KIT

Karlsruhe Institute of Technology

Analysis of Radon-Induced Background during First Measurements at the KATRIN Main Spectrometer

Analyse des Radon-induzierten Untergrunds während erster Messungen am KATRIN Hauptspektrometer

Masterarbeit
von

Jan Christian Johann Oertlin

Institut für Experimentelle Kernphysik
Karlsruher Institut für Technologie

Erstgutachter:	Prof. Dr. Guido Drexlin
Zweitgutachter:	Prof. Dr. Günter Quast
Betreuender Mitarbeiter:	Dr. Marco Kleesiek

22. September 2014

Zusammenfassung

Im Jahr 1930 schlug W. Pauli ein neues, massenloses Teilchen vor, um das kontinuierliche Energiespektrum von Elektronen zu erklären, die bei einem β-Zerfall emittiert werden. Zu dieser Zeit wurde angenommen, dass am β-Zerfall nur der Atomkern und das Elektron beteiligt sind, was eine bestimmte Elektronenenergie erwarten lässt. Dies würde durch die Beobachtung des Energiespektrums zu einer Verletzung des Energie- und Impulserhaltungssatzes führen. Das später in *Neutrino* umbenannte Teilchen löste dieses Problem.

1956 wurden die ersten Neutrinos von C. L. Cowan und F. Reines nachgewiesen. In den 1960er Jahren trat das *solare Neutrino Problem* auf: Es wurden weniger Elektron-Neutrinos von der Sonne gemessen als erwartet. Dies wurde schlussendlich 2001 vom SNO-Experiment durch Neutrino-Oszillation erklärt, was allerdings eine von Null verschiedene Neutrinomasse bedingt.

Das KATRIN-Experiment wird die Neutrinomasse mit einer Sensitivität von $m_{\overline{\nu}_e} = 200\,\text{meV}/c^2$ bei $90\,\%$ C.L. messen. Das ist eine Verbesserung von einer Größenordnung im Vergleich zu den Vorgänger-Experimenten in Mainz und Troizk. Bei dem am Campus Nord des Karlsruher Institutes für Technologie aufgebauten Experiment kommen MAC-E-Filter zum Einsatz. Diese filtern den immensen Strom an Elektronen, der von der Tritiumquelle erzeugt wird. Die Elektronen werden mithilfe eines magnetischen Feldes über verschiedene Komponenten durch das Spektrometer bis hin zum Detektor geleitet.

Um diese Sensitivität zu erreichen, müssen alle Komponenten bis an die technisch machbaren Grenzen hin optimiert werden. Das bedeutet u. a., dass der Untergrund auf $10\,\text{mHz}$ reduziert werden muss. Dabei stellte sich durch frühere Arbeiten heraus, dass die Radon-Isotope ^{219}Rn und ^{220}Rn eine Haupt-Untergrundquelle sind. Obwohl sie α-Strahler sind, wird der Zerfall durch die Freisetzung von Elektronen begleitet. Diese werden durch verschiedene Prozesse erzeugt, wodurch sie Energien von ca. $1\,\text{eV}$ bis hin zu mehreren $100\,\text{eV}$ erhalten können.

Die auf diese Weise erzeugten Elektronen können im Hauptspektrometer nach dem Prinzip der magnetischen Flasche gespeichert werden und durch das Ultrahochvakuum von $10^{-11}\,\text{mbar}$ können Speicherdauern von mehreren Stunden erreicht werden. Dabei beschreiben sie Zyklotronbewegungen um die Magnetfeldlinien und Magnetronbewegungen um die Symmetrieachse des Spektrometers. Sie bleiben so lange gespeichert, bis ihre Energie abgenommen hat und eine Schwelle unterschritten wird, bei der sie nicht weiterhin gespeichert sind. Dies geschieht durch Streuung mit den Restgasmolekülen; dabei können die gespeicherten Elektronen diese auch ionisieren, was zu weiteren Elektronen (Sekundärteilchen) führt. Diese wiederum können den Detektor erreichen und treten so als Untergrundkomponente auf. Auf diese Art können Elektronen, welche durch Radon erzeugt wur-

den, über mehrere Stunden mehrere tausend Sekundärelektronen erzeugen, was über diese Zeit zu einem erhöhten Untergrundniveau führt.

In früheren Arbeiten wurden bereits aktive und passive Methoden entwickelt, um diesen Untergrund weitestgehend zu unterdrücken: Dennoch ist es wichtig, den Untergrund noch besser zu verstehen, denn es ist weiterhin möglich, dass Radon-induzierter Untergrund auftritt bevor die Unterdrückungsmethoden greifen.

Im Rahmen dieser Arbeit wurden Messungen analysiert, die während der ersten Inbetriebnahme Phase (SDS-1) aufgenommen wurden. Dabei wurde das Spektrometer- und Detektorsystem ausführlich getestet. Bei diesen Messungen wurde u. a. auch der Druck von 10^{-11} mbar innerhalb des Spektrometers durch das Einführen von Argon auf 10^{-8} mbar erhöht. Dies hat den Vorteil, dass genau nur ein Elektron zur selben Zeit gespeichert wird, da die Speicherzeit direkt mit dem Druck zusammenhängt. Somit ist es möglich, einzelne Radon-Zerfälle zu untersuchen.

Dabei ist entscheidend, die zwei verbleibenden Untergrundkomponenten zu trennen: Radon induzierter Untergrund und Myon induzierter Untergrund. Der Unterschied zwischen beiden Komponenten besteht darin, dass die durch gespeicherte Elektronen erzeugten Ereignisse korreliert, die durch Myonen erzeugten dagegen Poisson verteilt sind. Die beiden Untergrundkomponenten können mit zwei Bedingungen unterschieden werden: Erstens, wenn die Zeiten zwischen zwei Ereignissen betrachtet werden. Dabei wird die Grenze bei $\Delta t = 0.2$ s gezogen: Alle Ereignisse mit $\Delta t < 0.2$ s werden gespeicherten Elektronen, die anderen Myonen zugeordnet. Zweitens wird weiterhin verlangt, dass ein gespeichertes Elektron (es wird angenommen, dass dies einem Radon-Zerfall entspricht) mindestens drei Sekundärelektronen (die *Multiplizität*) erzeugt hat.

Anhand dieser Separation wurden die Untergrundraten der unterschiedlichen Komponenten bestimmt. Dabei sind (569.8 ± 2.0) mcps Radon induziert und (232.0 ± 1.2) mcps durch Myonen verursacht. Die Gesamtrate wurde auf (857.7 ± 2.4) mcps bestimmt. Die radiale Verteilung der einzelnen Untergrundkomponenten entspricht den Erwartungen: Je kleiner der Radius, desto mehr gespeicherte Teilchen werden gefunden. Die Ursache liegt darin, dass der gültige Energiebereich desto kleiner, je weiter außen ein Elektron gespeichert ist. Für Myon-induzierten Untergrund ist dies gerade umgekehrt, da magnetische und elektrostatische Abschirmungsmechanismen die Elektronen (welche durch Myonen aus der Tankwand geschlagen werden) nicht tief ins Spektrometerinnere eindringen lassen.

Die Radon-Aktivität innerhalb des beobachtbaren Flussschlauchvolumens konnte bestimmt und auf das gesamte Hauptspektrometer extrapoliert werden. Die Aktivität beträgt damit (189.8 ± 12.8) mBq. Dabei ist zu beachten, dass dies nicht der wahren Aktivität entspricht: Durch die Untergrundseparationsmethode werden Radon-Zerfälle mit Multiplizitäten von zwei und eins nicht berücksichtigt. Dies wird korrigiert, indem die entsprechende Verteilung extrapoliert wird. Da die Extrapolation nicht eindeutig ist, wurde eine obere und eine untere Grenze bestimmt. Damit liegt die wahre Aktivität zwischen (286.6 ± 19.3) mBq und (541.3 ± 37.4) mBq. Weiterhin sind diejenigen Zerfälle nicht berücksichtigt, welche

kein Signal am Detektor erzeugen. Der entsprechende Korrekturfaktor wurde durch erste Simulationen auf ≈ 2 geschätzt.

Die mittlere Speicherzeit bei 10^{-8} mbar wurde auf (212.5 ± 3.5) ms bestimmt, der wahrscheinlichste Wert (MPV) auf (63.05 ± 1.40) ms. Die Untergrundrate und die Anzahl an gleichzeitig gespeicherten Elektronen bei einem Druck von 10^{-10} mbar bzw. 10^{-11} mbar konnten durch Strecken der Speicherzeit abgeschätzt werden. Dabei ergab sich eine Untergrundrate von (269.8 ± 0.9) mcps bzw. (267.1 ± 0.9) mcps. Die Anzahl der gleichzeitig gespeicherten Elektronen beträgt 9.0 ± 3.0 bei 10^{-10} mbar. Für einen Druck von 10^{-11} mbar wurde die Anzahl mittels zwei unterschiedlichen Methoden zu 39.0 ± 6.2 bzw. 89.6 ± 9.5 bestimmt.

Im Rahmen dieser Arbeit wurde außerdem ein empirisches Radon-Untergrundmodell entwickelt. Es basiert vollständig auf den oben erläuterten Analysen. Neben der Bestimmung der wahren Aktivität innerhalb des Spektrometers war es auch möglich, den Einfluss des Myon induzierten Untergrunds zu untersuchen. Es stellte sich heraus, dass die Anzahl an gefundenen Radon-Zerfällen um $2.3\,\%$ überschätzt wird. Die Geschwindigkeit der Simulation bei diesem Modell ist deutlich höher als das Simulieren auf Teilchenebene. Deshalb eignet sich dieses Modell dazu, den Radon-Untergrund für Sensitivitätsuntersuchungen zu generieren.

Introduction

Since the postulation of the neutrino by W. Pauli in 1930, it became one of the most mysterious particles. The neutrino was invented to explain the energy and momentum conservation in β-decay. At this time, the β-decay was considered to be a two body decay. However, this was in conflict with the continuous energy distribution of the released electron. By the first observation of a neutrino in 1956, the issue was resolved. With the rising of the *solar neutrino problem* in the 1960s, the idea of neutrino oscillations was pushed by experiments. Nevertheless, this implies a finite neutrino mass, which was former assumed to be zero.

KATRIN is a next-generation experiment, which will measure the neutrino mass with a sensitivity of $m_{\overline{\nu}_e} = 200\,\mathrm{meV/c^2}$ at $90\,\%$ C.L. This is an improvement of one order of magnitude, compared to previous experimets in Mainz and Troitsk. KATRIN is located at the Campus North at the Karlsruhe Institute of Technology (KIT). The electron-antineutrino mass will be measured model independent by utilizing the MAC-E-filter principle. For this purpose, major experimental challenges are the required ultra-high vacuum, an extraordinary stable high voltage system, a well-known magnetic field, a well-known high-intensity tritium β-decay source and a very low background level. The β-decay electrons will be guided by magnetic field lines from the source through the spectrometers to the detector.

The focus of this thesis lies on the background. The design background rate is $10\,\mathrm{mcps}$, which requires to optimize all background components. In previous theses $^{219}\mathrm{Rn}$ and $^{220}\mathrm{Rn}$ were discovered to be main background sources. Since radon is a uncharged, magnetic and electrostatic shielding do not have any effect. Also, electrons are released during decay, although radon is an α-emitter. These are produced by several processes, which result in electron energies from about $1\,\mathrm{eV}$ up to several $100\,\mathrm{keV}$. Such an electron can be stored inside the main spectrometer by the *magnetic mirror effect*. Since there is an ultra-high vacuum inside, the storage times can reach up to several hours. During this time, the electron is cooled down by scattering with residual gas molecules. This includes the ionization of these molecules. The electrons, released through ionization, are called secondaries and they are able to reach the detector and appear as background. If the electron energy reaches its storage condition threshold, it can escape the trap.

In previous theses, several active and passive methods were developed for suppressing radon-induced background. But it is still possible that radon induces background before the suppressing methods take effect. Therefore, it is of particular interest to know the activity of radon inside the main spectrometer. In the context of this work, this purpose was reached by analyzing data from the first commissioning phase (SDS-1). During this phase, also measurements of artificially elevated pressure are performed. That means, the pressure is elevated

from 10^{-11} mbar to 10^{-8} mbar. Thereby, the purpose is to significantly shorten the storage time of an electron. The shortened storage time is suitable for investigating single radon-decays, as for these conditions the mean storage time is much lower than the activity.

Chapter 1 gives a brief overview of the neutrino physics. This chapter is followed by an introduction of the KATRIN experiment (chapter 2), where the measurement principle as well as all major components are described. Also, different background sources are briefly discussed. A more detailed view on radon-induced background is given in chapter 3. A radon background model with several electron generating processes accompanying a radon-decay is introduced. Additionally, the impact of the pressure and the gas species to radon-induced background inside the main spectrometer are examined.

The main analysis of the measured data during SDS-1 is performed in chapter 4, presenting the separation of background components, the determination of the observable radon activity and its estimation of the actual activity and an extrapolation to a pressure of 10^{-10} mbar and 10^{-11} mbar.

Chapter 5 discusses an entirely empirical radon background model based on the analysis of chapter 4.

Contents

1. Neutrino Physics

The neutrino particle was postulated by W. Pauli in 1930. At this time, physicists were wondering about the continuous energy spectrum of the electrons, emitted by β-decay. This process was supposed to be a two-body reaction. That implies, that a discrete energy spectrum of the electron should be measured. Therefore, they concluded that the energy conservation might be broken. But in his letter *Dear radioactive ladies and gentlemen...* Pauli proposed a new particle named *neutron* to L. Meitner and his colleagues at a conference in Tübingen, to explain how the energy and momentum at the β-decay can be conserved. This electrically non-charged and spin-1/2 particle carries a part of the energy without be observed by any detector. This led to a three-body process

$$\mathrm{n} \rightarrow \mathrm{p}^+ + \mathrm{e}^- + \overline{\nu}_\mathrm{e}. \tag{1.1}$$

This new particle was renamed by E. Fermi to *neutrino*, as the neutral particle of the nucleus was named to *neutron*. Furthermore, Fermi developed the basic theoretical descriptions for the neutrino published in 1934 [Fer34].

It was 23 years later that this particle was observed for the first time. In 1956 C. L. Cowan and F. Reines gave the proof of the neutrino within the *poltergeist project*. This was done at a reactor, since a tiny cross section was expected and therefore a large number of neutrinos is required. For this experiment, electron-antineutrinos are used to induce a inverse β-decay

$$\overline{\nu}_\mathrm{e} + \mathrm{p}^+ \rightarrow \mathrm{n} + \mathrm{e}^+ \tag{1.2}$$

at a hydrogen nucleus of water. In this process, two well observable products are emitted, the positron (observed through annihilation with an electron) and the neutron. The latter is moderated by the water. Microseconds later, captured by cadmium-chloride (which was added to the water), it also induces a photon signal. By measuring the signal of the positron and the signal of the neutron within several microseconds, a neutrino was detected. They found a tiny cross-section for the process (1.2) of $(1.10 \pm 0.26) \times 10^{-43}\,\mathrm{cm}^2$ [RC59].

Several years later, 1962 J. Steinberger, M. Schwartz and L. M. Lederman found with the first neutrino-beam, produced with an accelerator, a second neutrino generation, the muon-neutrino. 38 years later in 2000, the last light neutrino generation was observed with the DONUT-experiment, namely the tau-neutrino. Neutrinos lighter than $45\,\mathrm{GeV}/c^2$ are excluded by studies of the Z^0-resonance at the LEP accelerator at CERN [EHO$^+$04].
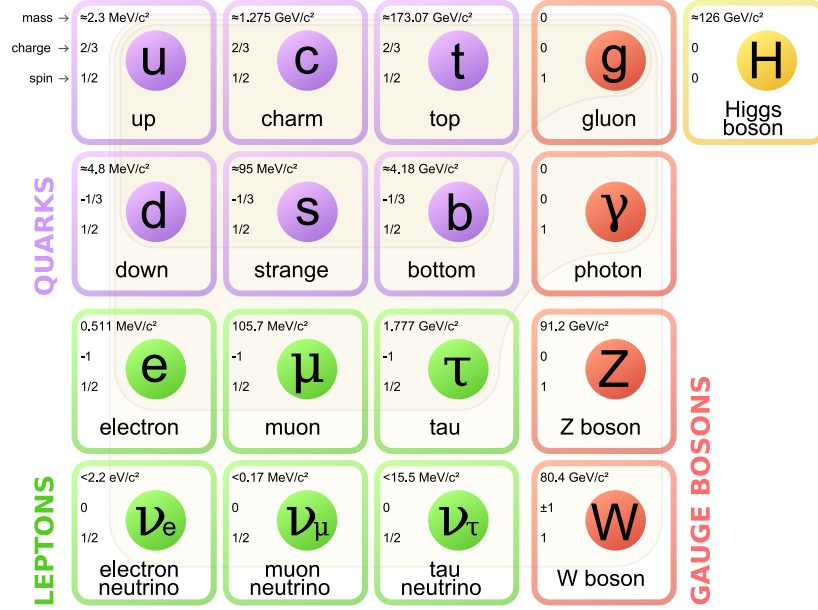
Figure 1.1.: Overview of all known particles of the Standard Model of particle physics. They are divided into fermions and gauge bosons. The fermions are also divided into three generations and containing the neutrinos, which only interacts through the weak interaction. The bosons contains all mediator particles and the Higgs-boson [Mis06].

In this chapter, a brief introduction to neutrino physics is given. In section 1.1, the neutrino is classified within the Standard Model of particles physics. The flavor-changing process of neutrino-oscillation is discussed in section 1.2 and sources of neutrinos in section 1.3. Several methods and experiments for determining the neutrino mass are discussed in section 1.4.

1.1. Neutrinos in the Standard Model

Neutrinos are part of the Standard Model of particle physics. This model describes all known particles and their interaction through the three basic forces, the strong and weak nucular and the electromagnetic. Also the mechanism of gaining mass with the Higgs-boson, discovered in 2012, is described by the Standard Model.

In this model the particles are classified in gauge bosons and fermions (see figure 1.1). Gauge bosons (mediators of the elementary forces) are the photon (γ), gluon (g) and $W^\pm/Z^0$-particles. Fermions are quarks and leptons. Each class is grouped in three generations, where the first generation contains the lightest particles (we are made of, as it is energetically most favorable) except for the neutrinos, as their exact mass is currently unknown. All fermions participate in the weak nuclear interaction. The mediators are the $W^\pm$ and Z^0 bosons. All charged particles

underlie the electromagnetic force, which is transferred by the photon.

The quarks are the only particles without n integer multiples of the elementary charge e. Up, charme and top quarks carry a charge of $2/3 \cdot e$, down, strange and bottom $-1/3 \cdot e$. In addition, they are the only particles that participate in the strong nuclear interaction, since these carry a so-called *color-charge*. The mediator particle is known as the gluon (g), which carries a color as well as an anti-color. Through the weak nuclear interaction[1], the quarks can change their type, the so-called *flavour*. So far, a single quark was not observed yet. This is described by the *confinement*, as the stored energy between two quarks increases with increasing distance until a new quark-antiquark pair of particles can be generated.

The leptons consist of the charged electron, muon and tau and the non-charged neutrinos ν_e, ν_μ and ν_τ. Within a generation, the particles are able to change their flavor by an interaction with a charged mediator particle of the weak interaction: $W^\pm$. The uncharged particle is named Z^0 boson. The type of leptons is also called flavor.

The recent discovered Higgs-particle is a consequence of the Higgs-mechanism. The mechanism gives all the particles their masses and originates from the electroweak symmetry breaking.

In the Standard Model, the neutrinos have no mass. In 1958, M. Goldhaber published results of an experiment for measuring the helicity[2] of neutrinos [GGS58]. It revealed that all neutrinos have a negative helicity. This implies that neutrinos travel with a velocity close to the speed of light. If they have a mass, their velocity is lower than c. Consequently a system should be able to find in which the helicity is positive. This opens also the possibility that neutrinos are their own antiparticle, thus Majorana-particles. In the case of neutrinos are Majorana-particles, neutrinos have always a negative helicity and antineutrinos positive helicity. This leads to a violation of the conservation of the leptonic number. If neutrinos are Majorana-particles, this is investigatable with neutrinoless double beta decay experiments.

1.2. Neutrino Oscillation

Neutrinos are able to change their flavor. If a neutrino was produced with a specified flavor, the same neutrino can appear with an other flavor at the next interaction. This idea was first proposed by B. Pontecorvo in 1957. For neutrino oscillations, the mass-eigenstates $|\nu_i\rangle$, where $i = 1, 2, 3$, of neutrinos have to be different to the flavor-eigenstates $|\nu_\alpha\rangle$, where $\alpha = e, \mu, \tau$, and consequently the neutrinos have to have a mass. The flavors are a composition of the mass-eigenstates, as obtained in the following equation:

$$|\nu_\alpha\rangle = \sum_i U_{\alpha i}|\nu_i\rangle, \tag{1.3}$$

---

[1]Mention the CKM-matrix.
[2]The orientation of spin in dependence to the momentum.

1. Neutrino Physics

$U_{\alpha i}$ is the mixing matrix, called PMNS[3], similar to the CKM-matrix for a mixing. This matrix describes how the mass-eigenstates interfere and how the composition changes with traveled distance of the neutrino. The probability of a flavor change from α to β can be derived concerning a traveled distance L and energy E dependence and is given by

$$P_{\alpha\to\beta}(L,E) = \sum_{i,j} U^{\star}_{\alpha i} U_{\beta i} U_{\alpha j} U^{\star}_{\beta j} \cdot \mathrm{e}^{-i\frac{\Delta m^2_{ij}L}{2E}} \tag{1.4}$$

with the mass difference between two mass eigenstates $\Delta m_{ij} = m_i - m_j$. To make the periodic change more obvious, the next equation is derived for the case of a two-flavor oscillation:

$$P_{\alpha\to\beta}(L,E) = \sin^2 2\theta_{ij} \cdot \sin^2 \frac{\Delta m^2_{ij}L}{4E}, \tag{1.5}$$

where θ_{ij} is the mixing angle. From that, the oscillation length L_{osc} can be extracted:

$$L_{\mathrm{osc}} = \frac{4\pi E}{\Delta m^2_{ij}}. \tag{1.6}$$

It is reasonable that for $L \ll L_{\mathrm{osc}}$ probably no oscillation is observable (that is used in some experiments to measure the initial neutrino flux). For $L \gg L_{\mathrm{osc}}$, the oscillation is very fast and therefore only the average transition probability can be measured.

The given equations are only valid for vacuum propagation. The propagation within matter is different as the neutrinos are able to interact with the medium. This leads e.g. for the neutrinos coming out of the sun to the so-called MSW-effect[4] [MS86, Wol78]. This effect appears in matter, to be more precisely at the presence of electrons. The electron-neutrinos underlie coherent forward scattering by interacting weak through charged currents. This leads to a different effective electron-neutrino mass and induces a resonant transformation of the neutrino flavor.

In the 1960s, the so-called *solar neutrino problem* occurred since R. Davis Jr. started to measure the solar electron-neutrino flux at the Homestake-experiment. This Tetrachloroethylene-based experiment observed a neutrino deficit. One possible explanation was that the actually well known Standard Solar Model (SSM) is not a good description. It provides the initial neutrino flux by basic nuclear processes. The other explanation was that the deficit of electron-neutrinos is caused by neutrino-oscillation. So, the electron-neutrinos change their flavor during the travel from the sun to the earth and cannot be detected at this experiment. The results of the Homestake-experiment was confirmed by other experiments like GALLEX, GNO, SAGE, Kamiokande and SNO, where the first three experiments are gallium-based and the last two are water-based.

---

[3]Named after B. Pontecorvo, Z. Maki, M. Nakagawa and S. Sakata.
[4]Named after S. Michejew, Alexei J. Smirnow and L. Wolfenstein.

In 2001 the solar neutrino problem was finally solved by the SNO-experiment[5] [AAA$^+$01]. This experiment was able to measure all three neutrino flavors. The total number of detected neutrinos for all flavors agree with the calculations of the SSM and gives as possible explanation neutrino oscillations.

1.3. Neutrino Sources

In nature a lot of neutrino-sources are existing. Also man-made source are existing. The most important neutrinos sources are briefly introduced in the following.

1.3.1. Natural Sources

Natural sources are important for the understanding of neutrinos and, for instance, the Sun. They are investigated for several years and still of interest to catch the nature of neutrinos.

Relic Neutrinos

One neutrino source is the Big Bang itself. Since the decoupling of the weak interaction took place about 0.1 s after the Big Bang, the neutrinos produced before can stream free through the universe. A scan of the entire sky for such neutrinos would result in a CMBR-like[6] map. But in contrast, this picture would show the universe at an earlier time, $t \approx 0.1$ s.

The neutrinos have a strong impact to the evolving of the universe. They affect for example the forming of galaxies. During the free-streaming of the neutrinos, they carry energy respectively mass away and hence they smear out small structures up to 1 Gpc. Consequently, neutrinos are important to understand the structure and the evolution of the universe. The number of relic neutrinos per volume and flavor is given with

$$n_\nu = 113 \,/\mathrm{cm}^3/\mathrm{flavour}. \tag{1.7}$$

This is a deviation from the CMBR by using Fermi- and Bose-statistics. Also, in total the density is $339 \,/\mathrm{cm}^3$ neutrinos of all three light flavors, as at $t < 0.1$ s all flavors produced in equal shares.

Supernova Neutrinos

Another cosmic source is a supernova explosion of type II. This happens when a lot of heavy elements are accumulating at the core of the star. These elements are (for example) $^{56}\mathrm{Ni}$, $^{54}\mathrm{Fe}$ and $^{52}\mathrm{Cr}$. Their energy budget at fusion are negative,

---

[5]**S**udbury **N**eutrino **O**bservatory

[6]The sky was scanned by many experiments for the cosmic microwave background radiation (CMBR). As example should be mentioned the COBE-satellite and the orbiter WMAP and PLANCK. This background radiation is due to the electromagnetic decoupling about 380 000 years after the Big Bang. It gives a picture of the universe at exactly the time of decoupling and helps to understand the development and the properties of the universe.

that means energy is required. Hence, the fusion stops inside the core and the pressure due to radiation is lost. If the core reaches the mass threshold of the Chandrasekhar-mass of $1.44M_{\odot}$, the pressure due to gravitation is large enough, so that the core begins to collapse. That means that the electromagnetic force is not strong enough anymore to keep the atomic orbitals. The electrons interact with the protons and neutrons and neutrinos are generated through

$$e^- + p^+ \rightarrow n + \nu_e. \tag{1.8}$$

The core collapse happens within less than one second and leads to a core only made-up of neutrons. This very huge nucleus is incompressible. Consequently, the collapse stops and the following inbound shock waves are reflected. This finally ends after about two hours in the final supernova type II. The produced neutrinos carry about $99\,\%$ of the released binding energy away.

As the supernova is visible until the shock wave reaches the surface of the star, it takes hours from the beginning of the core collapse (and consequently the generating of the neutrinos) and the possibility of a visual detection. But as the neutrinos escape the core, a supernova early warning system (SNEWS) can be started. It is based on measuring the first neutrino burst of supernovas with neutrino telescopes. In 2014, five neutrino observatories are member of SNEWS [SNE14]: Borexino, Super-Kamiokande, LVD, KamLAND and IceCube. If SNEWS detects a neutrino burst and can reconstruct the direction, other (visual) groups are informed. They have enough time to steer their instruments to the corresponding part of the sky.

Solar Neutrinos

The strongest neutrino source for the earth is the sun. In several nuclear fusion processes the neutrinos are emitted. The neutrinos travel through the different layers of the sun by being affected by the MSW-effect and moved to the earth. They may change their flavor[7]. Most of the neutrinos, namely $86\,\%$, are created by the slow

$$p + p \rightarrow d + e^+ + \nu_e \tag{1.9}$$

process. But there are also other processes, as shown in figure 1.2. The neutrino flux is calculated by the Standard Solar Model, including all these processes.

Atmospheric Neutrinos

Another natural neutrino source is the atmosphere of the earth. The atmosphere is permanently hit by cosmic rays such as photons, electrons, protons and other particles. By interacting with the molecules, (extensive) air showers of particles occur. Inside these showers, a lot of particles are produced. For example, Kaons emitting during their decay chain ν_e and ν_μ with an ratio of $2 : 1$ (compare equations (1.10) to (1.12)).

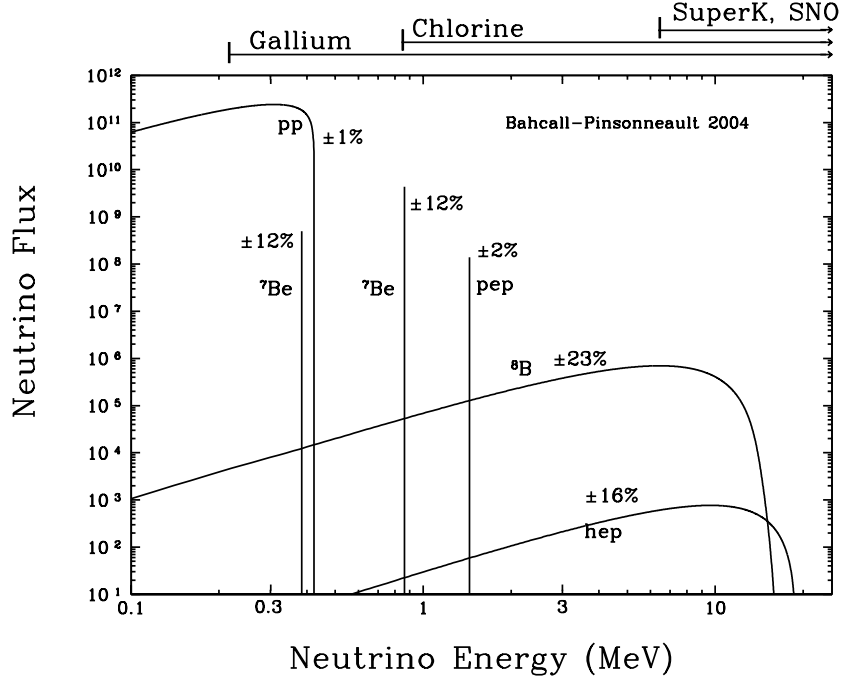[7]For MSW-effect and neutrino-oscillation see section 1.2.

Figure 1.2.: The solar neutrino spectrum. The most important process is the pp-cycle, in which especially low energy neutrinos are produced. Other processes are rare, but the are able to generate neutrinos with higher energy. Some experiments, which can measure neutrinos in the specific energy ranges are included [BP04].

1.3.2. Man-Made Sources

Man-made sources are essential for investigating neutrinos. For example, the first observation of neutrinos was performed at a nuclear reactor. Also, neutrino beams generated by accelerators are indispensable for neutrino studies.

Reactor Neutrinos

Neutrinos, produced in nuclear power plants, are often used to investigate the neutrino oscillation (see section 1.2). Nuclear reactors are the strongest terrestrial neutrino sources. At each fission, in average six neutrinos are generated. The neutrinos have an energy up to 10 MeV.

Among science, the neutrinos can be also used for surveillance of nuclear weapon stocks and compliance of contracts.

Accelerator Neutrinos

Moreover, accelerators can be used to generate neutrinos. In particular, well focused neutrino beams are possible. For this, the accelerated particles are directed to a fixed target. By nuclear reactions, among other particles charged Kaons and

Pions are produced, which can be focused and deflected by magnets. These particles decay after a short time and produce neutrinos:

$$K^+ \rightarrow \mu^+ + \nu_\mu \tag{1.10}$$

$$\pi^+ \rightarrow \mu^+ + \nu_\mu \tag{1.11}$$

$$\mu^+ \rightarrow e^+ + \nu_e + \overline{\nu}_\mu \qquad \text{(The antiparticles analog.)} \tag{1.12}$$

The neutrino beam (GeV range) can be send through earth reaching a distance up to several hundred kilometers to investigate, for example, neutrino oscillations.

1.4. Determination of the Neutrino Mass

The neutrino mass is still not known until now. From the observation of the neutrino oscillation (see section 1.2), neutrinos should have a mass $m_\nu > 0$. Several experiments revealed, that the mass is very small. The current upper limit for the electron-antineutrino is about $2\,\text{eV/c}^2$ [YAA$^+$06].

From several neutrino oscillation experiments, the mass-differences Δm_{ij}^2 between two mass-eigenstates i and j are known. But the order and the absolute scale is still unknown and currently under investigation. Often three scenarios are mentioned, the normal hierarchical, the inverted hierarchical and the quasi-degenerated. The first case postulates $m_1 \ll m_2 < m_3$, the second $m_3 \ll m_1 < m_2$ and the third $m_1 \cong m_2 \cong m_3$, where are the mass eigenstates differences much smaller than the absolute masses.

In the following, several methods and experiments to measure the neutrino-mass are briefly introduced. In section 1.4.1, the neutrino-mass derived from cosmological observations is discussed. In the next sections, methods for determining the mass with double beta decay experiments (section 1.4.2) and single beta decay experiments (section 1.4.3) are introduced.

1.4.1. Cosmological

Neutrinos are an important part of the evolution of the universe. So they contribute to the total energy density of the universe as well as they are involved into the formation of structures. With this, neutrino-mass estimations can be obtained, which are discussed in the following.

The first Friedmann equation [Fri22] describes the expansion of the universe in dependency of the Hubble parameter $H(t)$ respectively the scale factor $a(t)$ and the total energy density ρ:

$$\left(\frac{\dot{a}}{a}\right)^2 = H^2 = \frac{8\pi G}{3}\rho = H_0^2 \frac{\rho}{\rho_c^0}. \tag{1.13}$$

H_0 is the current value of the Hubble parameter, $H_0 = (67.3 \pm 1.2)\,\text{kms}^{-1}\,\text{Mpc}^{-1}$, and ρ_c^0 is the critical density today with a value of $\rho_c^0 = 1.88 \times 10^{-29} h^2 \text{gcm}^{-3}$ with $h = H_0/(100\,\text{kms}^{-1}\text{Mpc}^{-1})$ [AE14]. By assuming a flat universe, the total energy

density is given. The upper limit for the sum of all neutrino mass-eigenstates [LP12] is estimated to

$$\sum_i m_i \leq 15 \, \text{eV/c}^2. \tag{1.14}$$

Better estimations are obtained by considering scale formations. Neutrinos carried a lot of energy away from mass over-density regions. This lead to a smear out of structures. As this effect is neutrino mass dependent, an estimation of the neutrino mass can be given by using observations of mass density. The density fluctuation was for example investigated by the Sloan Digital Sky Survey [AAPA+11]. Combining this and data of CMBR, supernova and baryonic acoustic oscillation [AF11], the upper limit is determined to

$$\sum_i m_i \leq 0.51 \, \text{eV/c}^2 \qquad (95 \, \% \, \text{C.L.}). \tag{1.15}$$

But strikingly variations of the neutrino mass occur by using different data samples. This shows the strong model-dependency of such approaches to determine the neutrino mass [Han10].

1.4.2. Neutrinoless Double Beta Decay

The mass of neutrinos can also be estimated by the Majorana-mass $m_{\beta\beta}$. But this implies, that neutrinos are Majorana-like. The double β-decay with two emitting neutrinos ($2\nu\beta\beta$-decay) is very rare (half-life in the region of 10^{19} to 10^{21} years) and was first proposed in 1935 by M. Goeppert-Mayer [Goe35]. The first observation was succeeded in 1987 for ^{82}Se [EHM87]. The double β-decay happens, if the single β-decay is energetically forbidden.

Another process for double beta decay is the in 1937 from G. Racah [Rac37] and in 1939 from W. Furry [Fur39] proposed neutrinoless double beta decay ($0\nu\beta\beta$-decay), which is still not observed yet. But this requires that the neutrino is its own antiparticle, hence a Majorana particle. The only different between neutrino and antineutrino is the helicity. Consequently, the neutrino have to carry a mass, that the helicity can change.

The $0\nu\beta\beta$-decay is a good possibility to investigate the nature of neutrinos. At this process, one neutron decays by emitting an antineutrino. This antineutrino induces a second neutron decay:

$$\text{n} \quad \rightarrow \quad \text{p}^+ + \text{e}^- + \overline{\nu}_\text{e} \tag{1.16}$$
$$\nu_\text{e} + \text{n} \quad \rightarrow \quad \text{p}^+ + \text{e}^- \tag{1.17}$$

However, for that the antineutrino has to change into a neutrino. This can only happen, if the neutrino is a Majorana particle. This process should be observable as a peak at the end of the electron spectrum, as no energy is carried away by neutrinos. The measured parameter of such experiments is the half-life $T_{1/2}^{0\nu\beta\beta}$.
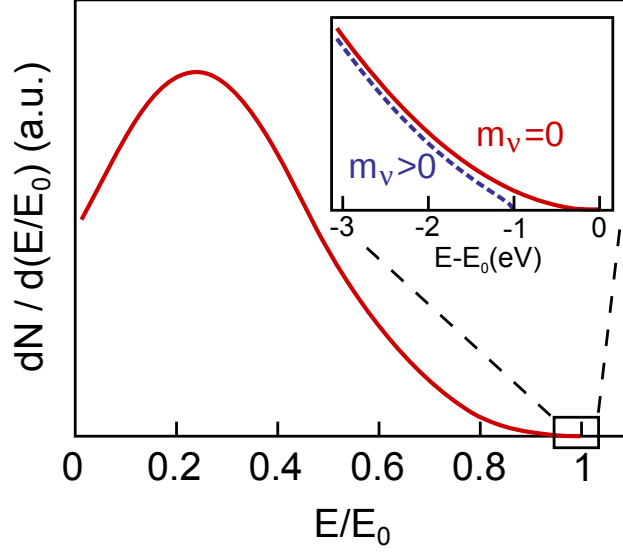
Figure 1.3.: Illustration of an electron spectrum due to tritium decay. If the mass of the neutrino is not equal to zero the spectrum will end at lower energies [Wan13].

The half-life is related to $m_{\beta\beta}$ [DTN$^+$81]:

$$\left(T_{1/2}^{0\nu\beta\beta}\right)^{-1} = G^{0\nu\beta\beta}(Q_{\beta\beta}, Z) \cdot \left| M_{\mathrm{GT}}^{0\nu\beta\beta} - \left(\frac{g_{\mathrm{V}}}{g_{\mathrm{A}}}\right)^2 \cdot M_{\mathrm{F}}^{0\nu\beta\beta} \right|^2 \cdot \frac{\langle m_{\beta\beta}\rangle^2}{m_{\mathrm{e}}^2}, \qquad (1.18)$$

where $G^{0\nu\beta\beta}$ is the phase space factor in dependence of the endpoint of the spectrum $Q_{\beta\beta}$ and the atomic umber Z. $M_{\mathrm{GT}}^{0\nu\beta\beta}$ respectively $M_{\mathrm{F}}^{0\nu\beta\beta}$ denotes the nuclear matrix elements of Gamov-Teller respectively Fermi transitions.

There are several experiments investigating the $0\nu\beta\beta$-decay, such as GERDA, CUORE and EXO. GERDA, for instance, completed recently the first measurement phase from 2011 to 2013. No evidence for the $0\nu\beta\beta$-decay was found [Mac14]. The lower limit for the half-life is determined to 2.1×10^{25} yr at $90\,\%$ C.L.

1.4.3. Single Beta Decay

A model independent effective neutrino mass determination can be performed by using the single β-decay. At this decay

$$\mathrm{n} \rightarrow \mathrm{p}^+ + \mathrm{e}^- + \overline{\nu}_{\mathrm{e}} \qquad (1.19)$$

three particles remain. As the nucleus mass is much heavier than the mass of the electron and the neutrino, the released energy is distributed to first order approximation between the electron and the neutrino. Consequently, the neutrino carries energy $\left(E_\nu = \sqrt{m_\nu^2 c^4 + p_\nu^2 c^2}\right)$ away and the measurable electron energy spectrum is continuous. If the neutrino mass is $m_{\overline{\nu}_{\mathrm{e}}} > 0$, the endpoint of the

electron spectrum is different as well as the shape [WA03] (also illustrated in figure 1.3):

$$\frac{\mathrm{d}N}{\mathrm{d}E} \propto (E_0 - E) \sqrt{(E_0 - E)^2 - m_{\nu_\mathrm{e}}^2 c^4}, \tag{1.20}$$

where E_0 is the endpoint energy. As only the electron's energy is measured, the effective mass of the electron antineutrino is model independent. Only energy and momentum conservation are considered. Theoretically the neutrino mass could be determined by measuring the endpoints, but in reality, these cannot be measured with sufficient precision. Thus, the shape of the spectrum close to the endpoint is measured and compared to the shape of the spectrum with no neutrino mass.

For measuring the electron spectrum, there are two possibilities in principle: Using cryogenic calorimeters or tritium decays. The first method is used in experiments as MARE, MANU and MIBETA. They are using ^{187}Re. The second method was used at experiments in Mainz and in Troitsk and is also used at KATRIN. In the next chapter, the Karlsruhe Tritium Neutrino Experiment KATRIN will be introduced.

1. Neutrino Physics

2. The KATRIN Experiment

The **Ka**rlsruhe **Tri**tium **N**eutrino experiment KATRIN is a next-generation tritium β-decay experiment to determine the effective mass of the electron-antineutrino. It is an international experiment which is located at the Campus North at the Karlsruhe Institute of Technology (KIT). KATRIN will have a sensitivity of $m_{\overline{\nu}_e} = 200 \, \mathrm{meV/c^2}$ at $90\,\%$ C.L. [KAT04], which is an improvement by one order of magnitude compared to previous experiments in Mainz and Troitsk. Because the measured observable is $m_{\overline{\nu}}^2$, many experimental parameters have to be improved by two orders of magnitude.

Major experimental challenges are the required ultra-high vacuum, an extraordinary stable high voltage system, a well-known magnetic field, a well-known high-intensity tritium β-decay source and a very low background level.

This chapter introduces the KATRIN experiment, explaining the measurement principle, which is based on the MAC-E filter (section 2.1), followed by an overview of the experimental setup (section 2.2). Of particular importance for this thesis are the different background sources affecting the experiment, which will be discussed in section 2.3. Finally, an overview of the recent measurements with the KATRIN spectrometer and detector system will be given in section 2.4. The analysis and interpretation of background data taken during that measurement phase is a major part of this thesis.

2.1. Measurement Principle

The KATRIN tritium source produces a high-intensity electron beam with a continuous energy spectrum. By measuring precisely the spectral shape close to the endpoint of $18.6\,\mathrm{keV}$, the effective mass of the electron-antineutrino is determined. The electrons are filtered according to their kinetic energy by a spectrometer using the MAC-E filter principle. To obtain the neutrino mass, a fit of a theoretical spectrum to the measured spectrum is applied, where the former is calculated from Fermi's theory of β-decay leaving the neutrino mass as a free parameter.

The scanning of the β-spectrum of tritium at KATRIN will be carried out using so-called MAC-E filters, which will be detailed in the following. A MAC-E filter is essentially a high-pass filter, where an electrostatic retarding potential, applied to the spectrometer vessel, is utilized to filter the β-decay electrons. While the source and detector are kept at ground potential, the maximum potential U_0 is reached at the central plane of the spectrometer, the so-called analyzing plane. Only if an electron from the source has enough kinetic energy, it can eventually
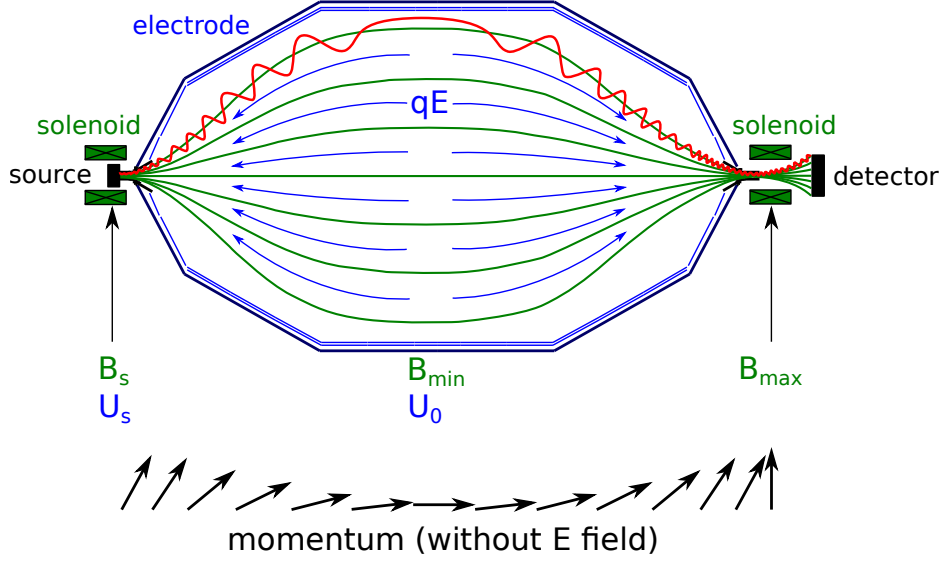
Figure 2.1.: Principle of the MAC-E filter. Electrons perform cyclotron motions around and along the magnetic field lines (green). The electrostatic retarding potential (blue) acts as a high-pass filter, selecting only the high-energy electrons to be counted by the detector. The lower part of the figure illustrates the transformation of the momentum vector due to the magnetic field gradient [Wan13].

pass the analyzing plane. Due to the vectorial character of the electric field, only the longitudinal component of the energy $E_\parallel$ contributes to passing the filter. As also energy is stored in the transversal component $E_\perp$, a mechanism is required to convert $E_\perp$ into $E_\parallel$, which is precisely what a MAC-E filter does, as illustrated in figure 2.1.

A magnetic field is required to fulfill this task. It has two major purposes: The Lorentz force keeps the β-electrons on a stable cyclotron motion around the magnetic field lines, while a slowly decreasing magnetic field results in an adiabatic transformation $E_\perp \to E_\parallel$. At the analyzing plane, ideally, the entire transversal energy is converted to longitudinal energy via the magnetic gradient force

$$\vec{F} = \vec{\nabla}(\vec{\mu} \cdot \vec{B}). \tag{2.1}$$

The energy conversion is a result of the conservation of the orbital magnetic moment

$$\mu = \frac{e^2}{2m_\mathrm{e}} \cdot \phi = \frac{E_\perp}{B}, \tag{2.2}$$

where ϕ is the magnetic flux. From equation (2.2) follows immediately, that a decrease (increase) of the magnetic field B results in a decrease (increase) in transversal energy. Energy conservation further necessitates a corresponding increase of the longitudinal energy component $E_\parallel$. Since the magnetic field cannot vanish at the analyzing plane, the electrons retain a small fraction of their initial

transversal kinetic energy.

An electron entering the spectrometer passes the region of maximal magnetic field strength, where at the same time the electrostatic potential is at its minimum. Successively the transversal energy is converted into longitudinal energy and the longitudinal energy into potential energy on its way to the analyzing plane. At the analyzing plane, the magnetic field strength is at its minimum; the electrostatic potential at its maximum. If now the electron possesses enough longitudinal energy, namely $E_\parallel \geq eU_0$, it will pass the analyzing plane towards the detector side. Now the electrostatic potential will decrease, so the electrons are re-accelerated to their originally kinetic energy. At the same time, the magnetic field increases and thus the longitudinal energy is converted back into transversal energy. Electrons with insufficient kinetic energies cannot overcome the retarding potential and will be reflected back to the source.

The energy resolution ΔE of a MAC-E filter is defined by the maximal and minimal magnetic field strength. Hence, ΔE determines the remaining transversal energy $E_\perp^{\mathrm{min}}$ at the analyzing plane (where $B = B_\mathrm{A}$) as a function of the initial transversal energy $E_\perp^{\mathrm{max}}$ (where $B = B_\mathrm{max}$). The energy resolution follows from equation (2.2):

$$\Delta E = E_\perp^{\mathrm{min}} = \frac{B_\mathrm{A}}{B_\mathrm{max}} \cdot E_\perp^{\mathrm{max}}. \tag{2.3}$$

Using the design values [KAT04] $B_\mathrm{A} = 3 \times 10^{-4}\,\mathrm{T}$, $B_\mathrm{max} = 6\,\mathrm{T}$ and $E_\perp^{\mathrm{max}} = 18.8\,\mathrm{keV}$, an energy resolution of $\Delta E = 0.93\,\mathrm{eV}$ is achieved.

Due to the small number of decays in the interesting energy region close to the endpoint ($2 \times 10^{-13}\,\mathrm{s}^{-1}$ at the last eV), the count rate and hence the accepted solid angle of electrons from the source have to be maximized. If the polar angle θ is large, the electrons travel a long distance through the source. Correspondingly, the probability for scattering off tritium molecules is large, resulting in a distortion of the spectral shape. As a counter measurement, a magnetic field strength of up to $B_\mathrm{S} = 3.6\,\mathrm{T}$ is used at the source, while the maximum magnetic field strength of $B_\mathrm{max} = 6\,\mathrm{T}$ is reached at the so-called pinch magnet, located between the spectrometer and the detector. This field ratio ensures, that electrons, which are emitted with a high polar angle, do not reach the spectrometer, but are magnetically reflected back to the source. The maximum polar angle θ_max is denoted by

$$\sin \theta_\mathrm{max} = \sqrt{\frac{B_\mathrm{S}}{B_\mathrm{max}}}. \tag{2.4}$$

If the values of B_S and B_max are inserted into equation (2.4), θ_max becomes $\theta_\mathrm{max} = 50.77°$. This value is high enough to gain a high count rate and small enough to ensure, that the probability for scattering is low.
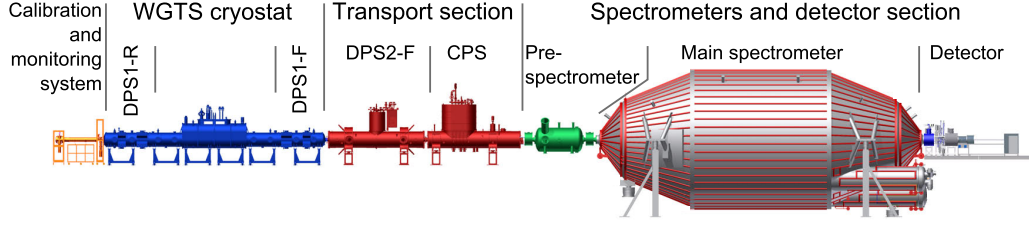
Figure 2.2.: Setup of the KATRIN experiment. Inside the WGTS the β-electrons are emitted by Tritium decays and guided adiabatically magnetic through the transport section and the pre-spectrometer. At the main spectrometer they are analyzed via the MAC-E filter principle and finally counted at the detector [BBB$^+$12].

2.2. Experimental Setup

The entire KATRIN setup has a total length of 70 m, with a maximal diameter of 10 m at the analyzing plane of the main spectrometer. The β-electrons are adiabatically guided by magnetic fields from the **w**indowless **g**aseous **T**ritium **s**ource (WGTS, see section 2.2.1) through the transport section, the pre-spectrometer and the main spectrometer to reach the detector system (see figure 2.2). The transport section consists of an active differential pumping system (DPS) and a passive cryogenic pumping system (CPS, section 2.2.2). The pre- and main spectrometer (section 2.2.3) act as MAC-E filters as described in section 2.1. The detector consists of 148 pixel Si-PIN diode, which will count the electrons, that passed the retarding potential of the main spectrometer (section 2.2.4).

2.2.1. Source

The low count rate in the interesting energy region around the tritium endpoint necessitates a very strong source. Therefore, this experiment is located at KIT Campus North as there already exists the needed infrastructure to handle the required amounts of tritium at the TLK[1]. The source, called WGTS[2], consists of a source tube with length of 10 m and diameter of 90 mm, housed within a cryostat. The advantage of a windowless gaseous source compared to a solid source are the reduced systematic uncertainties, as solid state and surface effects are circumvented. The gaseous molecular tritium with an isotopic purity of $\epsilon_{\mathrm{T}} \geq 95\,\%$ is injected at low pressure through more than 250 holes to keep the turbulences of the gas small. The flow rate comes to $1.853\,\mathrm{mbar}\,\ell\,\mathrm{s}^{-1}$. At both ends of the WGTS, differential pumping sections (DPS1-F and DPS1-R[3]) reduce the gas flow by two orders of magnitude. Hence, the tritium is pumped out with eight turbo molecular pumps. Pumped gas is cycled through the so-called *outer loop*, where it is purified and then reinjected into the WGTS through the *inner loop*. In this

---

[1]**T**ritium **L**aboratory **K**arlsruhe
[2]**W**indowless **G**aseous **T**ritium **S**ource
[3]**D**ifferential **P**umping **S**ection 1 - **F**ront respectively **R**ear

way about $40\,\mathrm{g}$ of tritium is lead through the WGTS every day.

To minimize the Doppler-broadening of the β-electrons, the WGTS is cooled down to $T = 27\,\mathrm{K}$ with a stability of $\pm 30\,\mathrm{mK}$. Two cooling tubes are assembled on the outside of the beam line, containing two-phase neon as cooling fluid. As the isotopic purity has to be known to an accuracy of $0.1\,\%$, the composition of the gas (H_2, HD, D_2, HT, DT, T_2) has to be monitored all the time. This is happening in the *inner loop* by use of Laser Raman-spectrosopy [FSS$^+$11] before the gas is reinjected. The source activity is measured by the monitor-detector in the Rear Section, which is mounted at the rear end of the WGTS. As this parameter cannot be measured with the main detector (section 2.2.4), this additional device is required in order to minimize systematic uncertainties.

The strength of the source is defined by the column density

$$\rho d = \frac{N}{A_\mathrm{S}}, \tag{2.5}$$

where A_S is the cross sectional area of the source and N the number of Tritium molecules. Considering also the isotopic purity ϵ_T, equation (2.5) becomes:

$$N = \rho d \cdot A_\mathrm{S} \cdot \epsilon_\mathrm{T}. \tag{2.6}$$

In standard operation mode, a column density $\rho d = 5 \times 10^{17}\,\mathrm{cm}^{-2}$ with a stability of $0.1\,\%$ is used.

A total of 7 superconducting magnets is utilized to adiabatically guide the electrons on cyclotron paths to the spectrometer or the Rear-Section. They produce a magnetic field of $T_\mathrm{S} = 3.6\,\mathrm{T}$ inside the source. The maximum of the magnetic flux ϕ_max is determined by

$$\phi = \int_\mathrm{A} \vec{B}\mathrm{d}\vec{A} \tag{2.7}$$

to $\phi_\mathrm{max} = 229\,\mathrm{Tcm}^2$. To minimize systematic uncertainties due to surface effects inside the source tube, only the inner $\phi = 191\,\mathrm{T\,cm}$ are analyzed. This leads to a effective activity of the source of $10^{10}\,\mathrm{Bq}$ [KAT04, BBB$^+$12].

2.2.2. Transport Section

The transport section contains two pumping systems. First, the active differential pumping section DPS2-F, and second, the passive cryogenic pumping section CPS. They connect the DPS1-F with the pre-spectrometer and guide the β-electrons adiabatically from the WGTS to the spectrometers. At the same time, it reduces the tritium flux from the source by twelve orders of magnitude down to a partial pressure of $10^{-19}\,\mathrm{mbar}$ inside the spectrometer, which is required to achieve an ultra-low background rate of $< 10^{-2}$ counts per second (see section 2.3.3).

DPS2-F

The DPS2-F has a length of $7.2\,\mathrm{m}$ and contains a beam tube with a diameter of $86\,\mathrm{mm}$. It is cooled down to $T = 77\,\mathrm{K}$ by liquid nitrogen and consists of five beam

line components as illustrated in figure 2.3. The second and the fourth component are tilted by 20° to improve the pumping efficiency and to prevent the molecular beaming effect. Turbo molecular pumps (TMP) are located between the individual beam line components. With a pumping rate of $2000\,\ell\,s^{-1}$, a tritium flux reduction by a factor of 10^5 is achieved. The gas is pumped into the *outer loop* and led back to the TLK to be reinjected into the WGTS.

To guide the electrons to the spectrometers, a total of 15 superconducting solenoids is installed to generate a magnetic flux density of $B = 5.6\,T$. In addition to the main solenoids, correction coils are installed at each bend to confine the transported flux inside the beam tube. The beam line and solenoids are surrounded by a helium cryostat.

Tritium and daughter ions are also guided by the magnetic field and hence are not affected by the TMPs. As they are mostly positively charged, they can, however, be blocked by a small potential of $+100\,V$, applied at the end of the DPS2-F beam tube. Therefore the ions turn back in the direction of the WGTS. Because of the gas flux from the WGTS, the ions cannot return into the source due to scattering with the gas atoms and molecules. So, they are trapped. That leads to a positive stored charge inside the DPS2-F, which causes a change of the energy of the β-electrons. To get rid of it, electrodes are installed to deflect the ions. After several passes, the deflection is large enough so, that the ions will be neutralized by hitting the surface of the tube. Now, they can be pumped out by the TMPs. The electrodes do not have an influence on the electron trajectories, because of the very short dwell time of the electrons in the electrostatic potential. Ions with a negative charge are rare and they recombine very fast with ions with a positive charge.

Inside the DPS2-F, an FT-ICR[4] trap is installed to monitor the ions and their deflection by the electrodes during measurement breaks [KAT04, LBB+12, Sch10].

CPS

The CPS reduces the gas flux by a factor of 10^7 by adsorbing the atoms and molecules on its inner surface. While the setup is very similar to that of the DPS2-F (see figure 2.4), the beam tube is cooled to $T = 4.5\,K$ by helium. A thin layer of argon frost covers the inner surface of the stainless steel tube which consequently acts as a cryo-adsorber. The tilted beam line increases the pumping efficiency. Approximately every 60 days, the argon will be saturated and the beam tube has to be heated to $100\,K$ and flushed by helium for regeneration. After that, a new layer of argon will be applied. The flushed out gas will be purged and the tritium will be reinjected into the WGTS. This part of the CPS is simulated and studied by the test experiment TRAP [Eic08].

In addition to this part of the CPS, another part with a NEG pump[5] is appended. Between the cryogenic one and the NEG pump section, the cold gate valve is installed to prevent flooding the spectrometers with tritium. It can be closed

---

[4]**F**ourier **T**ransform **I**on **C**yclotron **R**esonance
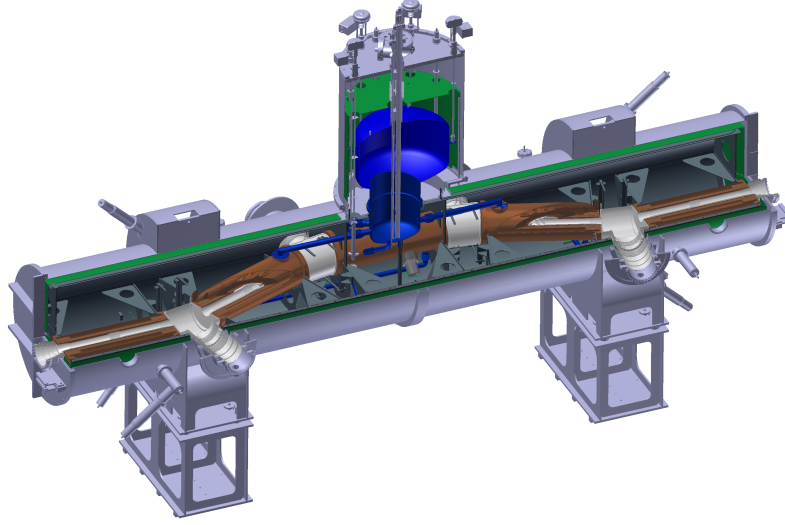[5]**N**on-**E**vaporable **G**etter pump

Figure 2.3.: Technical draw of the DPS2-F with its four pumps between each component, the magnets (brown) and the cryostat. Also the tilts of part two and four are illustrated [Rei13].
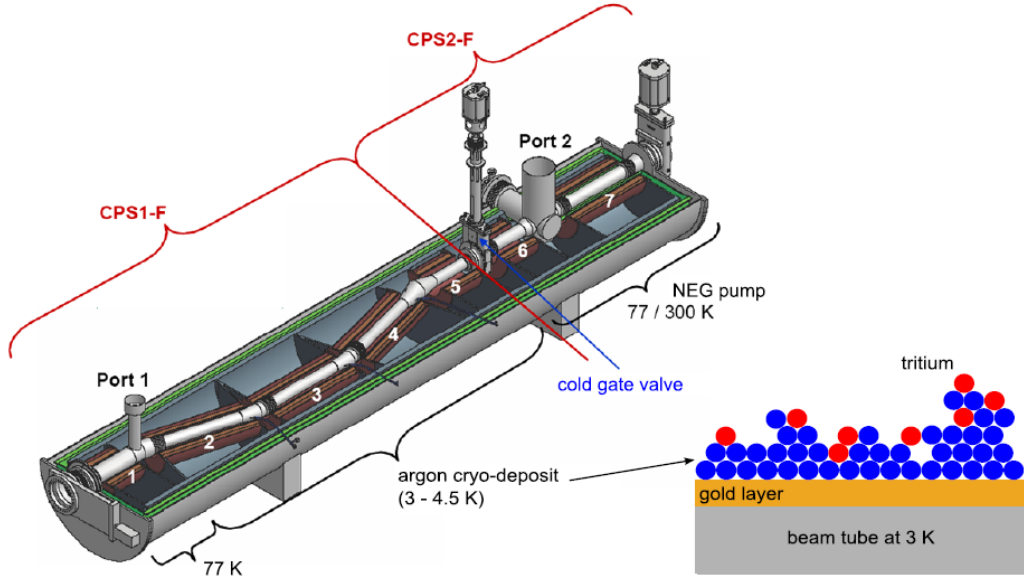

Figure 2.4.: Technical drawing of the CPS and the principle of the inner beam tube surface. The walls of the first five components are covered by a thin layer of Argon frost to adsorb Tritium. Beam line element 7 also houses a non-evaporable getter (NEG) pump [Bac12].

within a few seconds in case a system malfunction occurs. In this case, the NEG pump helps to preserve the ultra high vacuum inside the spectrometers [KAT04, GBB$^+$10].

2.2.3. Spectrometers

KATRIN utilizes three spectrometers, which are based on the MAC-E filter principle as described in section 2.1. In the following sections the pre-spectrometer, the main spectrometer and the monitor spectrometer will be described.

Pre-Spectrometer

The pre-spectrometer connects the transport section with the main spectrometer. This MAC-E filter has a length of 3.4 m and an inner diameter of 1.7 m. The retarding potential is fixed at -18.4 kV, thereby reducing the β-electron flux to the main spectrometer by a factor of 10^7. This is important to minimize the background, because the electrons could interact with residual gas and ionize them. Additionally, an ultra-high vacuum on the order of 10^{-11} mbar is required in the pre- and main spectrometer to minimize the background. This is one of the main challenges at the KATRIN experiment [Wol09]. The solenoids at the entrance and exit of the pre-spectrometer produce a magnetic guiding field of 4.5 T.

Since the pre-spectrometer has arrived at KIT in 2003, it was used as a prototype for the main spectrometer. Furthermore, several test experiments have been realized at the pre-spectrometer, such as testing of the vacuum and cooling systems, optimization of the electromagnetic design and investigation of various background sources, such as radon-induced background. As the latter subject is the main focus of this work, background sources are discussed in more detail in section 2.3 [FBD$^+$11, KAT04]

Main Spectrometer

The main spectrometer is a vessel with a length of 23.3 m and a maximal diameter of 10.0 m at its center. It follows after the pre-spectrometer and also has an ultra-high vacuum of around 10^{-11} mbar inside. To ensure the vacuum, at the rear end of the spectrometer three pump ports are located, which contain a total of six TMPs and NEG pumps. They provide an overall pumping speed of $10^6\,\ell\,\mathrm{s}^{-1}$ [Wol09]. The spectrometer scans the last 30 meV of the endpoint of the tritium spectrum and has therefore a retarding potential varying around -18.6 kV. The energy resolution is $\Delta E = 0.93$ eV (also see equation (2.3)).

The magnetic flux density varies between 0.0003 T and 6.0 T. The superconducting magnet between pre-spectrometer and main spectrometer provides a magnetic field of 4.5 T. The Pinch Magnet at the rear end of the main spectrometer induces the maximal magnetic field strength at KATRIN with $B_{\mathrm{max}} = 6.0$ T. Located in the middle of the spectrometer is the analyzing plane, where the magnetic field reaches its minimal value of 0.3 mT. For fine tuning and correcting the magnetic

field inside the vessel, two air coil systems are installed at the outside of the spectrometer. The EMCS[6] compensates the magnetic field of the earth. The LFCS[7] corrects interfering fields and ensures that the magnetic flux tube is contained into the vessel.

Inside the vessel a system of 28 000 wire electrodes is installed to avoid background from the walls. Therefore, the wire electrodes are set on a slightly more negative potential than the vessel. Electrons could be knocked out of the stainless steel due to interactions of cosmic muons (this background component is discussed in more detail in section 2.3.2). Because of the wire electrodes, low-energy electrons are electrostatically reflected back to the vessel surface, where they are absorbed. Hence, they do not reach the sensitive volume. This supports the background suppression with a factor of 10^2. A background suppression by a factor of 10^5 is achieved by the intrinsic *magnetic shielding* effect if the magnetic field is sufficiently axially symmetric. In addition to the background suppression, the wire electrodes will fine-tune the electrostatic field inside the vessel. This leads to optimized adiabatic transmission properties and prevents Penning traps.

Monitor Spectrometer

The modified Mainz spectrometer will be used at KATRIN to monitor the stability of the high voltage retarding potential at the main spectrometer. It is a vessel with a length of 3.5 m and a diameter of 1 m. This spectrometer is called Monitor Spectrometer and is located in a separate building, but fed with the high voltage of the main spectrometer. With the observation of the K32 line[8] of the ^{83m}Kr decay, the retarding potential of the main spectrometer can be monitored on the ppm level. For a second measurement, a precise voltmeter is used to determine the voltage after its transformation to low voltages using a high-precision voltage divider [Erh12, KAT04].

2.2.4. Detector

To detect the β-electrons from the tritium-decay, a silicon-based semiconductor FPD[9] is attached to the rear end of the main spectrometer. As the electrons are analyzed by the retarding potential at the spectrometer, the FPD only has to count the electrons. It is placed in a strong magnetic field $B_D = 3.6$ T to limit the maximal impact angle to 45°.

The PIN array with a diameter of 9 cm is divided into 148 pixels, where each pixel covers the same area. The segmentation happens radially and azimuthally.

Due to a moderate the energy resolution of $\Delta E < 1$ keV at 18.6 keV, the FPD is able to partially differentiate between background and signal events. In addition to that, a 10 kV PAE[10] is installed for further background reduction at the detector.

---

[6] **E**arth **M**agnetic field **C**ompensation **S**ystem
[7] **L**ow **F**ield **C**orrection **S**ystem
[8] Conversion electrons with an energy of $E = 17.8$ keV.
[9] **F**ocal **P**lane **D**etector
[10] **P**ost **A**cceleration **E**lectrode

The detector has to be sensitive to electron rates as low as 10^{-3} cps, while it has to tolerate rates up to 10^3 cps during calibration phases [Har12, KAT04].

2.3. Background Sources at the MAC-E Filter

An important challenge at KATRIN is to minimize the background to a 10^{-2} cps level. To fulfill this purpose, all background sources have to be well understood. In the context of this work, background sources at the pre- and main spectrometer have to be discussed. In the following sections, the principles of Penning traps, electrons from the surfaces and magnetically stored particles are shown.

2.3.1. Penning Traps

Electrons can be stored locally in volumes down to the order of cm^3 due to unfavorable combination of electrostatic potentials and magnetic fields. In case of a Penning trap, electrons are axially trapped within a potential well and radially confined due to being forced on cyclotron motions around the magnetic guiding field lines. The trapped electron ionizes residual gas atoms or molecules, thereby generating ions. These can escape the trap and ionize other atoms inside the spectrometer. The resulting tertiary electrons eventually reach the detector. The maximal potential difference defines the depth of the trap and hence determines the average number of ionizations per stored electron. Thus, a Penning trap can produce a large number of background electrons spread over a large volume [Mer12].

A Penning trap at KATRIN for example is located between the pre-spectrometer and the main spectrometer, which is a consequence of the high retarding potentials. To avoid this Penning trap, the pre-spectrometer can be operated at or close to ground potential. Simulations have shown, that such a setup does not have a negative influence on the β-electrons [Pra11].

2.3.2. Background due to Emission from Surfaces

Due to the large area of the main spectrometer vessel, $A_\mathrm{V} = 650\,\mathrm{m}^2$, and of the wire electrode system, $A_\mathrm{E} = 460\,\mathrm{m}^2$, there are two mechanisms for creating background electrons.

Secondary Emission: Electrons can be emitted from the surface of the stainless steel vessel when being hit by cosmic muons or high energy photons. The photons originate from natural radioactivity outside of the spectrometer or from radioactivity inside the spectrometer near the surface.

Field Emission: At sharp edges inside the main spectrometer at the wire electrode system or the surface of the vessel, high electric field strengths can arise. This leads to field emission, a quantum mechanical effect, where electrons tunnel out of the steel surface and eventually drift into the sensitive flux tube volume.

The fraction of electrons entering the sensitive flux-tube volume can be reduced by two mechanisms: the dominant part is the *magnetic shielding* and in addition the *electrostatic shielding*. For further details, see [Wan13, Rei13].

2.3.3. Background due to Magnetically Stored Particles

Electrons can be also stored due to the *magnetic mirror effect* [HIKO08]. Electrons which are produced inside the spectrometer have their longitudinal momentum transfered into transversal momentum when traveling towards the high magnetic field at the entrance and exit region of the spectrometer. In case of a full transformation, the electron is magnetically reflected back into the spectrometer. Now, if such an electron is stored, it will perform cyclotron motion around the magnetic field lines, magnetron motions around the spectrometer's symmetry axis and an axial motion along the magnetic field lines. While being stored, the electron scatters with residual gas molecules. Within these processes, the electron loses energy until it reaches the so-called trapping threshold, which is about 1 eV in standard operation mode. One of the possible energy loss mechanisms is the ionization of the residual gas. In this way, secondary electrons are produced over a long time which can reach the detector and appear as background electrons. The storage time depends on the pressure in the spectrometer [Wan13]. This background component is discussed in more detail in section 3.1.

The following sources are known to produce electrons that can potentially be stored in the main spectrometer:

Radon Decay: If a radon atom decays inside the spectrometer, it generates electrons which are able to be stored. Possible radon isotopes are ^{219}Rn, ^{220}Rn and ^{222}Rn, whereas ^{222}Rn is negligible, as the half life is too long such that these atoms will be pumped out of the vessel before they decay. This important background source is discussed in more detail in section 3 and [Sch14, Wan13, Mer12, Frä10]

Tritium Decay: It is possible, that Tritium reaches the main spectrometer despite all retaining mechanisms within the WGTS and transport section (section 2.2.1 and 2.2.2). It occurs in the form of HT molecules, which are mainly pumped out by the NEG pumps inside the pump ports at the main spectrometer. But the tiny amount of residual tritium produces a background which has to be taken into account [Wan13, Mer12].

To get rid of magnetically stored particles, *active* and *passive* background reduction methods have been studied (see section 3.1.3). Active methods, e.g., are the electric dipole, magnetic pulse [Wan13] or ECR[11] [Mer12] methods, which rely on the manipulation of the electromagnetic field configuration in order to remove stored electrons from the sensitive volume. The passive background reduction method utilizes a liquid nitrogen cooled baffle system [Gör14] to prevent radon atoms, emanating from NEG pumps, from entering the spectrometer.

---

[11]**E**lectron **C**yclotron **R**esonance

Table 2.1.: In this table the three magnetic field settings are listed with the corresponding observed flux tube volume.

Magnetic Field Setting in G	Flux Tube Volume in m^3
3.8	851.178
5.0	655.144
9.0	391.781

2.4. Spectrometer-Detector-System Commissioning Phase I

During summer 2013, the first spectrometer-detector-system (SDS) commissioning phase was completed, where the main spectrometer as well as the detector system were extensively tested. The spectrometer was operated at different voltages, magnetic field settings and pressures. In the context of this work, the variation of the pressure by argon is especially interesting. The transmission properties of the spectrometer were tested utilizing an angular-resolved quasi monoenergetic electron gun.

The majority of the measurements was performed using the following magnetic field settings: 3.8 G, 5.0 G and 9.0 G. The field strength defines the field at the analyzing plane (compare with a selection of measurements, table A.1). The stronger the magnetic field, the smaller is the observable volume inside the main spectrometer (compare table 2.1 and see figure 2.1). This is important for a major part of this thesis, discussed in section 4.

For the purpose of studying radon-induced background (see section 3.1), special measurements were carried out. As the storage time of electrons due to radon-decays correlates with the pressure[12], pressures of $\sim 10^{-8}$ mbar were used. This pressure range is called *high pressure* or *elevated pressure* as the *normal pressure* is about $\leq 10^{-10}$ mbar. During the commissioning phase, a vacuum of $\sim 10^{-10}$ mbar was achieved [BBB$^+$14]. This high pressure region is reached by flooding the main spectrometer with a constant flow rate with argon at a purity of 6.0, so 99.9999 % [BBB$^+$14]. Argon was chosen because it is a noble gas and hence neither sticks to the surface of the spectrometer vessel, nor does it saturate the NEG pump. While the main residual gas inside the spectrometer during normal pressure operations is molecular hydrogen, at the high pressure measurements the main scattering target for stored electrons has changed to argon. A potentially different behavior between molecular hydrogen and argon has to be investigated (see section 3.2 and 3.3) and taken into account for simulations and analyses. An advantage of argon is the similarity of its first ionization energy (15.76 eV [SM13]) to that of molecular hydrogen (15.43 eV [SM13]).

Also measurements for testing the baffle-system were performed. So data are

---

[12]The stored electrons have to cool down to a certain threshold to escape the trap. This happens via scattering with residual gas atoms and molecules. From this it follows that the threshold is reached faster if the scattering probability is increased by increasing the pressure.

taken at warm baffle as well as with cold baffle. In the latter case, ideally all radon-decays inside the sensitive volume will be suppressed and only background due to emissions from surfaces will be measured.

During the measurements, no signal electrons were generated, so in according to that, only background data were taken.

Following these commissioning measurements in 2013 the spectrometer was further optimized for tritium operation. Hence, a second commissioning phase (SDS-2) is scheduled for fall 2014 to finally prepare the spectrometer for tritium operation in 2016.

2. The KATRIN Experiment

3. ∎ Radon-Induced Background

The radon-induced background at the KATRIN experiment leads to a higher background rate than the design limit of 10^{-2} cps [KAT04].Therefore this important component was previously investigated in [Sch14, Wan13, Mer12, Frä10]. It turned out that decays of ^{219}Rn and ^{220}Rn introduce a non-Poisson distributed background component. Despite the fact, that radon is an α-emitter, also a few electrons are emitted, which fulfill the storage conditions partially and generate additional electrons through ionization. In the context of this work, those electrons are analyzed by using data from the SDS phase I (section 2.4) to determine the total radon activity inside the volume of the main spectrometer (see chapter 4).

In the following the developed radon background model from [Wan13] will be introduced (see section 3.1). Aspects of pressure dependence are discussed in section 3.2. Differences between cross-sections of hydrogen and argon and its impact on background due to stored particles are outlined in section 3.3.

3.1. Radon Background Model

To treat the radon-induced background properly, this background component has to be understood. A model of electron emission processes accommmpanying radon-α-decays at KATRIN is developed as described in [WDF$^+$13, Wan13]. It was found, that atomic shell processes like internal conversion, shake-off and kinds of relaxation produce a few electrons, which are able to get trapped. In this section this model will be briefly introduced. First, in 3.1.1 the storage mechanism is described and the generation of secondary electrons. In section 3.1.2 the atomic shell processes during the decay is discussed in particular. Finally, in 3.1.3 methods to address the radon-induced background are introduced.

3.1.1. Storage Mechanism and Background Electron Generation

Radon-decays inside the volume of the spectrometer can lead to magnetically stored electrons by the *magnetic mirror effect* [HIKO08]. This happens, if an electron travels from a region of lower magnetic field strength to a region of a higher field strength. Hence, the longitudinal energy $E_{\parallel}$ is transformed into transversal energy $E_{\perp}$. A total transformation of the longitudinal energy into the transversal energy occurs, when $E_{\perp}$ reaches a value above a certain threshold. In this case,

the electron will be reflected and will be stored until it no longer fulfills the storage conditions. Electrons traveling to areas of a higher magnetic field strength, gain $E_\parallel$ as the negative electrostatic potential will increase up to zero. The following equation

$$E_\perp^{\max}(\vec{p}_{\mathrm{s}}) = qU(\vec{p}_{\mathrm{s}}) \cdot \frac{B(\vec{p}_{\mathrm{s}})}{B_{\max}} \tag{3.1}$$

shows, that the electrostatic potential acts contrary to the reflecting magnetic field[1] ($\vec{p}_{\mathrm{s}}$ is the starting point of the electron, $E_\perp^{\max}(\vec{p}_{\mathrm{s}})$ denotes the maximal transversal energy for which the electron is not reflected[2], $U(\vec{p}_{\mathrm{s}})$ represents the electrostatic potential at the starting point and $B_{\max}$ is the maximal magnetic field strength). In consequence of equation

$$E_{\mathrm{kin}}^{\max}(\vec{p}_{\mathrm{s}}) = \frac{E_\perp^{\max}(\vec{p}_{\mathrm{s}})}{\sin^2 \theta_{\mathrm{s}}}, \tag{3.2}$$

electrons are more likely to be stored, if the starting polar angle θ_{s} is large. $E_{\mathrm{kin}}^{\max}(\vec{p}_{\mathrm{s}})$ denotes the starting kinetic energy.

Within the storage time, the electron is performing cyclotron motions around the magnetic field lines and moves along the symmetry axis of the spectrometer. In addition to that, it is also performing magnetron motions around the symmetry axis (see figure 3.1). In the meanwhile the electron will interact with residual gas molecules or atoms and in this way looses energy down to the storage threshold. At this point it is able to leave the trap. One possible interaction is the ionization of atoms. Therefore up to a few thousand secondary electrons are produced by one stored electron during the storage time. By getting accelerated by the retarding potential, the secondaries hit the detector and are not distinguishable from signal electrons. An important property is, that the storage time reaches up to several hours. Consequently one electron can generate background electrons extending over several hours. At a pressure of 10^{-11} mbar, the time between two interactions is about 10 s.

It depends on the energy, if the particle is stored. The lower bound of the energy is determined by the energy resolution of the spectrometer (see section 2.1) and is therefore set to 1 eV. If the energy falls below this value, the electron can escape the trap. As figure 3.2 illustrates, electrons with energies between ~ 10 eV and ~ 1 keV are most likely stored. At energies up to ~ 100 eV, the electrons can leave the trap in axial direction[3] (exit condition *z-position*). In the energy range of ~ 100 keV, the cyclotron radius exceeds the radius of the main spectrometer and the electrons will hit the wall. Thus, the probability of getting trapped decreases down to approximately zero within two orders of magnitude. If non-adiabatic motions are considered, the electron storage probability above ~ 1 keV is further suppressed.

---

[1] The electrostatic potential increases $E_\perp^{\max}(\vec{p}_{\mathrm{s}})$ as the particle is accelerated. The reflecting magnetic field $B_{\max}$, decreases $E_\perp^{\max}(\vec{p}_{\mathrm{s}})$.

[2] Do not confuse $E_\perp^{\max}(\vec{p}_{\mathrm{s}})$ with $E_\perp^{\max}$ from equation 2.3.

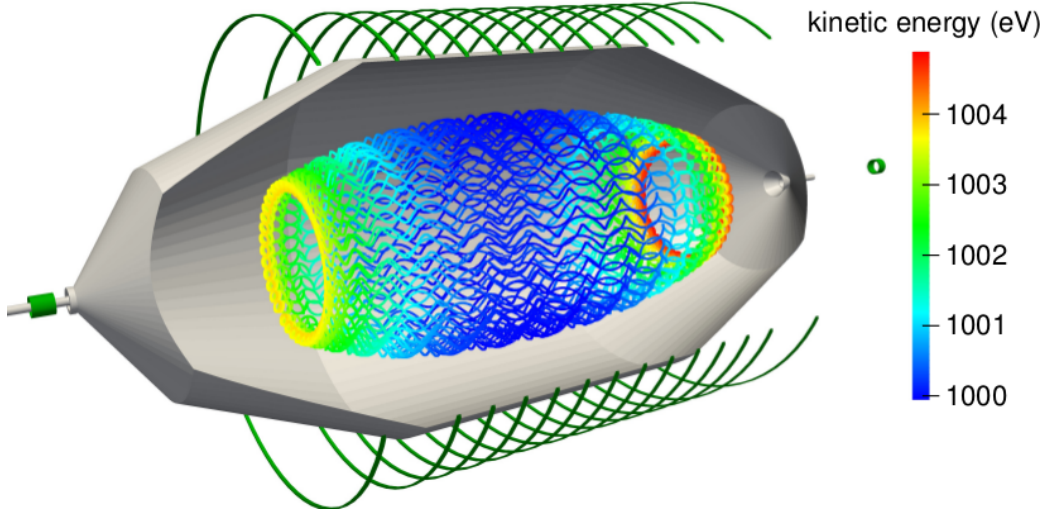[3] If an electron leaves the spectrometer towards either the entrance or the main detector.

Figure 3.1.: Visualisation of one magnetron motion of a trapped electron inside the volume of the main spectrometer. An 1 keV electron is started at the middle of the spectrometer at a radius of 3.5 m at this simulation with KASSIOPEIA [Wan13].
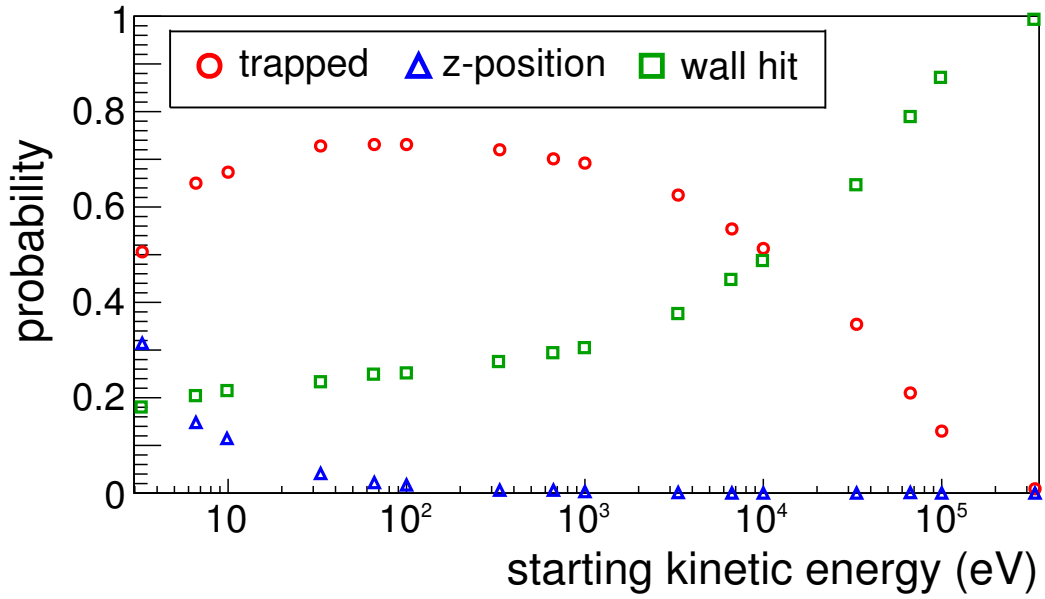

Figure 3.2.: Results of Monte-Carlo simulations with KASSIOPEIA. A central magnetic field strength of 0.35 mT was applied at the main spectrometer. The electrons were tracked until one of three termination conditions occurred (trapped, z-position or wall-hit). This plot is a result of simulation of homogeneous distributed electrons inside the main spectrometer with discrete energies between 3 eV and 300 keV [Wan13].

3.1.2. Electron Generating Processes by Radon

It was revealed, that the origin of the radon background is the vessel itself and the NEG pumps. Therefore it is a product of the decay chain of the primordial ^{232}Th, ^{235}U and ^{238}U. As radon is a noble gas, it is able to escape the steel easily, if the decay happens close enough to the surface. The area of the vessel is about $650\,\mathrm{m}^2$ ($25\,\mathrm{m}^2$ at the pre-spectrometer). The NEG pump stripes of the main spectrometer have a total length of $3\,\mathrm{km}$ ($90\,\mathrm{m}$ at the pre-spectrometer) and emits mainly ^{219}Rn. From the vessel, ^{219}Rn as well as ^{220}Rn is emitted. ^{222}Rn is negligible because of its half life of $t_{1/2}^{222} = 3.82\,\mathrm{d}$ [Son]. During this time, it is probably pumped out, because the pump out speed of radon has the value of $t_\mathrm{mainspec} \approx 360\,\mathrm{s}$ (at the pre-spectrometer $t_\mathrm{prespec} \approx 25\,\mathrm{s}$). In contrast the half life of the other two isotopes are $t_{1/2}^{219} = 3.96\,\mathrm{s}$ for ^{219}Rn and $t_{1/2}^{220} = 55.6\,\mathrm{s}$ for ^{220}Rn [Son]. However, they are able to decay homogeneously distributed inside the volume of the spectrometers[4]. During the decay into the daughter nuclei ^{215}Po respectively ^{216}Po, an important process for KATRIN appears: Despite the fact that it is an α-emitter, electrons are emitted. In the case of radon, there are several ways of generating up to 20 electrons per decay. The energy of these are in the eV range up to keV, see also figure 3.3. In the following, such processes are described.

Internal Conversion

The internal conversion (IC) process occurs, if the daughter nuclei is in an excited state. Hence it is able to interact electromagnetically with an inner electron and emits it. The probability of IC processes increases for heavy nuclei, as it is scaling with Z^3 [Sie68, TLMB08]. Other possibilities to get rid of the excitation state are radiative processes.

In this case, only the decay ^{219}Rn $\rightarrow$ ^{215}Po* is relevant, because the probability of an IC process increases for low-laying levels. This decay leads to two excited levels, namely $271.2\,\mathrm{keV}$ and $401.8\,\mathrm{keV}$. IC processes following the ^{220}Rn decay are rare as the daughter nucleus populates no low-laying excitation levels, only $549.7\,\mathrm{keV}$. Electrons due to IC from ^{215}Po* and ^{216}Po* with energies between $40\,\mathrm{keV}$ and $500\,\mathrm{keV}$ have been observed.

The overall IC probability resulting from radon-decay is about $3.3\,\%$ due to ^{219}Rn only. ^{220}Rn has a impact in the order of $\mathcal{O}(10^{-5})$, consequently it can be neglected.

An IC process leaves a vacancy in the inner atomic shell. This leads to relaxation processes as described after the section of *inner shell shake-off* electrons.

Inner Shell Shake-Off

Due to the α-decay, the shell electrons are getting perturbed by the outgoing α-particle and the resulting change of the nucleus' charge. But there are differences depending on the number of the shell. Electrons of the (K, L, M) shell bear a much higher velocity than the α-particle, which leads to an adiabatic change of

---

[4]The volume of the main spectrometer is $1240\,\mathrm{m}^3$, $8.5\,\mathrm{m}^3$ at the pre-spectrometer.
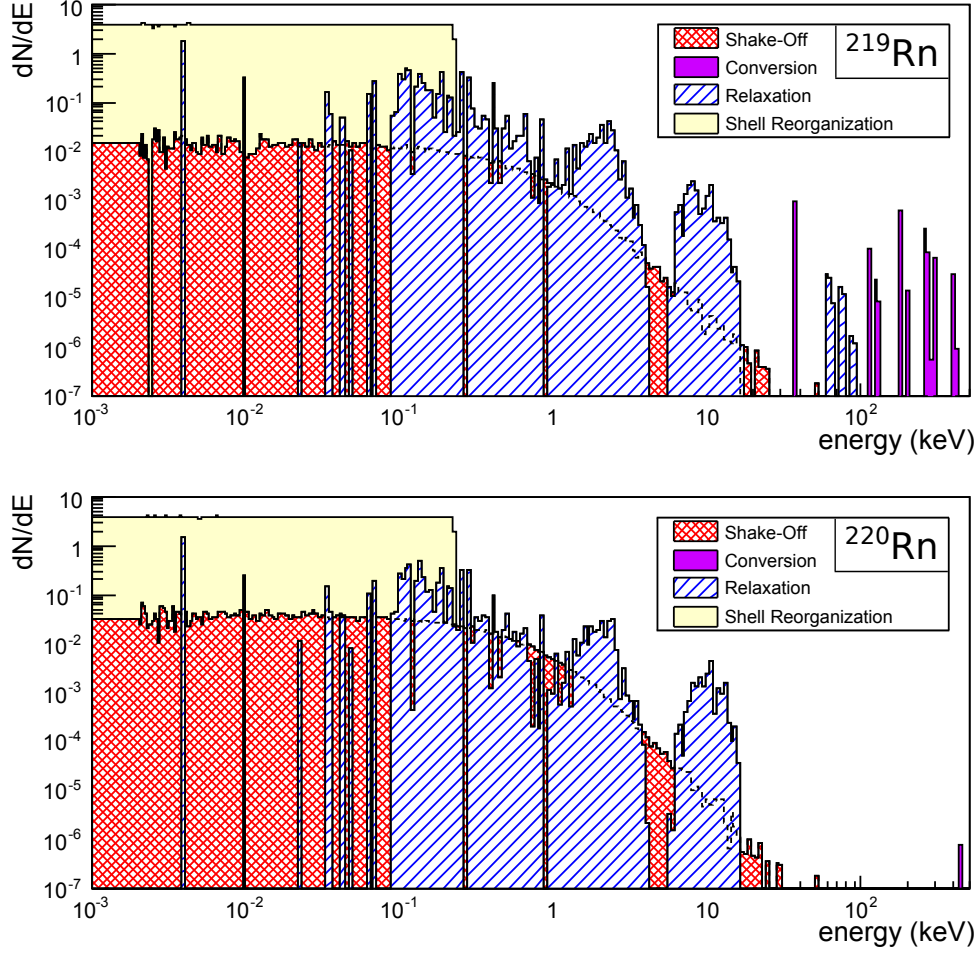
Figure 3.3.: Energy spectrum of the Radon model developed within [Wan13] for ^{219}Rn (top) and ^{220}Rn (bottom). In these spectra, internal conversion, inner-shell shake-off, relaxation and shell reorganization considered. The high-energy electrons ($> 100\,\text{keV}$), emitted accompanying to Radon-α-decays, are produced by internal conversion processes [Wan13].

the charge. The ratio of the velocities is about $v_\alpha/v_e \approx 0.1$, where v_α denotes the velocity of the helium nucleus and v_e the velocity of the electron. In contrast, the ratio for the outer-shells (N or higher) is about $v_\alpha/v_e \approx 10$. This causes a sudden change of the charge and therefore the electrons are still in the configuration of their parent atom. However, the inner electrons can interact electromagnetically with the outgoing particle and can be ejected to the continuum (shake-off) or to an excited level (shake-up). The transfered energy is close to the binding energy of the electron. The shake-off electron's energy spectrum is steeply falling and can be parametrized by the following equation [BH59],

$$N(E_{\text{shake}} = \left(\frac{E_b}{E_b + E_{\text{shake}}} \right)^8 , \tag{3.3}$$

where E_b denotes the binding energy and E_{shake} the kinetic energy of the electron. The probability for shake-off processes of ^{210}Po is used in [Wan13] as a good approximation for ^{215}Po and ^{216}Po. It has an amount of 1.6×10^{-6} for the K-shell [RAP75a] and rises up to 1.8×10^{-2} for the M-shell [RAP75b].

Shake-off electrons leaf also a vacancy within the atomic shell, which leads to relaxation processes as described below.

Relaxation Following Internal Conversion and Shake-Off

As IC and shake-off processes produce vacancies at the atomic shell, a rearrangement of the shell follows, called relaxation. There are two possibilities: A radiative way, and a non-radiative way. In context of KATRIN, only the non-radiative way is of interest, because it will emit further electrons. This happens via Auger or Coster-Kronig electrons.

In the case of a non-radiative process, an electron is emitted by occupying the vacancy by another electron. As the transition-electron[5] releases the difference in binding energy and transfers it to another electron, which will emitted. It leads to two vacancies, triggering more such processes. So, large cascades can occur, so-called *Auger explosions*. The remaining nucleus is highly positively charged. This ion is potentially neutralized by interacting with the vessel's wall. This leads to an implementation of the ion into the wall, which happens within a time of $\mathcal{O}(10^{-6})$s in comparison of the half life of ^{215}Po ($t_{1/2}^{215} = 1.781$ ms) and ^{216}Po (($t_{1/2}^{216} = 145$ ms) [Son]. Thus, the decay of polonium daughter nucleus is not an issue for KATRIN (it is a consequence of the *magnetic shielding* and *electrostatic shielding* [Wan13, Rei13]).

The energy of the emitted electrons can reach from mainly < 100 eV up to 93 keV. In the case of KATRIN, the exact multiplicity of electrons was not the focus of [Wan13], because the ionization due to high-energy IC and shake-off stored electrons causes several thousand electrons as mentioned above.

---

[5]If it is an electron from an outer shell, the emitted electron is called *Auger electron*. If it is an electron from a neighboring sub-shell, it is called *Coster-Kronig electron*.

Atom Shell Reorganization

If the atomic shell is left approximately unperturbed by the α-particle or the emitted electron originates from the outer-shells (N or higher), the process of the shell reorganization can be calculated more easily than in the way mentioned above. This happens, because the outer electrons do not adjust adiabatically to the changed charge and remain in their original shell configuration.

The electrons' energy, which are emitted by shell reorganization, have to be estimated, as there exists no experimental data. By using relativistic Hartee-Fock-Slater calculations of [LCM$^+$71], the change of the charge of $\Delta q = 2e$ leads to a different binding energy of $\Delta E = 37.7\,\text{keV}$. ΔE is a composition of a sudden component ΔE_{sud} and a much slower rearrangement component ΔE_{R} [Fre74]. ΔE_{sud} is dominant for the outer shells, as the change of the charge happens suddenly. The fraction of ΔE_{R} is typically in the order of $\mathcal{O}(10^{-2})$. The energy change ΔE is fed by the outgoing α-particle, that decelerates this particle. So, the average outer shell rearrangement energy is about $250\,\text{eV}$ [Fre74] and is statistically shared by the two outermost electrons. As their kinetic energy is higher than the binding energy for polonium at the P-shell, they escape into the continuum.

This is the most probable electron emission process during α-decays, because shake-off electrons from the inner shell are not frequent.

3.1.3. Suppressing Methods

The fact, that radon exceeds the design limits of KATRIN for background rates [KAT04], led to the development of several methods to get rid of the stored particles. This results in a significant background suppression. In this section four methods are briefly introduced which are investigated within three PhD thesis: Magnetic pulse and electric dipole [Wan13], ECR[6] [Mer12] and a liquid nitrogen cooled down chicane, called *Baffle* [Gör14]. They are divided into *active* and *passive methods*.

Active Methods

The active methods includes magnetic pulse, electric dipole and ECR. These three methods have in common, that they remove stored electrons after they got trapped. In contrast, the passive method avoids trapped particles.

With a magnetic pulse, the stored electrons can be removed by reducing the magnetic field strength in a large area of the spectrometer. At the main spectrometer, it is realized by the LFCS[7], and the magnetic field is changed at the analyzing plane. Therefore the magnetic guiding lines come closer to the vessel wall or hit them. Hence the stored electrons are absorbed. Removing the magnetic field completely from the middle, all guiding lines lead the stored electrons to the walls. This leads to three accompanying effects:

---

[6]**E**lectron **C**yclotron **R**esonance
[7]**L**ow **F**ield **C**orrection **S**ystem

First, the reduction of the magnetic field causes larger cyclotron radii. This benefits the absorption of the electrons. Second, by changing the magnetic field, an electric field is inducted. This causes an $\vec{E} \times \vec{B}$ drift towards the walls (compare with the electric dipole method). And third, the magnetic field lines, which are terminated at the walls, can guide electrons (produced by muons) from the wall into the spectrometer and induce new background electrons.

An electric dipole also induct an $\vec{E} \times \vec{B}$ drift by using the inner wire electrode system of the main spectrometer, so that the electrons are drifting in one direction. If the field strength is sufficient, they hit the spectrometer's wall during one magnetron motion. Otherwise, they return to their starting point.

The ECR method uses a stochastic heating of the stored electrons. A high-frequency (HF) source is applied at the analyzing plane. Every time the electrons pass this plane, they gain energy through a stochastical process. This leads to a large cyclotron radius. If the transversal energy is higher than $\sim 100\,\text{keV}$, the cyclotron radius is larger than the vessel's diameter. Thus, they hit the wall. To heat them up, the frequency has to be chosen accordingly to

$$\omega_{\text{c}} = \frac{eB}{\gamma m_{\text{e}}}, \tag{3.4}$$

where e denotes the electron's charge, B the magnetic field, m_{e} the mass of the electron and γ the Lorentz factor. Because of γ, the cyclotron frequency changes very slowly with increasing energy of the electron. In the case of KATRIN, it causes only a change of $5\,\%$ of the energy. Thus, the applied HF has not to change and is able to heat up electrons at all occurring energies[8].

All these methods have in common, that during electron removal no data for the neutrino mass can be taken.

Passive Methods

The passive method consists of a liquid nitrogen (LN2) cooled baffle system. It is constructed such that a straight line of view is prevented by using V-shaped copper sheets. As it is cooled down by LN2, it acts as a kind of cryo-pump and adsorbs the radon as long until it decays. This is important as it showed, that the NEG pumps are emitting ^{219}Rn. So, because they are located inside the pump ports at the rear end of the main spectrometer (compare figure 2.2), the baffle system is installed between the entry to the vessel and the pumps (see figure 3.4). The radon is inhibited to reach the sensitive flux-tube volume and the background due to radon-decays is suppressed. Accordingly, this is a totally different method to get rid of the radon-induced background and is therefore distinguished from the active methods.

---

[8]All energies, resulting in trapped electrons.
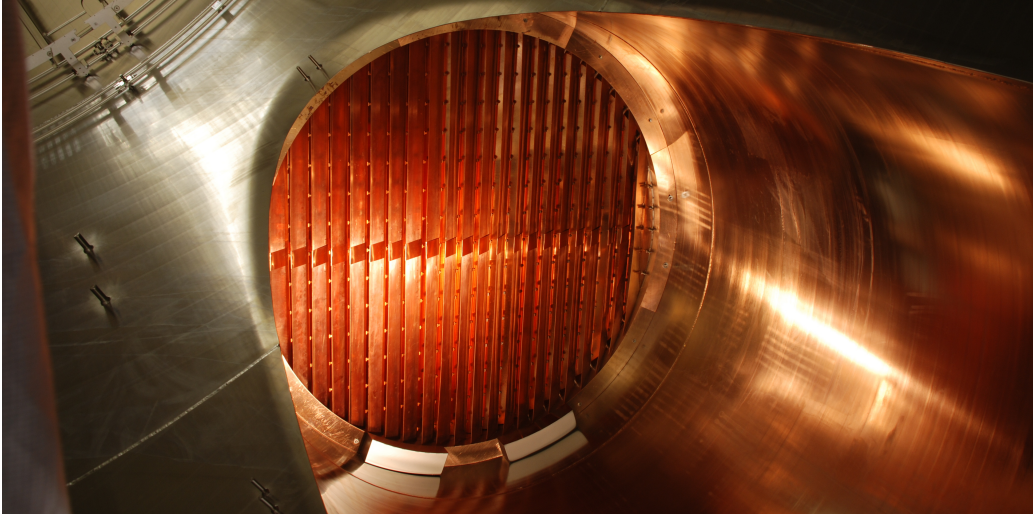
Figure 3.4.: View from the inside of the main spectrometer at the baffle system of pump port III. The V-shaped copper and cooled by LN2 sheets avoid a straight line of view into the pump port. So, the radon, which is emitted by the NEG pumps, is hitting the baffle and is adsorbed for a time longer than its half lifetime. Photo taken by M. Zacher in 2012.

In addition, the radon emitted by the vessel's wall also can be adsorbed by the baffle system. In the best case, it removes all radon atoms[9].

By designing this system, it has to be ensured that the pumping speed of hydrogen and tritium is still sufficient.

3.2. Pressure Dependence

The pressure inside the spectrometer has an immediate impact on the storage time. The pressure defines the number of particles inside the volume, which affects together with the total cross-section the mean free path leading to a different mean free time. Using these simple assumptions the correlation between the time of storage t_{storage} and the pressure p resolves to

$$t_{\mathrm{storage}} \propto \frac{1}{p}. \tag{3.5}$$

Consequently, the storage time increases (decreases) if the pressure decreases (increases). This leads to a simple factor for stretching or shrinking the storage time by changing the pressure. If the storage time t'_{storage} at pressure p' should be

---

[9]The velocity of the radon atoms is high enough, that they most likely hit the copper wall before they decay.

calculated from the time t_{storage} and the pressure p, it results in

$$t'_{\text{storage}} = \frac{p}{p'} \cdot t_{\text{storage}}. \tag{3.6}$$

As it is needed in section 4.6.2, an example is given for $p = 10^{-8}\,\text{mbar}$ and $p' = 10^{-10}\,\text{mbar}$: $p/p' = 100$ (compare section 2.4).

Additionally, non-adiabatic effects do have an impact on the number of secondaries per stored particle [Wan13]. The stored electron can escape by falling below the maximum energy for not getting trapped, $E_{\text{kin}}^{\text{max}}$, or the polar angle enters the loss cone, which is defined by the maximal polar angle θ_{max} (see equation (2.4) and (3.2)). As high-energy electrons (with energies above several keV) are guided non-adiabatically, so μ is not constant anymore, the polar angle is able to change virtually uncontrolled by the guiding field. For specific starting conditions of the electron the angle can change in such a way that the electron ends up in the loss cone. Hence, the electron escapes the trap without storing the residual energy as ionization. Consequently, less secondaries are produced. It is also possible, that such an electron does fulfill the starting conditions and will never end up in the loss cone without scattering despite it is affected by non-adiabatic processes. At each scattering process the polar angle changes. As the phase space of the loss angle is small, there is a high probability for an increased distance to the loss cone. Consequently, scattering processes will prevent electrons to escape the trap by changing the angle away from the loss cone's neighborhood. The higher the pressure, the more secondaries are generated, as more electrons will still be trapped until their transversal energy falls below the local threshold.

This effect can be estimated by comparing the radon-induced background rate at $10^{-10}\,\text{mbar}$ and $10^{-8}\,\text{mbar}$. The rate at $10^{-8}\,\text{mbar}$ is calculated based on the analysis within section 4 and is approximated to $r_{\text{Rn}}(10^{-8}) = (569.8 \pm 2.0)\,\text{mcps}$. At $10^{-10}\,\text{mbar}$, the rate is yielded by baffle-measurements [BBB^{+}14] during SDS-1 (see section 2.4):

$$\begin{aligned} r_{\text{Rn}}(10^{-10}) &= r_{\text{warm-baffle}} - r_{\text{cold-baffle}} \\ &= (519.6 \pm 3.2)\,\text{mcps} - (219.7 \pm 4.7)\,\text{mcps} \\ &= (299.9 \pm 5.7)\,\text{mcps}. \end{aligned} \tag{3.7}$$

This leads to a ratio of the rates between those pressures of $r_{\text{Rn}}(10^{-8})/r_{\text{Rn}}(10^{-11}) = 1.90 \pm 0.09$. So, the number of secondaries increases by elevating the pressure, in particular from $10^{-10}\,\text{mbar}$ to $10^{-8}\,\text{mbar}$, the rate increases with the factor of ≈ 2.

3.3. Argon and Hydrogen Cross-Sections

The storage time of trapped particles scales not only with the pressure (see previous section) but obviously also with the cross-sections of the gases and the energy-loss per interaction. The higher the cross-sections (energy-loss) the earlier the particle's
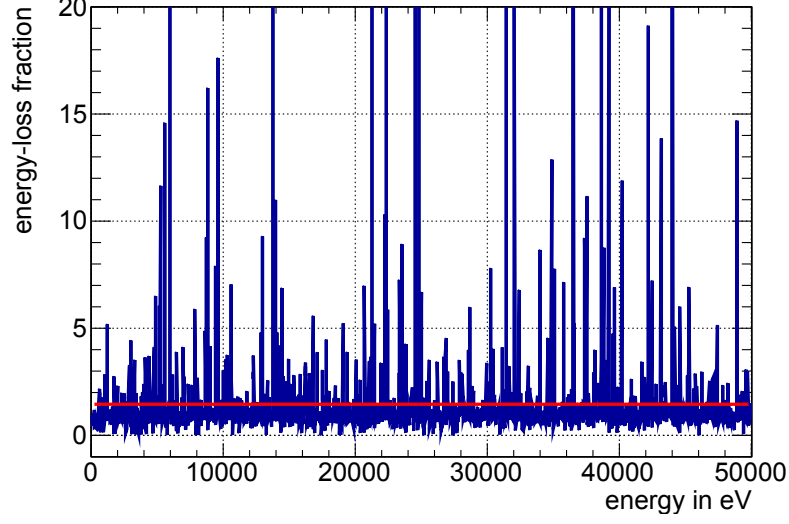
Figure 3.5.: Comparison of energy-loss of argon and hydrogen. KASSIOPEIA3's scatter-model was utilized to get the result of the fraction $E_{\text{loss}}^{\text{Ar}}/E_{\text{loss}}^{\text{H}_2}$. The mean value is the result of a fit in a region from 20 eV to 50 keV.
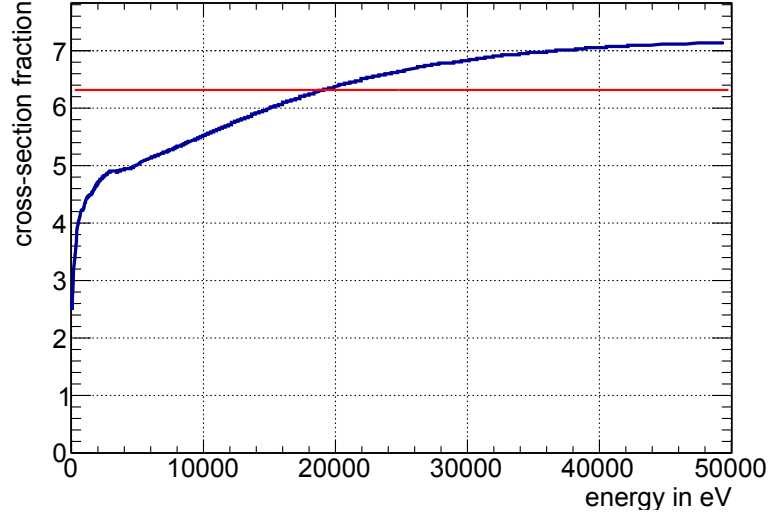

Figure 3.6.: Comparison of cross-section of argon and hydrogen by using KASSIOPEIA3's scatter-model. The mean value of the fraction $\sigma_{\text{Ar}}/\sigma_{\text{H}_2}$ is obtained from a fit in the region from 1 eV to 50 keV.

energy will fall below the storage threshold. As in this work data with argon as main scatter target are analyzed, in the following the molecular hydrogen and argon cross-sections and energy-losses are compared for estimating its impact to the storage time.

As a first step, the mean energy-loss is compared by using KASSIOPEIA3's scattering-model for hydrogen and argon. The energy-loss due to the particle's energy was evaluated between $20\,\mathrm{eV}$ and $50\,\mathrm{keV}$. For comparison, the fraction of $E_{\mathrm{loss}}^{\mathrm{Ar}}/E_{\mathrm{loss}}^{\mathrm{H_2}}$ is calculated and shown in figure 3.5. As only a rough approximation is necessary, the mean energy-loss at this energy range is fitted. So, the fit yields a value $\eta_{\overline{E_{\mathrm{loss}}}} \approx 1.5$. That means, that the energy-loss per scattering with argon is about a factor of 1.5 times higher than with hydrogen. This results in 1.5-fold longer storage times for hydrogen in case of an extrapolation from argon as main scatter target to hydrogen.

In figure 3.6, the fractions of the total cross-sections $\sigma_{\mathrm{Ar}}/\sigma_{\mathrm{H_2}}$ is shown in a range of $1\,\mathrm{eV}$ and $50\,\mathrm{keV}$. The mean quotient is obtained by a fit, which results approximately in $\eta_{\sigma} \approx 6$. Thus, the storage time increases by a factor of 6 for an extrapolation from argon as main scatter target to hydrogen.

As a result, the stretching of storage time extrapolated from argon to hydrogen is based on the previous estimations (energy-loss and cross-section) in order of a factor nine.

4. Analysis of Background Measurements at Elevated Pressure

The main focus of this thesis is the investigation and analysis of measurements at the main spectrometer taken during the first commissioning phase of the spectrometer-detector-system as described in section 2.4. The pressure was artificially increased by flooding the spectrometer with Argon, which will not contaminate the spectrometer due to its poor chemical reactivity. As the storage time of electrons anti-correlates with the pressure due to an increased scattering probability (see section 3.2), measurements were taken using an elevated pressure of about 10^{-8} mbar. This, resulting in a maximal storage time of about 200 ms. Thus, most probably just one electron is stored inside the main spectrometer at any time. The probability for two particles being stored simultaneously is of the order of 10^{-4} to 10^{-5} (see section 4.6.1). These conditions are advantageous for the investigation of single radon-decays, for the estimation of the total radon activity and the results can be used to extrapolate to the background expected at nominal pressure.

In this chapter the analysis of high-pressure-data is described in detail for measurements performed with the 9 G-setting (see table A.1). The results for measurements at the 5 G-setting are shown in the appendix A.4. The basic method for separating two background components is discussed in section 4.1. Sections 4.2 and 4.3 detail the radial background distribution and radon-spike characteristics, followed by a major objective of this thesis, the estimation of the radon activity in section 4.4. Of particular interest is the understanding of the distribution of secondaries per radon-decay, the so-called *multiplicity*, which in turn allows to determine correction factors for low multiplicity events, as these are not automatically found by the method described in 4.1, discussed in section 4.5. Applying these corrections to the activity determined in section 4.4 yields the real total radon activity inside the main spectrometer. In section 4.6, the measurement of the storage time is described and finally a background estimation for pressure settings of 10^{-10} mbar and 10^{-11} mbar is given.
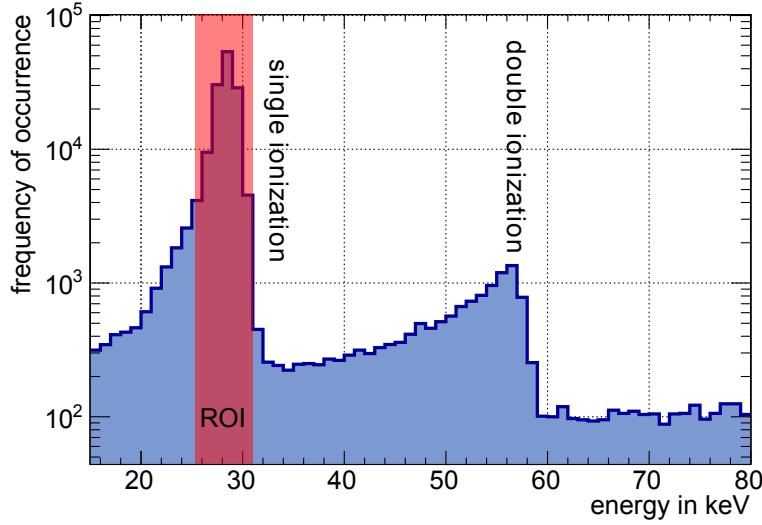
Figure 4.1.: Energy spectrum of electrons detected at the FPD (9 G-setting). The *single ionization* peak, caused by single electron impact, is within the region of interest (ROI). The initially low-energetic electrons ($\mathcal{O}(\mathrm{eV})$) are accelerated by the retarding potential $-18.6\,\mathrm{kV}$ and the post acceleration electrode ($-10\,\mathrm{keV}$). The *double ionization* peak is caused by the simultaneous (within $50\,\mathrm{ns}$) impact of two electrons, presumably produced via double ionization of argon.

4.1. Separation of Background Components

A very important step in this analysis is the separation of the individual background components. As mentioned in section 2.4, no signal electrons are involved, thus, only background data are taken. In the context of this thesis the radon-induced background component is the subject of interest. As described in section 2.3, there are three known background sources in the spectrometer: muon-induced, radon-induced and Penning-trap-induced background. During SDS-1, the pre-spectrometer was not connected, hence no Penning traps are expected. Therefore, only electrons originating from stored particles and the surface have to be considered. Also, tritium-induced background is negligible since no source was connected.

For the following analysis, only events with energies in the region of interest (ROI, between $25.6\,\mathrm{keV}$ and $30.6\,\mathrm{keV}$) are considered. The energy spectrum measured between $15\,\mathrm{keV}$ and $80\,\mathrm{keV}$ is shown in figure 4.1, where the first peak ($28.6\,\mathrm{keV}$) is in the ROI. It results from the impact of a single low-energy electron which is accelerated by the retarding potential ($\sim -18.6\,\mathrm{kV}$) and the PAE[1] ($-10\,\mathrm{kV}$). The second much lower peak at $57.2\,\mathrm{keV}$ is a result of double ionization

---

[1] **P**ost **A**cceleration **E**lectrode
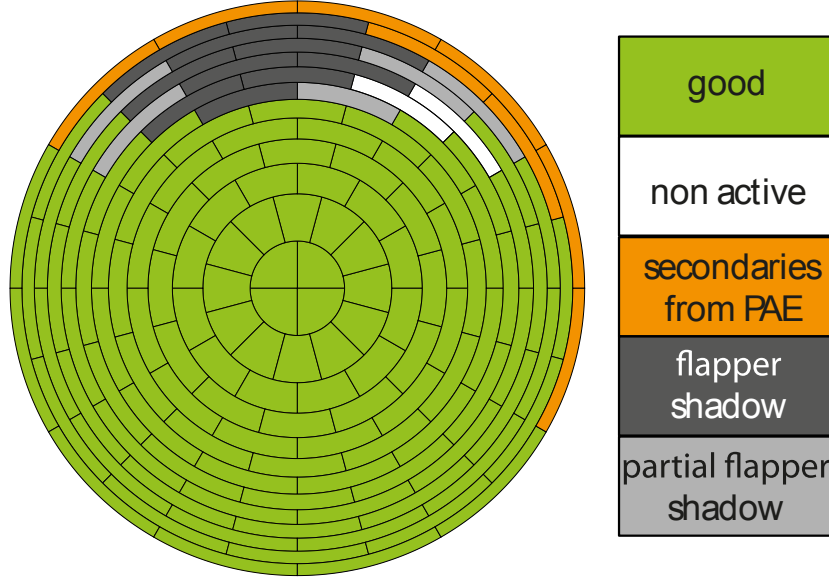
Figure 4.2.: Map of pixels status during commissioning. Several pixels cannot be used for the analysis due to the following reasons: two pixels are inactive due to a short circuit (white), see background electrons coming from the surface of the PAE (orange), eleven pixels are shadowed by the flapper-valve (dark-gray) while five pixels show a partial shadow (light-gray) [BBB$^+$14].

of argon[2]. Two angular-correlated electrons are produced simultaneously by ionization and reach the detector within a narrow time interval. Due to the limited time resolution of the detector (~ 50 ns), they appear as a single electron with twice as much energy. Also twin-events due to one electron inducing responses on two pixels within 2×10^{-6} s are identified and commutated. They appear within the ROI. The analyzed runs for the 9 G-setting are #8547 to #8567.

Certain pixels (26 out of 148, shown in figure 4.2) were excluded from the analysis for the following reasons: Two pixels[3] were deactivated due to an electrical short circuit. Eight pixels[4] show an increased background due to field lines connecting to the PAE, guiding electrons produced by secondary emission to the detector. This effect is caused by a tilt of the magnets with respect to the axis of the PAE, which will be improved for SDS-2. Additionally, the flapper valve between the spectrometer and detector system, which cannot be fully retracted due to a malfunction, causes a full shadow on eleven pixels[5] and a partial shadow on five pixels[6]. For further details refer to [BBB$^+$14].

In this analysis, the background is assumed to consist of two components: mag-

---

[2]Double ionization does not occur with Hydrogen, which dominates at nominal pressure.
[3]Pixels #78 and #89.
[4]Pixels #125, #126, #136, #137, #138, #139, #140 and #147.
[5]Pixels #67, #79, #80, #90, #91, #103, #104, #114, #115, #127 and #128.
[6]Pixels #66, #92, #102, #113 and #116.
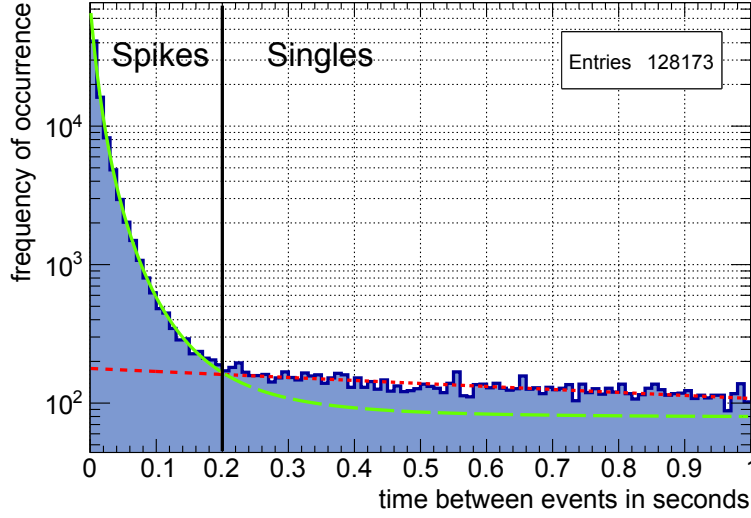
Figure 4.3.: Time between two consecutive detector hits (interarrival-time Δt) during measurements at 10^{-8} mbar and 9 G-setting. An exponential and a flat background component were fitted to the data, intersecting at 0.2 s. The events with $\Delta t < 0.2$ s (solid line, *spikes*) originate mainly from stored particles, while events with $\Delta t > 0.2$ s (dotted line, *singles*) are generated by emissions from surfaces.

netically stored particles (in particular radon-induced) and emissions from surfaces. While the emissions from surfaces are Poisson-distributed, the background events due to stored particles are correlated and as a consequence not Poisson-distributed. This is a result of two Poisson-distributed processes. First, the nuclear decay of radon which can create electrons and second, the ionization of residual gas molecules if this electron happens to be stored. These two background components are distinguishable by their characteristic distribution of the interarrival-time[7] Δt, which is shown in figure 4.3. Events at small Δt, which follow an exponential distribution, originate mainly from stored particle induced background. They are called *spike* (*-events*) or *radon-spikes*. Events at larger Δt follow a flat distribution as expected from e.g. muon-induced surface emissions. Accordingly they called *single events* or *singles*. The separation time (0.2 s) is derived by applying fits to each component and extrapolating to the intersection point. These fits are shown in figure 4.3: The solid line is the fit of the background due to radon and the dotted line the background due to singles.

Figure 4.4 (left) shows a randomly chosen time window of 1000 s of the detector rate with a one-second binning during a background measurements. Among rates about 0 to 2 cps there are excessive rate increases during mostly less than one second. These *spikes* are due to stored particles and their production of secondaries, which is further underlined by the characteristic spatial distribution of events on

---

[7]The interarrival-time is defined as the time between two consecutive detector hits.
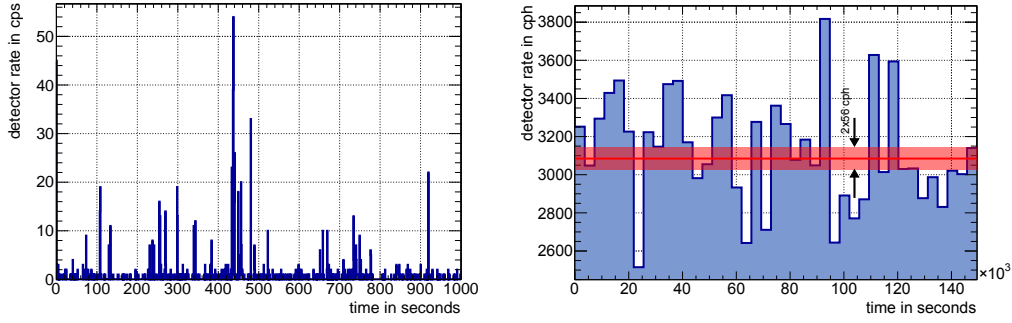
Figure 4.4.: Detector rate during measurements at 10^{-8} mbar and 9 G-setting. (left) Shown is a random 1000 s time window with a one-second binning. Increased rates over a short period of time (*spikes*) are caused by single high-energy stored electrons which cool down via ionization of residual gas molecules. (right) The detector rate for the entire measurement. Even with the chosen one-hour binning, large rate fluctuations can be observed, underlining the non-Poissonian behavior of this particular background component. The average rate and the expected standard deviation by a Poissonian behavior are included.

the detector (see figure 4.5). The visible ring structure is a result of the magnetron motion around the spectrometer symmetry axis performed by the stored particle (compare also figure 3.1). Based on the detector rate the non-Poisson behavior of the radon-induced background can be shown very well. In figure 4.4 (right) the detector rate during the entire exposure time is plotted. Used is a one-hour binning to make the non-Poisson behavior obvious. The average detector rate is determined to 3088 cph. If the rate is Poisson-distributed, the standard deviation is equal to the square root of the numbers of events within that time bin $\sqrt{N}/T = 56$ cph. However, the calculated standard deviation significantly exceeds this value: $\sigma = 287$ cph.

Following the separation method outlined above, radon-spikes are selected by an interarrival-time cut at 0.2 s. A second selection criterion is applied. The *cluster-size N*, which is the number of secondaries within a spike-event, has to exceed a certain minimal threshold. This threshold affects the impact of the singles to the spike detection. A lower threshold results in more singles being falsely tagged as *spikes*. Hence, a higher threshold results in a better discrimination of radon-induced events. As radon-induced background is the focus of this thesis, a threshold of $N_{\mathrm{min}} = 3$ is chosen.

The average total detector rate in the region of interest within the analyzed data is about (857.7 ± 2.4) mcps, with (569.8 ± 2.0) mcps being radon-induced and (232.0 ± 1.2) mcps due to singles $(\Delta t > 0.2 \text{ s})$.
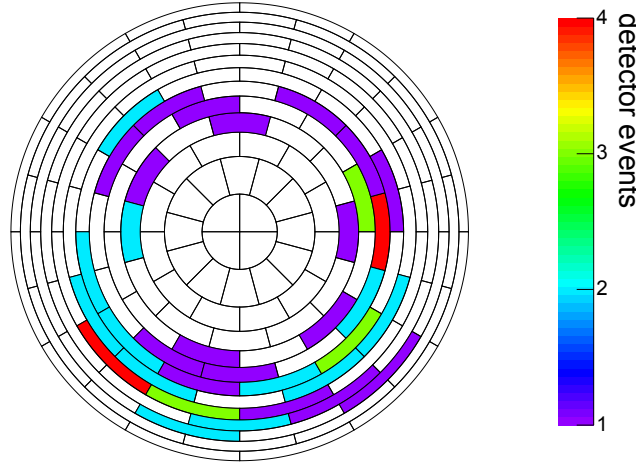
Figure 4.5.: Accumulated hits on the individual detector pixels during a radon-spike at 9 G-setting. Due to the magnetron motion of the stored particle, a ring structure is visible.

4.2. Radial Background Distribution

The radial dependencies of the individual background components at the 9 G-setting (see section 2.4) are shown in figure 4.6. The background rate as observed by the individual detector rings is normalized to the volume and is plotted as a function of the corresponding radius at the analyzing plane. Especially at larger radii, the behavior of radon-induced and single background is different. The radon-induced background decreases towards larger radii. This is a result of the storage conditions. Since the cyclotron radius increases with increasing kinetic energy, only low-energy particles can be stored on outer field lines[8]. Since the background is proportional to the energy of the stored particle, a lower background rate is expected at larger radii. In contrast, the radial behavior of singles is reversed: The rate is higher at large radii and decreases towards smaller radii. This results from the fact that these electrons originate from the vessel surface and their penetration into the flux tube is suppressed by the magnetic shielding effect.

In order to validate the Δt cut introduced in this section, the results are compared to measurements utilizing the liquid nitrogen cooled baffles (see section 2.4). It is assumed that the baffle is highly efficient (close to 100 %) in removing the radon-induced background component. Therefore the remaining background [BBB+14] should be compatible with the singles component of the analysis performed here. The comparison is shown in figure 4.7. The shape of the curves is very similar, underlining the validity of the Δt cut. The discrepancy can be ascribed to radon-induced single background, which cannot be distinguished from surface emission-induced singles utilizing the Δt cut. This is discussed in more

---

[8]Electrons are assumed to be absorbed upon hitting the spectrometer vessel.
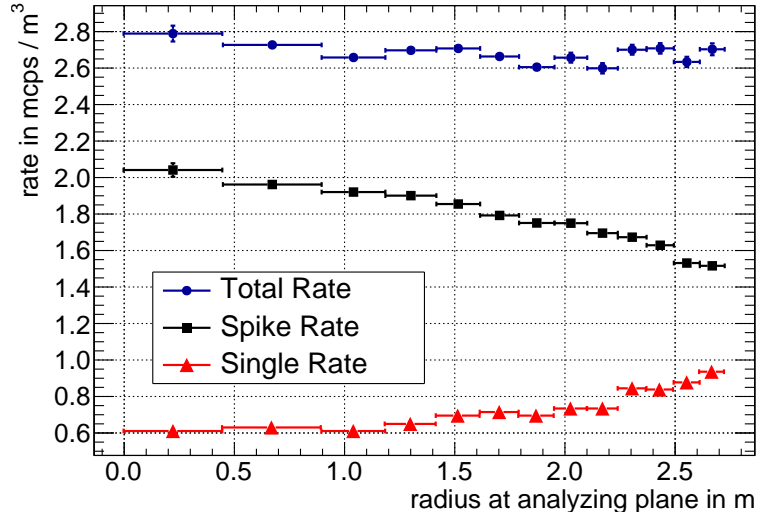
Figure 4.6.: Radial background distribution at 9 G-setting: The total rate does not show a significant radial dependence. In contrast, events due to *spike* and events due to *singles* do have a contrary behavior at larger radii. Electron storage is most efficient in the center of the spectrometer, leading to spikes predominantly at smaller radii. Singles, however, originate from surface emissions and hence are expected to dominate at larger radii.

detail in section 4.5.1.

4.3. Spike Characteristics

As shown in section 4.1, the magnetron motion performed by the stored electron is reflected by the ring-like hit pattern on the detector (compare figure 4.5). These ring structures can be investigated in more detail. The radial spike distribution can be investigated much in the same way as the radial background distribution discussed in section 4.2. For this purpose, each radon-spike is analyzed on event-by-event basis where the average hit ring and the standard deviation are calculated. Figure 4.8 (left) shows, the spike rate observed by the individual detector rings normalized to the volume corresponding to the ring as a function of the corresponding radius at the analyzing plane. It shows a slight increase of the rate until reaching the maximum at ring #8, which corresponds to a radius of 2.2 m. Thereafter, the rate decreases steeply. This agrees with the results shown in figure 4.6, although the decrease starts at much smaller radii in that case. This observation is reasonable when taking into account the multiplicity of a radon-spike as a function of the radius of the corresponding particle track in the analyzing plane (figure 4.8
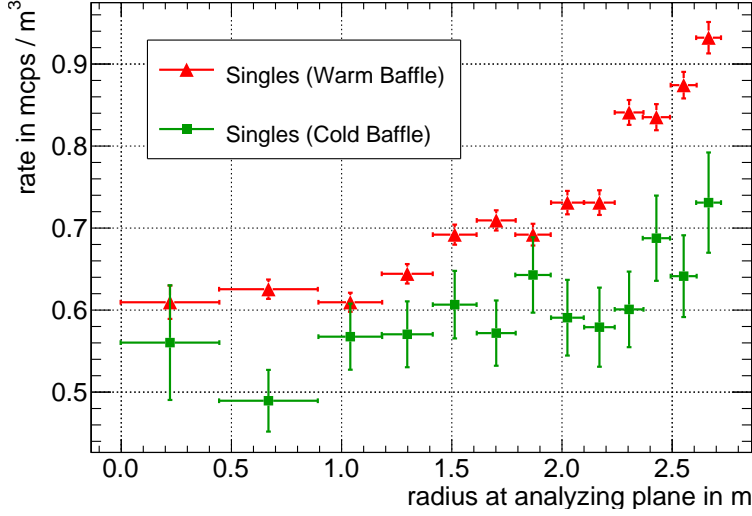
Figure 4.7.: Comparison of single background rates: The single rate during warm baffle measurements is obtained by the Δt-cut. The rate during cold baffle measurements is dominated by singles as radon is not expected to decay within the spectrometer. Hence, the Δt-cut can be validated by comparing both curves. The discrepancy is due to radon-induced single background.

(right)). Therefore, inner spikes show a generally higher multiplicity[9]. If both graphs of figure 4.6 are taken into account, the radial background rate of figure 4.8 is retrieved.

The event distribution inside a radon-spike determines how sharp such structures are and how they are distributed. Figure 4.9 illustrates the radial spread of the events inside a spike relatively to the mean spike radius in numbers of detector rings, so the fuzziness of the ring structures. Most events (70 %) are distributed around the mean radius within one ring. A very low fraction (3 %) stretch over more than four rings.

A characteristic time structure of spikes has not been observed in the context of this thesis. Firstly, the statistics for high energy stored particles is rather low, and secondly, the increased pressure shortens the events to very low times, thereby eventually compressing effects to an unobservable level. A time structure is observed within KASSIOPEIA simulations at standard pressure in [Wan13].

4.4. Radon Activity

Assuming that each spike appears due to exactly one radon-decay, the radon-activity inside the main spectrometer can be estimated. Therefore, the spikes

---

[9]A result of the storage condition as the multiplicity correlates with the energy of the primary particle.
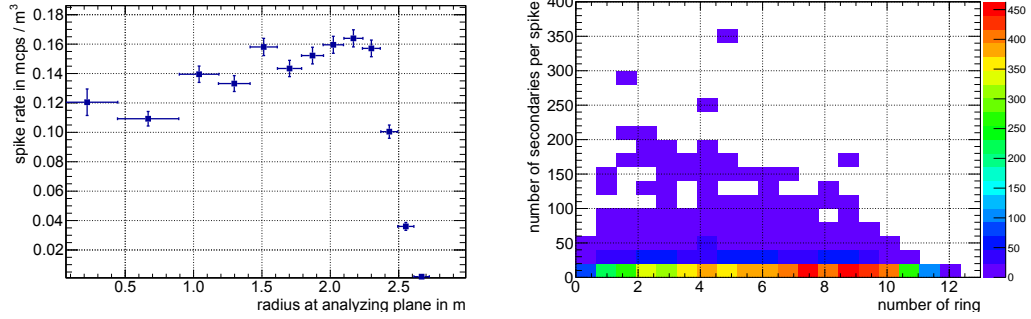
Figure 4.8.: Radial distribution of spikes at 9 G-setting. (left) Equivalently to the radial rate distribution of figure 4.6 here the radial spike rate normalized to the volume is shown. This distribution also decreases towards larger radii, but not until ring #8. This can be explained with the scatter-plot of number of secondaries per spike as a function of its ring radius (right). At large radii it shows a large number of spikes but with low multiplicities. The smaller the radius, the more spikes with high multiplicities occur, which explains the difference in distributions of the radial spike rate and the radial background rate.
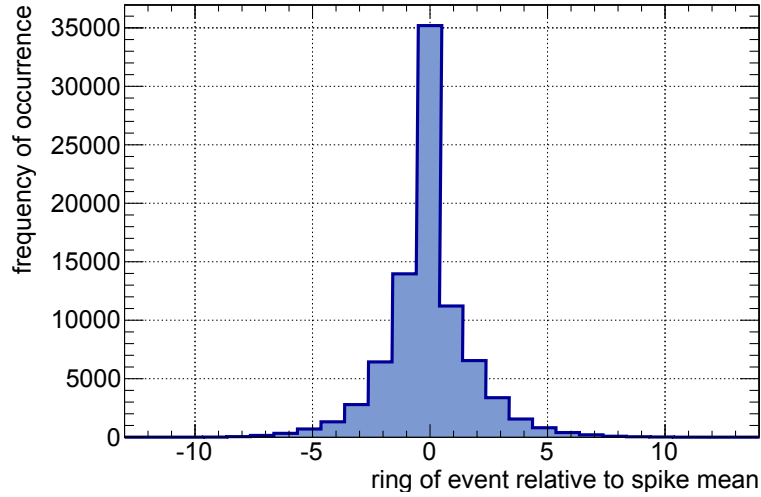
Figure 4.9.: Fuzziness of spike-rings at 9 G-setting during high pressure measurements. The relative distance to the mean radius of the spike is calculated and inserted into the histogram. About 70 % of the events are distributed around the mean radius and in the neighboring rings. Only a fraction of 3 % extend over more than 4 rings.
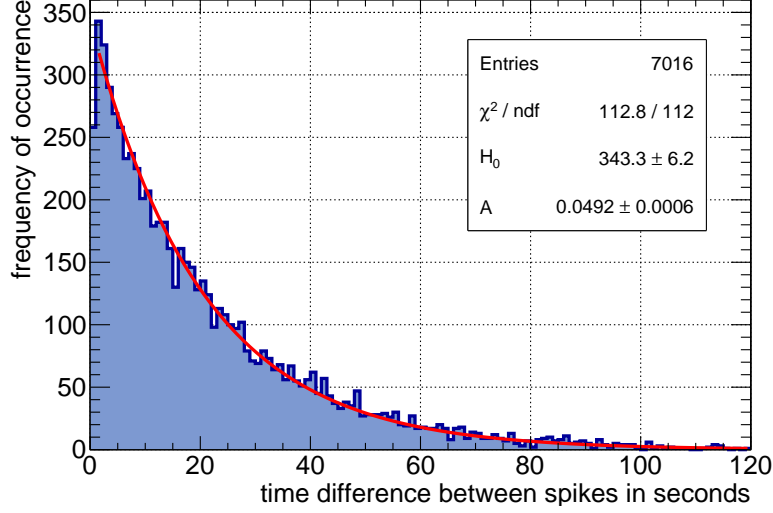
Figure 4.10.: Observed activity for 9 G-setting. The drop at the first bin is due to the interarrival-time cut as introduced in section 4.1, where detector hits time differences lower than 0.2 s are assigned to one spike.
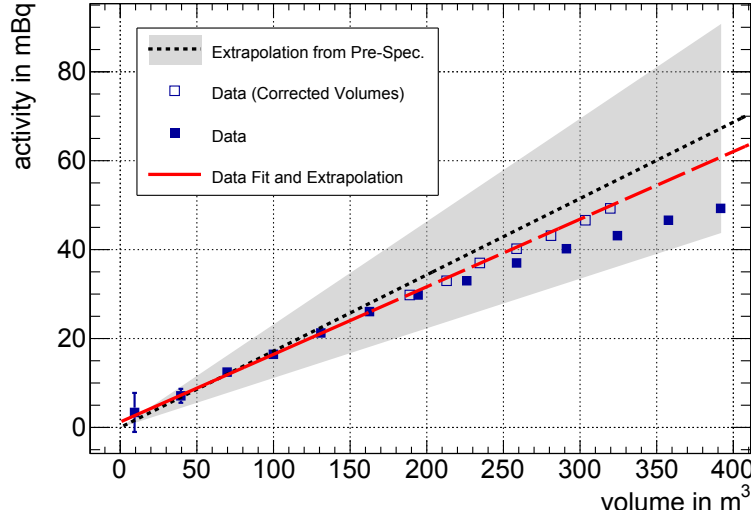
Figure 4.11.: Activity extrapolated to the entire main spectrometer volume. Every point is obtained by successively considering more pixel-rings of the FPD starting at the inner four pixels. The fit is applied only to the first six data points (solid line) and extrapolated (dashed line). The kink occurs due to unused pixels, which are corrected at the empty squares. An extrapolation from the pre-spectrometer [MDF+13] is drawn as dotted lines with its error-band.

are called radon-spikes in the following. As the radioactive decay is Poisson distributed, the time between two radon-decays follows an exponential distribution:

$$H(\Delta t) = H_0 \cdot e^{-A\Delta t}, \tag{4.1}$$

where A denotes the activity, Δt the time between two decays and H_0 is the initial decay rate in units of Bq. H_0 can be derived by the assumption that radon-decay continues during the total exposure time ΔT,

$$N_{\mathrm{D}} = A \cdot \Delta T. \tag{4.2}$$

Consequently, H_0 is given by equation (4.2) and the integral of (4.1) as

$$H_0 = A^2 \cdot \Delta T. \tag{4.3}$$

Therefore, the activity and the exposure time can be estimated by applying an exponential fit to the observed activity as shown in figure 4.10. There the times between radon-spikes for the 9 G-setting are shown. The activity is determined to $A = (49.2 \pm 0.6)\,\mathrm{mBq}$ and the initial decay rate to $H_0 = (343.3 \pm 6.2)\,\mathrm{Bq}$, which leads to an exposure time of $(141\,882 \pm 4304)\,\mathrm{s}$. This time is very close to the real time of $149\,443\,\mathrm{s}$. The drop in the first bin is due to the interarrival-time cut, introduced in section 4.1. As events with time differences lower than $0.2\,\mathrm{s}$ are assigned to a spike, this bin is underestimated since the bin width is one second. It has to be noted that this activity is only the observed activity within the specified flux tube volume (see table 2.1). The performed cuts of section 4.1 do not represent the real activity inside the entire main spectrometer volume.

To estimate the activity inside the entire main spectrometer volume, an extrapolation has to be applied. This activity is determined by performing the same fits as applied to the data shown in figure 4.10 for different observed volumes. These volumes are obtained by considering only specific FPD-channels for the extrapolation, starting at the *bulls-eye* (center-channels $\#0 - \#3$) and successively adding further pixel-rings. Figure 4.11 shows results of such analysis for the 9 G-setting. The extrapolation results in a radon-activity in the entire main spectrometer volume[10] of $A_{\mathrm{MS}} = (189.8 \pm 12.8)\,\mathrm{mBq}$ by considering only the first six detector rings, caused by shadowed and in other ways affected pixels (see section 4.1) at the outer rings. The volume of the outer seven data points can be corrected by subtracting the volumes related to the unused pixels. These are also marked in figure 4.11. Note, that corrections due to the cuts are not applied yet.

This estimation can be compared to extrapolations of the radon-activity from studies at the pre-spectrometer performed in [MDF+13], also shown in figure 4.11 (dotted line) including its error estimation. The data fits the extrapolation very well, although no required corrections (see section 4.5.2) were applied. If the correction factors are applied, the error-band of the extrapolation does not have an intersection with the measured activity anymore. Consequently, it lies below the measured activity for the entire main spectrometer volume. Hence, the extrapola-

---

[10] The entire main spectrometer volume is $1240\,\mathrm{m}^3$.

tion of [MDF$^+$13] underestimates the activity.

4.5. Multiplicity of Radon-Spikes and Correction Factors

The multiplicity $N_D(N)$ of radon-spikes, which is the number of detector hits within one spike, and its distribution is important to estimate the total radon activity, because an extrapolation to the multiplicity *one* has to be performed. As the maximal magnetic field on the detector side (5 T) is larger than at the pre-spectrometer side (4.5 T), only a fraction of 47:53 of the secondaries escape towards the detector. Therefore, the real amount of secondaries is higher and can be estimated by applying a factor of ≈ 2.1. Radon-spikes with lower multiplicities corresponds to low-energy stored particles, whereas high multiplicities originate from high energy stored particles. This is reasonable as high-energy particles ionize more than particles with low energy. As shown in figure 3.3, radon-decays generate much more low-energy particles than high-energy electrons. Consequently, the distribution of the secondaries should show a considerable fraction of low multiplicities.

4.5.1. Multiplicity of Radon-Spikes

For the 9 G-setting, the multiplicity is shown in figure 4.12. As the minimum of the multiplicity is limited by the cuts introduced in 4.1, the data starts at $N = 3$ with $\sim 10^3$ entries, decreases rapidly and reaches approximately zero at several hundred secondaries per decay. This distribution follows in first order approximation a power-law

$$N_D(N) = N_D^0 \cdot N^{-\gamma}, \tag{4.4}$$

where γ denotes the slope. By applying a fit in the range from 3 to 100 to the distribution as shown in figure 4.12, the slope is determined to $\gamma = 1.945 \pm 0.014$ with $\chi^2/\text{ndf} = 228.2/91$. However, the χ^2/ndf value gives a hint, that this distribution actually is not a power-law. In the following, three other reasons are given, why it probably follows another distribution.

Power-law fits in different multiplicity regions are a possibility to test if the multiplicity follows a power-law. For this purpose, the lower limit of the considered multiplicity bins is successively increased from $N_{\min} = 3$ up to $N_{\min} = 50$. Consequently, the fits were applied from $N_{\min}$ to $N_{\max} = 100$ and the determined slope γ is plotted as a function of $N_{\min}$ in figure 4.13. A large change of γ is observed for $N_{\min} < 20$. It is reasonable that a power-law is not a good description for this distribution in this region. However, it looks differently for higher limits $N_{\min} \gtrsim 25$. γ is not changing within its error bars, so that the power-law may be a good description for the multiplicity in this region. Thus for lower multiplicities another analytic description has to be found.
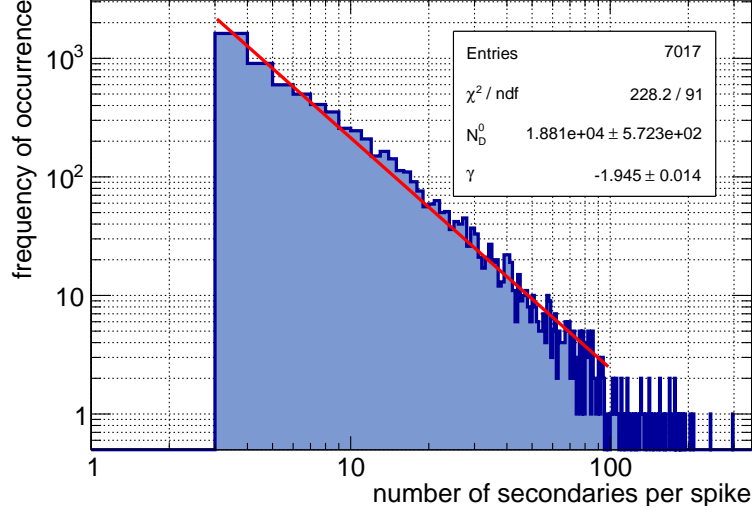
Figure 4.12.: Multiplicity of radon-spikes at 9 G-setting. As discussed in section 4.1, only spikes with multiplicities $N > 2$ are considered. In first order approximation, this distribution follows a power-law. Thus, one spike can consist of several hundred secondaries.
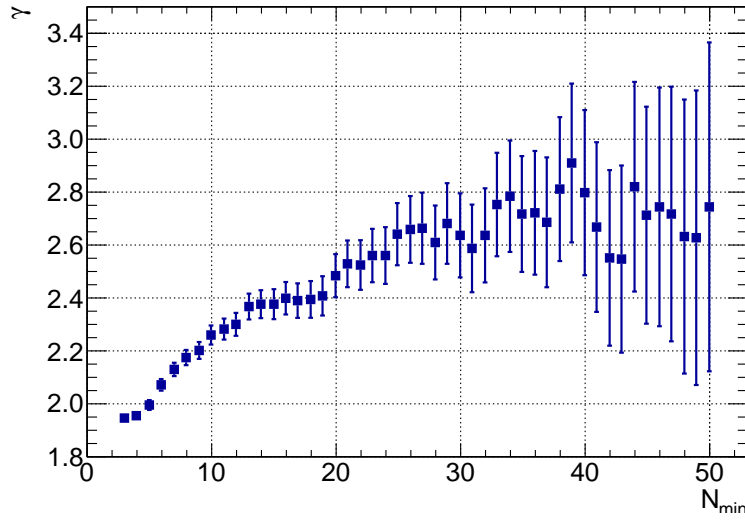

Figure 4.13.: Applying power-law fits to the multiplicity by increasing successively N_{min} at 9 G-setting. As the slope γ is changing in particular for low N_{min}, it is reasonable that the multiplicity is not power-law distributed. For higher $N_{\mathrm{min}} \gtrsim 25$, the multiplicity may follow a power-law.
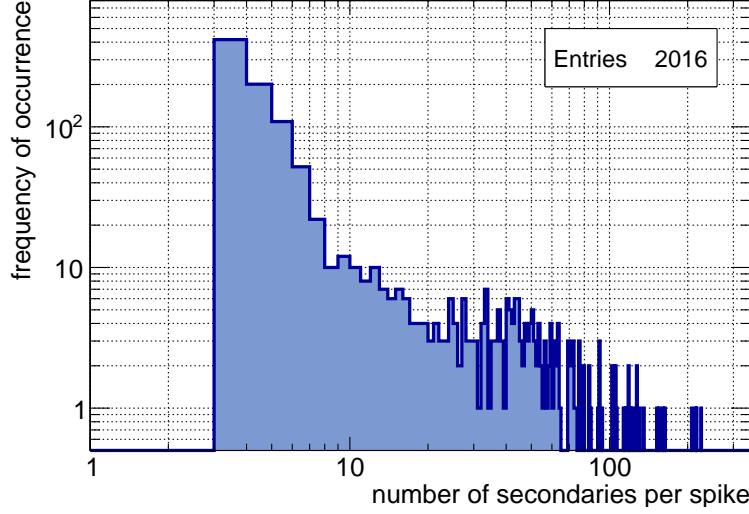
Figure 4.14.: Kassiopeia simulation of hydrogen to investigate the behavior at
low multiplicities at 9 G-setting, where the simulation does not fol-
low a power-law. Low multiplicities caused by shell-reorganization
electrons, high multiplicities due to conversion electrons.

Simulations of hydrogen[11] by using Kassiopeia gives another evidence. Indeed
the simulation data do not fit the distribution shown in figure 4.12, as for
lower multiplicities they do not follow a single power-law. Figure 4.14 il-
lustrates such a simulation after applying the same analysis cuts as for the
data. The change in slope at $N \sim 8$ maybe due to a missing component in
the medium energy region. Low multiplicities arises from shell-reorganization
electrons, while high multiplicities correspond to shake-off and inner conver-
sion electrons. In order to obtain low multiplicities, which are comparable
to the measurements, the shell reorganization part of the radon generator
[Wan13] of Kassiopeia had to be modified. While previously, the shell re-
organization electrons shared a total energy of 230 eV, simulations using a
value of 50 eV showed better agreement[12].

First-bin estimation by utilizing baffle-measurements. The value of the first bin
of the multiplicity-plot can be estimated by using measurements with cold
baffle during SDS-1 at 9 G-setting and 10^{-10} mbar. By the assumption that
during cold baffle measurements no radon-induced background occurs (100 %
efficiency of the baffle), the detector-rate is caused due to singles only. The
fact that these measurements are performed at 10^{-10} mbar can be neglected,
since the single background varies very poorly with pressure. Using the single
rate resulting from the analysis of this work (see section 4.1), it is possible
to estimate the radon-induced singles, since the singles determined with the

[11]Performed by N. Wandkowsky.
[12]Total energies between 25 and 230 eV were scanned in 5 eV steps.
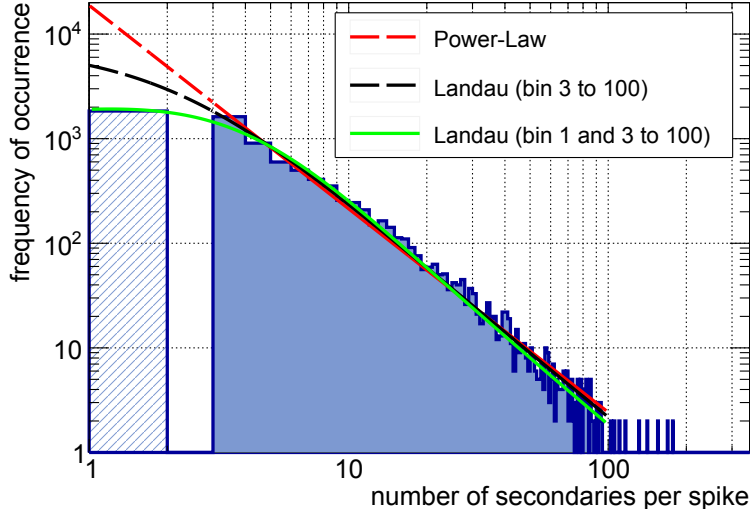
Figure 4.15.: Multiplicity of radon-spikes with estimated multiplicity 1 at 9 G-setting. The estimation (hachured bin) is a result of a combination of cold-baffle measurements and warm-baffle at high-pressure measurements. This estimation shows, that the multiplicity distribution does not follow a power-law. For comparison, two Landau-Fits are applied which seem to better describe the distribution.

$\Delta t > 0.2\,\mathrm{s}$ condition also contain singles due to radon. For this purpose, the difference of the cold-baffle single-rate and the single-rate during warm-baffle high-pressure exposure time has to be calculated. By using $r_{\text{cold-baffle}} = (219.7 \pm 4.7)\,\mathrm{mcps}$ [BBB^{+}14] and $r_{\text{warm-baffle}}^{\text{singles}} = (232.0 \pm 1.2)\,\mathrm{mcps}$ the radon-induced single rate is estimated to

$$
\begin{aligned}
r_{\text{Rn-induced}} &= r_{\text{warm-baffle}}^{\text{singles}} - r_{\text{cold-baffle}} \\
&= (12.3 \pm 4.9)\,\mathrm{mcps}.
\end{aligned}
\tag{4.5}
$$

By multiplying with the exposure time corresponding to the data used, the first bin is determined to $N_{\text{D}}(1) = 1838 \pm 725$. This estimation is also considered in the data shown in figure 4.15, which extends the data shown in figure 4.12. This visualizes the non-power-law behavior at low-multiplicities very well. The included fits will be discussed below.

Since the power-law fit does not describe the multiplicities of radon-decays very well, another analytic function has to be found. As simulations do not fit the measured multiplicity-distribution very well, a function has to be chosen based on the investigations outlined above. For low multiplicities a much flatter function than a power-law is required, while at high multiplicities the power-law fits well. Therefore, Landau-fits are performed as shown in figure 4.15. By considering the estimated first bin, the flattest fit is obtained, followed by the Landau-fit without

Table 4.1.: The calculated correction factors and activities (based on $(49.2 \pm 0.6)\,\mathrm{mBq}$, see section 4.4) inside the 9 G-flux-tube volume and the entire main spectrometer volume are shown in this table. The real activity A_{MS} may lie between κ_{low} (lower-bound Landau-fit) and κ_{max} (power-law fit).

Fit-Function	κ_3^i	$A_{\text{flux-tube}}$ in mBq	A_{MS} in mBq
Lower-Bound Landau	1.51	74.3 ± 0.9	286.6 ± 19.3
Landau	1.89	93.0 ± 1.1	358.7 ± 24.2
Power-Law	2.85	140.3 ± 2.8	541.3 ± 37.4

the first bin. The steepest function is the power-law fit as mentioned above. These fits are necessary for calculating correction factors as discussed in the next section.

4.5.2. Correction Factors

Although the measurements can only be used to directly determine multiplicities $N \geq 3$, using the applied fits allows an extrapolation to single and double hit events. Several fits are applied to determine the radon activity inside the main spectrometer compatible with data. The lower limit is determined by the Landau-fit by considering the first-bin estimation, while the power-law fit gives the upper value (see figure 4.15). In order to extrapolate the total activity within the main spectrometer, the correction factor $\kappa_{N_{\mathrm{min}}} \equiv \kappa(N_{\mathrm{min}})$ is introduced[13], which has to be applied to the activity (as in section 4.4) of the observable flux tube volume. The correction factor $\kappa_{N_{\mathrm{min}}}$ in general is defined by

$$\kappa_{N_{\mathrm{min}}} = \frac{\int_1^\infty F(N)\mathrm{d}N}{\int_{N_{\mathrm{min}}}^\infty F(N)\mathrm{d}N}, \qquad (4.6)$$

where $F(N)$ denotes the distribution function. If $F(N)$ is defined by the power-law, the correction factor $\kappa_{N_{\mathrm{min}}}^{\mathrm{upper}}$ is obtained by

$$\kappa_{N_{\mathrm{min}}}^{\mathrm{upper}} = (N_{\mathrm{min}})^{\gamma-1}, \qquad (4.7)$$

where γ describes the slope, see equation (4.4). The real activity inside the observed volume is defined by

$$A^{\mathrm{real}} = A \cdot \kappa_{N_{\mathrm{min}}}, \qquad (4.8)$$

where A denotes the measured activity inside the observable flux tube volume. By using equation (4.7) and (4.6), the correction factors and the real activity within the sensitive volume A^{real} and finally within the entire main spectrometer volume $A_{\mathrm{MS}}^{\mathrm{real}}$, can be determined. The results are summarized in table 4.1. Consequently, the real activity lies between the lower limit (Landau-fit) of $(74.3 \pm 0.9)\,\mathrm{mBq}$ and the upper limit (power-law-fit) of $(140.3 \pm 2.8)\,\mathrm{mBq}$. For the entire main

---

[13] N_{min} denotes the threshold for commutate events to radon-spikes, see section 4.1

spectrometer volume the activity is determined to within (286.6 ± 19.3) mBq and (541.3 ± 37.4) mBq. The correction factors ranges from 1.51 to 2.85.

Further Correction Factors

In addition to the correction factor detailed above, further corrections can be applied:

Invisible decays have a large impact on the activity. There exist several possibilities of radon decays happening without any electrons being detected by the FPD:

- the decay does not induce a stored particle,

- all secondaries are emitted to the source section,

- the electron escapes the sensitive volume before the first ionization occurs.

For investigation of such decays, KASSIOPEIA-simulations are required. If the total number $N_\mathrm{D}(0)$ of invisible decays is known, the correction factor is calculated easily:

$$\kappa_\mathrm{invisible} = \frac{\overline{N_\mathrm{D}(1)} + N_\mathrm{D}(0)}{\overline{N_\mathrm{D}(1)}}, \tag{4.9}$$

where $\overline{N_\mathrm{D}(1)}$ denotes the multiplicities summed from $N_\mathrm{min} = 1$ to $N = \infty$ (compare equation (A.1)). First simulations suggest a correction factor on the order of $\kappa_\mathrm{invisible} \approx 2$ (see appendix A.2.2).

Single induced background has an impact on the detection rate of radon spikes. As the detection strategy (see section 4.1) requires a minimum of three detector hits with interarrival-times lower than 0.2 s, singles do have an impact in that way, that three singles can occur with time differences lower than the intearrival-time cut. Also one single event in combination with a two-event radon-spike within a time difference of less than 0.2 s, turns non-detectable events into a radon-spike. Generally, singles are able to shift the multiplicity distribution to higher multiplicities. This impact of the single-events is investigated in section 5.2.2 within an empirical radon background model. This study determines the correction factor κ_singles.

In summary, an overall correction factor can be defined:

$$\kappa(N_\mathrm{min}) = \prod_i \kappa_i = \kappa_{N_\mathrm{min}} \cdot \kappa_\mathrm{invsible} \cdot \kappa_\mathrm{singles} \tag{4.10}$$

4.6. Storage Time and Background Estimation at 10^{-10} mbar **and** 10^{-11} mbar

The storage time of the primary electron can be determined using the timestamps of the secondary electrons arriving at the detector. The results of the analysis based
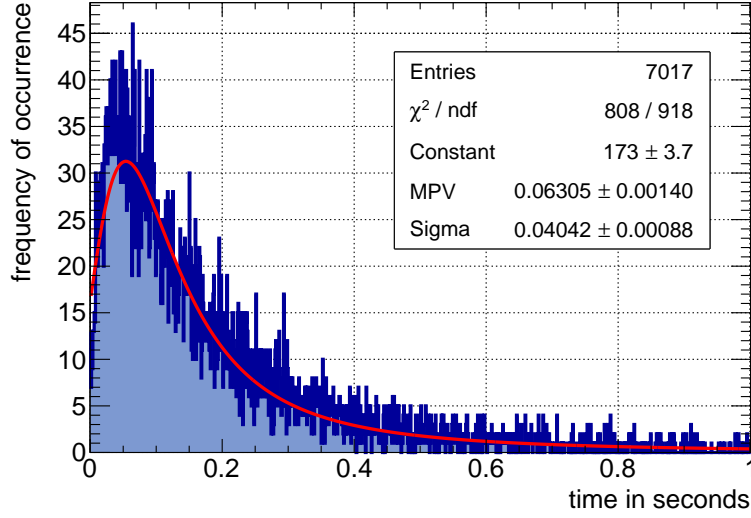
Figure 4.16.: Storage time of trapped electrons at the 9 G-setting. The measured distribution follows in good agreement a Landau-distribution. The most probable value for the storage time is determined to (63.05 ± 1.40) ms.

on SDS-1 measurements will be shown in section 4.6.1. Estimations of the expected background rate for 10^{-10} mbar (during SDS-1) and 10^{-11} mbar (design value) are performed in section 4.6.2. The number of simultaneously stored electrons is also discussed.

4.6.1. Storage Time

The storage time of the trapped electron can be determined by using the first and the last event of a spike. The time difference between the timestamps of both events is utilized as storage time. Generally, the storage time is longer than the difference between the first and last ionization, since at energies of $\lesssim 15$ eV no ionizations can occur energetically. However, this is negligible as the other processes (for example elastic scattering) for losing energy do not induce background.

Obviously, the higher the energy of the stored electron the longer the storage time. However, the high energy stored electrons can leave the magnetic bottle earlier due to non-adiabatic effects (such effect is mentioned within pressure dependence in section 3.2). The impact of non-adiabatic effects and especially the storage time is correlated to the pressure and the cross-sections of the scattering target (section 3.3). The higher the pressure the faster the stored electron will cool down and will fall below the storage condition threshold.

For measurements at the 9 G-setting, the storage time distribution is shown in figure 4.16. At storage times above 0.2 s, the measured distribution approximately follows a power-law. At shorter storage times it is much more flat. Therefore, a Landau-distribution is fitted in a range from zero up to five seconds. The fit

gives the most probable value of (63.05 ± 1.40) ms. The average storage time is determined to (212.5 ± 3.5) ms. The short storage times are mainly caused by shell reorganization electrons, whereas high-energy electrons originate from the shake-off and conversion processes (compare figure 3.3) and are stored much longer.

If the mean storage time and the activity are known, the probability for two spikes to overlap can roughly be estimated with a Poisson-distribution. The probability for two decays happening within the mean storage time at the chosen activity (the measured or the corrected), is calculated to lie between 10^{-4} and 10^{-5}. Consequently, this effect is negligible in first order approximation, which is sufficient for this analysis.

This storage time distribution can be compared to KASSIOPEIA simulations and theoretical considerations discussed in [Wan13]. The simulations are performed for ^{219}Rn at a pressure of 10^{-11} mbar. Hence, the storage times are different than the measured ones. To be able to compare them, the measured storage time is scaled by a factor ζ, as described in section 4.6.2. The spectra are compared in figure 4.18 (left). A rather good agreement is observed although the stretched data contains more particles with longer storage times, corresponding to higher primary energies.

4.6.2. Background Estimation at 10^{-10} mbar and 10^{-11} mbar

One method to estimate the radon-induced background at 10^{-10} mbar during SDS-1 and 10^{-11} mbar for normal pressure, is the so-called *spike-stretching*-method. This means that the radon-background measured at 10^{-8} mbar is extrapolated to 10^{-10} mbar (10^{-11} mbar) by modifying the storage time only. This is a result of the following assumptions and considerations:

- The activity of radon is identical, as it is independent of pressure or the species of the residual gas.

- The change of the pressure results in a higher interaction probability (see section 3.2).

- Molecular hydrogen as the new main scattering target leads to different energy-losses and cross-sections, see section 3.3.

- Non-adiabatic effects, as described in section 3.2, have to be taken into account, which have an impact on the total number of secondaries. This consequently leads to a change of the average background rate[14].

The modification of the storage time is performed by applying a stretching-factor ζ. In particular, each found spike will be stretched in that way, that the hit time of the first event of the spike (defined as the decay-time) will be kept while the hit times of all other events are delayed by the factor ζ with respect to the decay-time.

---

[14]The average background rate for the entire exposure time does not change by stretching of spikes, as the total number of events is not affected.

4. Analysis of Background Measurements at Elevated Pressure

ζ is composed of two factors:

$$\zeta \approx \zeta_{\text{pressure}} \cdot \zeta_\sigma, \tag{4.11}$$

where ζ_{pressure} denotes the change of pressure and ζ_σ the change to another gas species. To reduce the total number of secondaries due to non-adiabatic effects, an additional reduction factor is calculated (see section 3.2), which allows to decide if an event is kept. In the case of a factor two, 50 % of the events are randomly removed.

An interesting quantity for normal pressure is the amount of simultaneously stored electrons. As mentioned above, at high-pressure only one particle is stored at a time, since overlapping storage times are negligible. However, this fact changes considerable when improving the vacuum, since the storage time increases proportionally. In this section, this quantity also is investigated under the limitations of the chosen cuts from section 4.1. That means, that only radon-spikes with $N_{\min} = 3$ or more detector hits are considered. If the extrapolated storage time is actually longer than the considered time window, the overflowing events will be fed in at the beginning of the time window, thereby emulating a continuous measurement.

In the following, two methods for calculating ζ are discussed. This includes a method which uses the change of pressure and species of gas explicitly and a method which adjusts the storage time distribution to a simulated spectrum only.

Stretching Factors Derived from Pressures and Cross-Sections

The stretching factor can be estimated from the pressure change and the cross-section change due to a differing scattering target. As outlined in section 3.2, the storage time is correlated with the inverse pressure. Using equation (3.6), this leads to a stretching factor of

$$\begin{aligned}
\zeta_{\text{pressure}}(10^{-10}\,\text{mbar}) &= \frac{p}{p'} \tag{4.12} \\
&= \frac{10^{-8}\,\text{mbar}}{10^{-10}\,\text{mbar}} = 10^2
\end{aligned}$$

for an extrapolation to the pressure during SDS-1, i.e. the electron will scatter 100-times less frequently and consequently the cool down at a 100 times lower rate. Equivalently, the correction factor for the normal pressure scenario is $\zeta_{\text{pressure}}(10^{-11}\,\text{mbar}) = 10^3$.

In addition, the change of the main scattering target from argon to molecular hydrogen has to be considered. This results in a different cross-section σ and average energy-loss $\bar{E}_{\text{loss}}$ per interaction as described in section 3.3. Considering both effects, a further stretching factor is obtained:

$$\begin{aligned}
\zeta_\sigma(\text{Ar} \rightarrow \text{H}_2) &= \eta_{\bar{E}_{\text{loss}}} \cdot \eta_\sigma \tag{4.13} \\
&\approx 9
\end{aligned}$$

Finally the total stretching factor ζ is calculated to $\zeta(10^{-10}\,\text{mbar}) \approx 900$ (for normal-pressure the factor is found to be $\zeta(10^{-11}\,\text{mbar}) \approx 9000$).

After application of the stretching the expected radon-induced background for the 9 G-setting at 10^{-10} mbar and 10^{-11} mbar can be investigated by determining the detector rate and the number of simultaneously stored particles. The bin width is chosen to be half of the expected most probable value (MPV) of the storage time[15] ($t'_{\text{storage}} \approx \zeta \cdot t_{\text{storage}}$) to ensure that the electrons are stored significantly longer than the bin width. With the knowledge of the activity inside the sensitive flux tube volume (see section 4.4) and the mean storage time (see section 4.6.1), the expected number of simultaneously stored electrons within 30 s for 10^{-10} mbar (300 s for 10^{-11} mbar) is estimated[16] to 9 respectively 90. This agrees very well with the bin-width independent calculations as detailed in table 4.2.

For a complementary estimation, the experimental data of SDS-1 are used. These are extrapolated to lower pressures by stretching the storage times of the individual spikes by the factor ζ, keeping the start times fixed. An average detector rate for radon-induced background of (269.8 ± 0.9) mcps for 10^{-10} mbar (for normal-pressure (267.1 ± 0.9) mcps) is obtained, which is close to the expectation of (299.9 ± 5.7) mcps [BBB$^+$14] (compare equation (3.7)). An approach for explanation for the difference is that only radon-spikes with a minimum of three events are considered (see section 4.1). The missed detector rate due to this reason can be roughly approximated by using the extrapolations for the spike multiplicity from section 4.5.2. In combination with the rate reduction due to non-adiabatic effects, this leads to an additional detector rate of 20 mcps by using the lower-bound Landau-fit, and 55 mcps by using the power-law-fit as upper-bound, respectively. In this case, the expected rate (299.9 ± 5.7) mcps lies between the lower (290 mcps) and upper (325 mcps) estimation.

The number of simultaneously stored electrons (see figure 4.17) is determined to 9.0 ± 3.0 for 10^{-10} mbar (89.6 ± 9.5 for normal-pressure). The results are compatible with the estimations and are detailed in table 4.2.

Comparison to Simulations

Another method to obtain the stretching-factor ζ is the comparison to simulation, performed in [Wan13]. These simulations are accomplished with KASSIOPEIA for ^{219}Rn and a pressure of 10^{-11} mbar, i.e. normal-pressure, using a total of 9817 stored particles.

For estimating the factor ζ, the storage time spectra can be compared. A χ^2 fit was performed to find the stretching factor that yields the best agreement of data (see figure 4.16) and simulation. The found factor is $\zeta(10^{-11}\,\text{mbar}) = 3916$. The scaled and simulated spectra are shown in figure 4.18 (left). It is apparent,

---

[15]See MPV of figure 4.16 and consider ζ.

[16]Example for 10^{-10} mbar: The activity is determined to ≈ 50 mBq which results in 1.5 decays within 30 s. The average storage time is measured to $t'_{\text{storage}} \approx \zeta \cdot t_{\text{storage}} = 900 \cdot 0.2\,\text{s} = 180\,\text{s}$, i.e. the stored electron extends over 6 bins. Finally, $N_{\text{electrons}} \approx 6 \cdot 1.5 = 9$ electrons are simultaneously stored within 30 s. This calculation is nearly independent of the bin width Δt_{bin} for $\Delta t_{\text{bin}} \ll t_{\text{storage}}$, since $N_{\text{electrons}} \approx \Delta t_{\text{bin}} \cdot A \frac{t_{\text{storage}} \cdot \zeta}{\Delta t_{\text{bin}}} = A \cdot t_{\text{storage}} \cdot \zeta$.
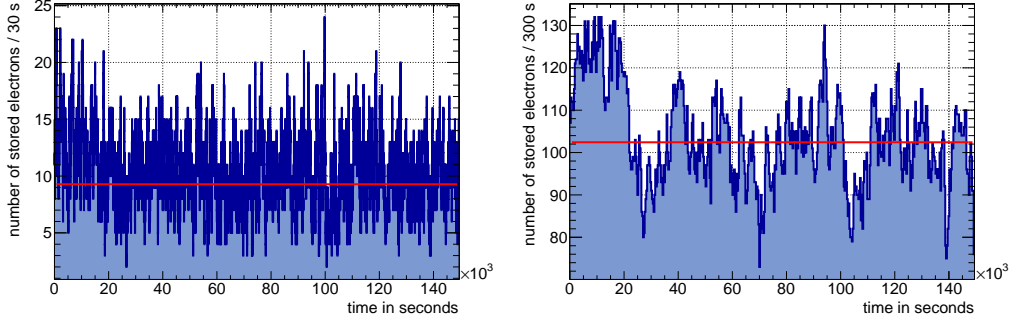
Figure 4.17.: Number of simultaneously stored electrons. (left) Extrapolation to 10^{-10} mbar (SDS-1) implies 9.3 ± 3.3 simultaneously stored electrons within 30 s. (right) Extrapolation to 10^{-11} mbar (normal pressure) with 102.4 ± 12.3 simultaneously stored electrons within 300 s.
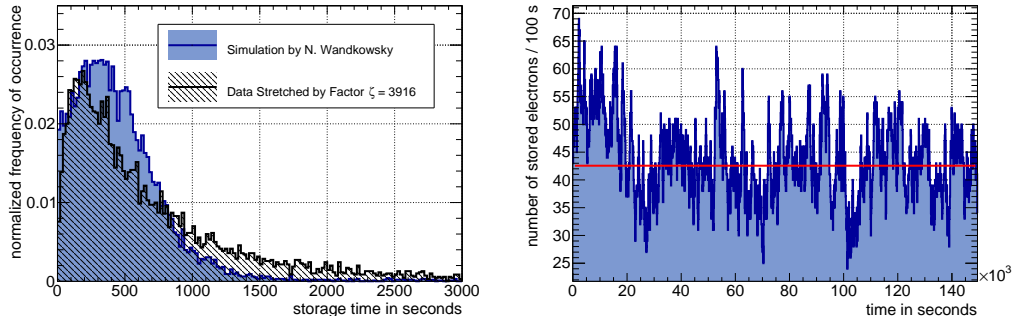

Figure 4.18.: Stretching-factor determined by comparing the storage time spectrum to simulations. (left) The storage time spectra of simulated and measured particles. Latter spectrum was scaled by a factor ζ, which was obtained by χ^2 minimization of the difference between the two spectra. The simulation was performed in [Wan13] for ^{219}Rn and a pressure of 10^{-11} mbar. (right) Number of simultaneously stored electrons for $\zeta = 3916$ at 10^{-11} mbar and 9 G-setting. The average number is determined to 42.6 ± 7.4 within 100 s.

Table 4.2.: Radon-induced background extrapolations from high-pressure 10^{-8} mbar to 10^{-10} mbar (SDS-1) and 10^{-11} mbar (normal-pressure). The table lists the results by stretching all radon-spikes by the factor ζ.

Pressure in mbar	ζ	Bin-Width in s	Mean Detector Rate in mcps	Simultaneously Stored Electrons within Bin-Width	Simultaneously Stored Electrons (bin-width independent)
10^{-10}	900	30	269.8 ± 0.9	9.3 ± 3.3	9.0 ± 3.0
10^{-11}	3916	100	267.1 ± 0.9	42.6 ± 7.4	39.0 ± 6.2
10^{-11}	9000	300	267.1 ± 0.9	102.4 ± 12.3	89.6 ± 9.5

that the simulation resulted in more low energy particles and shorter storage times respectively than the measured data.

In figure 4.18 (right) the number of simultaneously stored particles within 100 s during the entire exposure time is shown. It is determined to 42.6 ± 7.4 electrons per 100 s, with an unbinned value of 39.0 ± 6.2. Using the same rough estimation as described in footnote 16, about 38 simultaneously stored electrons are expected. The estimations are in good agreement with each other. The extrapolated average detector rate is determined to (267.1 ± 0.9) mcps. This is equal to the rate in the section above, as the secondary reducing factor is only determined by the pressure difference. These results are also listed in table 4.2.

This extrapolation to normal-pressure yield a 2.3 times smaller stretching-factor ζ than than the previous one. A discrepancy is, however, expected as simulation and measurement do not fit very well.

4.7. Conclusion

In this chapter, the analysis of the high-pressure measurements during the first SDS commissioning phase was discussed. It was shown that high-pressure measurements are suitable to investigate studying radon-induced background as individual radon decays are distinguishable, because the storage time is much lower than the average time between two decays. Therefore, it was possible to determine the activity of radon within the observable flux-tube-volume of the 9 G-setting to (49.2 ± 0.6) mBq, since the activity is not affected by any change of the pressure. This activity was also extrapolated to the entire main spectrometer volume, which led to an activity of (189.8 ± 12.8) mBq.

As the cuts applied within this analysis hide the real activity, correction factors were investigated. For that, the multiplicity distribution of radon-spikes was discussed. Since at low multiplicities the measured distribution is much flatter than a power law and at high multiplicities it may follow a power-law, two different Landau-distributions were fitted. As a consequence, a lower and an upper

limit were calculated. The lower limit is provided by an estimation of radon-induced singles. The power-law determines the upper limit. So, the real activity inside the flux-tube-volume was determined to be between (74.3 ± 0.9) mBq and (140.3 ± 2.8) mBq. The activity inside the entire main spectrometer volume was estimated to lie between (286.6 ± 19.3) mBq and (541.3 ± 37.4) mBq.

Also correction factors to take into account invisible decays and the impact of single events were discussed. An estimation for a correction factor for invisible decays was given by using KASSIOPEIA simulations with molecular hydrogen and a modified shell-reorganization energy. The factor is approximately $\kappa_{\mathrm{invisible}} \approx 2$.

The mean storage time of electrons was determined to (212.5 ± 3.5) ms. It was outlined that it potentially follows a Landau-distribution with its most probable value at (63.05 ± 1.40) ms. By modifying the storage time with a stretching factor while keeping the activity, a background estimation to normal pressure was performed. This includes a reduction of the radon-induced background rate due to non-adiabatic effects and the number of simultaneously stored electrons. The latter was computed by two different methods. First, the stretching factor was determined by considering the pressure change and the change of the gas species separately. Second, the stretching factor is obtained by fitting the storage time distribution to corresponding simulations. The number of simultaneously stored electrons was determined to 9.0 ± 3.0 for 10^{-10} mbar. Two methods are used to obtain the number of simultaneously stored electrons for normal pressure: 39.0 ± 6.2 (comparison to simulations) and 89.6 ± 9.5 (factors derived from pressures and cross-sections) respectively.

To investigate these parameters in more detail, dedicated Monte-Carlo simulations with KASSIOPEIA are required. A full understanding of the measurements at high-pressure and consequently the different behavior of the ionization of argon compared to molecular hydrogen can not entirely be reached within the analysis above. The real activity inside the main spectrometer is determined for a region only, which is a result of the ambiguous distribution of multiplicities of the radon spikes. Also the fraction of invisible decays has to be verified.

5. A Simple Empirical Radon Background Model Based on Measurements at $10^{-8}\,\mathrm{mbar}$

For calculating the radon background much faster than with KASSIOPEIA, a much simpler model was developed in context of this work. As basis it uses the results of the analysis of chapter 4, therefore it is an entirely empirical model. The so-called SIMBA[1]-model is a simple but powerful and easily extensible model, which simulates radon-induced events as well as single events for different magnetic field settings, pressures between $10^{-8}\,\mathrm{mbar}$ and $10^{-11}\,\mathrm{mbar}$ and different residual gas types. As in the previous chapter discussed, the highest uncertainty is the modeling of the multiplicity of radon-spikes. To involve this fact, it is possible to use different modelings of this distribution or to apply self-defined functions. Consequently, for different distributions studies were performed and compared to the results above.

In this chapter, this model and performed studies are introduced. In section 5.1, the model and the way how the background is simulated is described. After that, in section 5.2, different investigations are discussed and compared to data.

5.1. Simulation Strategy

The simulation of radon-induced background is based on simple distributions, resulting from chapter 4. For this, certain input parameter are required, listed in the following:

- The real activity inside the flux-tube-volume.

- The total exposure time.

- The magnetic field setting.

- The species of the residual gas.

- The pressure.

- The distribution of the multiplicity.

---

[1]**Sim**ple Empirical Radon **Ba**ckground

Figure 5.1.: The schematic simulation sequence of SIMBA. Each entry represents a sub-process which uses the knowledge of chapter 4.

These parameters are used to simulate the background events. The simulation sequence is a composition of five sub-processes, shown in figure 5.1. In the following, these processes are described and motivated.

Calculating All Radon Decays

The first step is to calculate the timestamps of all radon decays within the defined exposure time. As the time between two decays follows an exponential distribution as shown in equation (4.1), this calculation is done easily and very fast. This calculation is a direct consequence of the activity measurement in section 4.4 and figure 4.10.

Calculating the Multiplicity of each Decay

The second step dices the multiplicity of each decay. That means, how many secondaries per decay are reaching the detector. This is based on the previous investigated distributions, shown in figure 4.15. This is, as mentioned above, the section with the highest uncertainties, as the exact distribution is not known. Hence all three distributions (two Landau-distributions and one power-law) are predefined, which are used to simulate multiplicities down to one secondary per decay.

For higher multiplicities a limit is chosen, to avoid possible but very unlikely amounts of secondaries of about several million electrons or more. This limit is provided by a simple estimation for the maximum realistic number of secondaries.
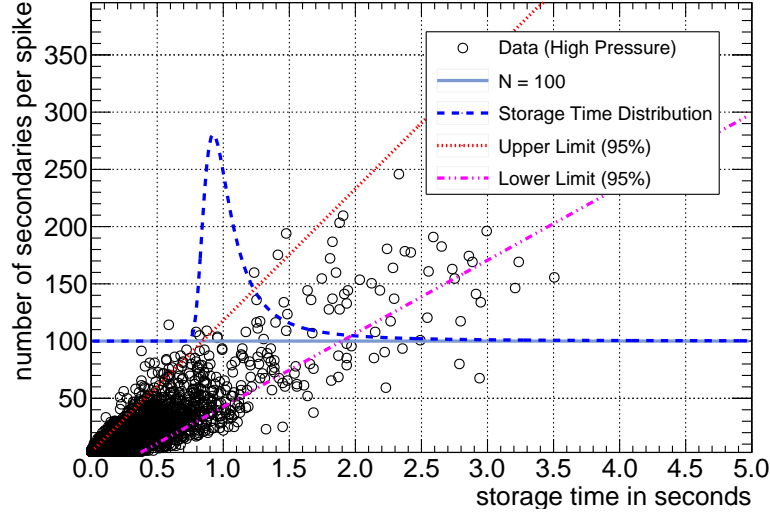
Figure 5.2.: Scatter plot of the number of secondaries per radon decay and the storage time of the primary electron. As for each multiplicity an individual Landau-distribution has to be calculated, the width of the data at the specified multiplicity has to be known. Therefore, an upper and a lower limit is determined by fitting two lines by the condition, that 95 % of the data points are included. An exemplary Landau-distribution for $N = 100$ is shown.

The maximum possible energy of a stored electron is estimated to be approximately 384 keV. By dividing it through the minimal ionization energy of the residual gas, the upper limit of secondaries is obtained. For example, for molecular hydrogen the maximal number of secondaries is estimated at approximately 25 000.

Correction of the Amount of Secondaries by Non-Adiabatic Effects

As described in section 3.2, non-adiabatic effects have an impact to the number of electrons reaching the detector. As it is pressure dependent, the input pressure parameter is compared to the pressure of the data, namely 10^{-8} mbar. The factor is calculated like in the section above and applied to the number of secondaries, computed in the previous step.

Calculating the Storage Time

At this point, have been computed the timestamps of the decays only. The timestamps of each secondary is not known yet. To approach that, first the storage time has to be known. Here, two distributions have to be considered: First, the Landau-like-distribution of the storage time as shown in figure 4.16. And second, the correlation between storage time and amount of secondaries. The latter is illustrated in figure 5.2. For dicing the storage time, for each number of secondaries

an individual Landau-distribution has to be calculated. Thus a most probably value (MPV) and the standard deviation σ has to be determined.

In general, both calculations require the width of possible storage times. For this purpose upper and lower limits are defined, as shown in figure 5.2. Both limits are calculated by including a total of $95\,\%$ of data points. By using these limits, the width for each number of secondaries is known. The MPV as well as the value of σ uses the width and each a different factor, which is fitted to the storage time in figure 4.16. An example is given in figure 5.2 for the multiplicity $N = 100$. The corresponding Landau-Distribution is included.

After dicing the storage time, it is reviewed by the condition shown in equation (5.1):

$$\text{diced storage time} < (\text{number of secondaries} - 1) \cdot 0.2\,\text{s}. \qquad (5.1)$$

This is reasonable as this model is based on high-pressure measurements. The analysis uses an interarrival-time cut of $0.2\,\text{s}$ (see section 4.1). Consequently, a radon-spike duration or the storage time respectively cannot be larger than the sum of all gaps between the secondaries. And these gaps are limited by the cut. Hence, if the condition of equation (5.1) is not fulfilled, the calculation is repeated.

After that, the storage time is scaled by the pressure. The factor is calculated as it is described in section 3.2. At this point, also the different cross-sections for hydrogen and argon should considered (see section 3.3). At the time of writing, this function is not fully implemented yet. Bit it will come available with the upcoming release of KASSIOPEIA3.

Determine the Timestamps of each Event

After the previous step it is possible to determine the timestamps of all events. The first event, thus the first secondary electron, appears at the time of decay[2]. The last event appears at the diced storage time plus the time of decay (if the multiplicity is greater than one). All other events (if the multiplicity is greater than two) are uniformly distributed between the first and last event.

5.2. Simulations

With this model, several studies are realized. The simulated data are analyzed with the same tools and cuts as in chapter 4, which is why the following results can be easily compared to the measured data. So, the real activity inside the flux-tube-volume is investigated (see section 5.2.1). This model also is suitable to analyze the impact of single events to the spike detection (section 5.2.2) as well as to determine correction factors for a measured activity (section 5.2.3). All studies are performed for the same exposure time as the data taking time in chapter 4, which is $149\,443\,\text{s}$ ($41.5\,\text{h}$).
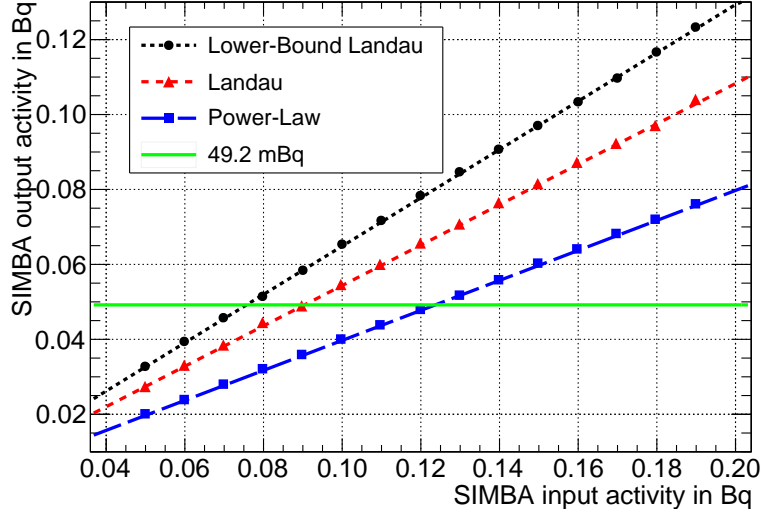
Figure 5.3.: Simulated radon background for different multiplicity distributions. For each data row, a linear fit is applied. By comparing the output and input activity, the real activity inside the flux-tube-volume of the 9 G-setting can be obtained. The measured activity of (49.2 ± 0.6) mBq is also included. As expected, the lower-bound Landau (see section 4.5.1) yields the lowest real activity and the power-law the highest. Errors are included, but to small to see.

5.2.1. Activity Studies

To determine the real activity inside the flux-tube-volume of the 9 G-setting, for all three multiplicity distributions, found in section 4.5.1, simulations are performed. By comparing the input and output activity, the real activity is obtained. The three multiplicity-distributions are obtained by the following considerations:

1. The lower-bound Landau-distribution consider the first bin estimation by using baffle-measurements and bin 3 to 100.

2. The Landau-distribution uses only the 3rd bin up to the 100th bin.

3. The Power-law distribution is provided by a power-law fit between bin 3 and 100.

For this study, 15 simulations for input activities between 50 mBq and 200 mBq for each multiplicity-distribution are performed. Single background is considered with (219.7 ± 4.7) mcps. The result is shown in figure 5.3. The lower-bound Landau-distribution for the multiplicity yields the lowest input activity for a kept output activity. The middle Landau and the highest input are obtained by the power-law. The measured activity inside the flux-tube-volume from section 4.4

---
[2]Compare with how the storage time is determined in section 4.6.1.

Table 5.1.: Comparison of simulated data with SIMBA and data from high-pressure measurements, analyzed in chapter 4. The input activity is about (75.7 ± 1.0) mBq and the lower-bound Landau-distribution for the multiplicity is used. SIMBA data fits very well the measured data. The slope (γ) results from a power-law fit to the multiplicity distribution.

Source	$A_{\text{flux-tube}}$ in mBq	Storage Time MPV in ms	Storage Time σ in ms	Slope (γ)
Data	49.2 ± 0.6	63.05 ± 1.40	40.42 ± 0.88	1.945 ± 0.014
SIMBA	50.5 ± 0.6	60.95 ± 1.56	40.09 ± 0.78	1.961 ± 0.013

of (49.2 ± 0.6) mBq is added to the figure (solid horizontal line). The intersections are (75.7 ± 1.0) mBq for the lower-bound Landau, (90.4 ± 1.2) mBq for the middle Landau and (123.7 ± 1.6) mBq for the power-law. Except for the power-law, the results are comparable with the values of section 4.5.2 and table 4.1.

This agrees with the expectation. The input activity should be comparable. The deviation from the power-law may result from the fact, that the power-law is not a good description of the multiplicity.

This result can be verified by comparing the multiplicity and storage time with the measured results of the high-pressure analysis of chapter 4. In figure 5.4 are exemplary the results for the determining of the activity, multiplicity and storage time shown (left) as well as a bin to bin comparison to the data from chapter 4 (right) for the lower-bound Landau modeling of the multiplicity. For this simulation, about 200 spikes found in addition as in the measured data. Therefore, the deviations on the right side of figure 5.4 should be above zero in average. By fitting the corresponding functions to the results, the activity, storage time and multiplicity are comparable to the high-pressure date, see table 5.1. The results fit the data very well as expected.

5.2.2. Single Events and its Impact to Spike Detection

As with this model the single background is completely removable, the impact of singles to the rate of spike detection is investigatable. For this, the algorithm for finding spikes is applied once to simulated data without singles and once to simulated data with simulated single events. Then the detected number of spikes with and without singles are compared:

$$\frac{\text{\# of spikes with singles}}{\text{\# of spikes without singles}} \tag{5.2}$$

This ratio is calculated for single rates between 100 mcps and 300 mcps with 20 steps in between. This is repeated 100 times. The result is shown in figure 5.5. The impact of singles to the spike detection is very small and is in a region of

Table 5.2.: The calculated correction factors and activities with SIMBA. The results for the Landau-distributed are very similar to the ones of table 4.1. Only the value for the power has a huge deviation. In this case, the determined activities of section 4.4 are used.

Fit-Function	κ_3^i	$A_{\text{flux-tube}}$ in mBq	A_{MS} in mBq
Lower-Bound Landau	1.58	77.6 ± 0.9	299.4 ± 20.2
Landau	1.89	93.0 ± 1.1	358.7 ± 24.2
Power-Law	2.59	127.3 ± 1.6	491.2 ± 33.1

several percent. In the case of the high-pressure measurements, the single rate is (219.7 ± 4.7) mcps, which leads to 2.3 % more detected spikes by using the linear fit. That means, that the activity is overestimated by a factor of 1.023.

5.2.3. Correction Factor

Correction factors as in section 4.5.2 can be easily obtained with SIMBA, since the real number of decays is known. These factors can be applied to a measured activity. For this purpose, 100 simulations are performed and the number of detected spikes and the real number of decays are compared. The result is shown in figure 5.6, where the ratio

$$\frac{\text{\# of detected spikes}}{\text{real \# of decays}} \tag{5.3}$$

is visualized. The correction factor $\kappa_3^{\text{lower-bound}}$ is defined by the inverse mean of the applied Gauss-fit:

$$\kappa_3^{\text{lower-bound}} = 1.58 \tag{5.4}$$

This value agrees within 5 % to the correction facto found in section 4.5.2. This result and the correction factors for the other two distributions for the multiplicity are outlined in table 5.2. The activities for the observable flux-tube-volume as well as for the main spectrometer volume were calculated (with the measured activity of section 4.4). The activities also have a rough agreement with the activities calculated in section 5.2.1.

5.3. Conclusion

In this section, the empirical SIMBA model is introduced. This model simulates the radon induced background based on simple assumptions. It is an immediate consequence of the analysis of the high-pressure measurements (chapter 4), which yielded the simulation parameters.

The highest uncertainty of this model also is the unknown distribution of the radon-spike multiplicity in the first two bins. Therefore, the studies are performed for three candidate distributions (chapter 4). By using different input activities

and by comparing the results with the measured activity, the real activity inside the flux-tube volume can be estimated. The results are comparable to the measured activities in chapter 4.

Also the impact of the single events to the number of detectable radon-spikes was investigated. As spikes must have more than two events with interarrival-times of lower than 0.2 s, singles can produce radon-spikes by appearing at the right time. It was found, that the number of spikes was overestimated by only about 2.3 %.

As in section 4.5.2, also with SIMBA correction factors can be obtained. For each multiplicity distribution 100 simulations are performed. The found factors are comparable to the previous ones of chapter 4.

The model works for high-pressure measurements, but further simulations and tests have to be performed to check the extrapolation to other pressures and magnetic field settings. For investigating the activity, approximately the same results as in chapter 4 are obtained. The SIMBA model can be used to generate radon-induced background with little computational effort in short time as opposed to particle tracking methods. This is for example required for neutrino mass sensitivity studies.
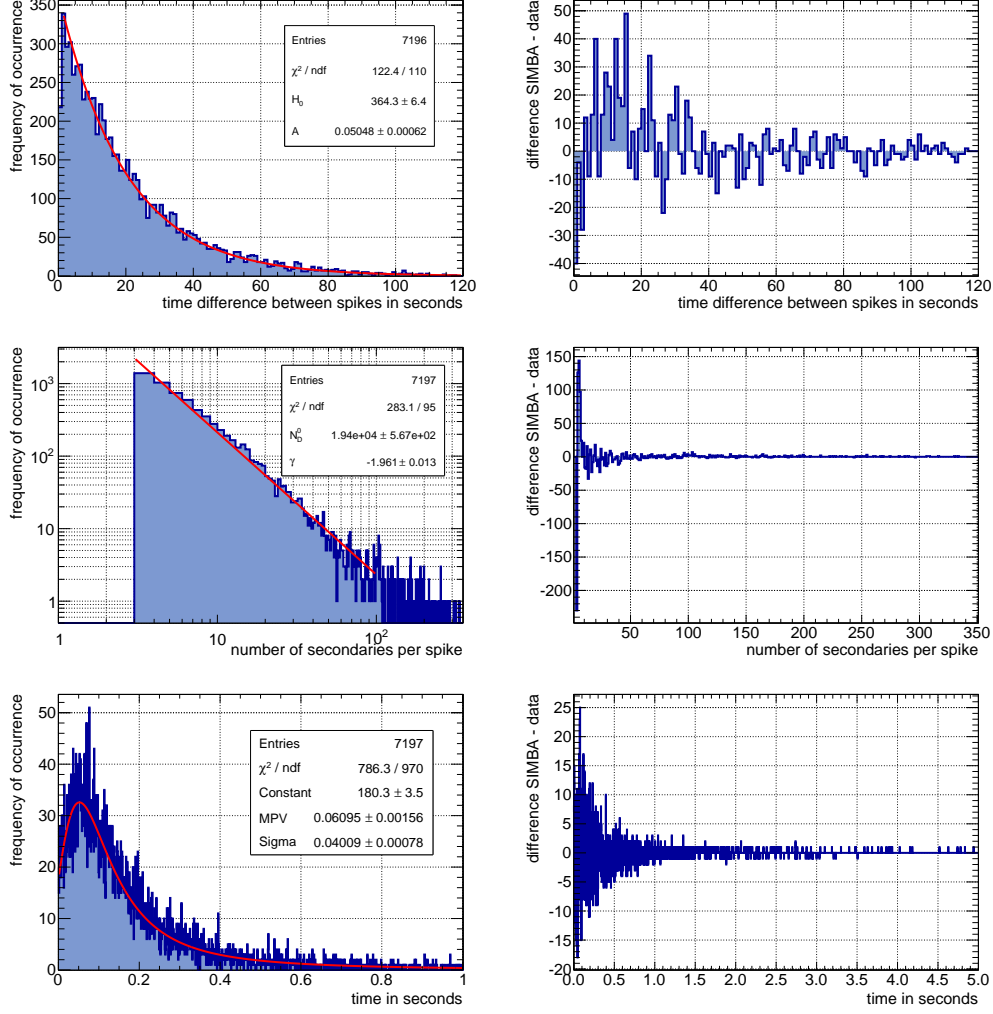
Figure 5.4.: Results of SIMBA and comparison to measured data for the lower-bound Landau modeling of the multiplicity. On the left side, the determination of the activity, the multiplicity and the storage time is shown. The fit parameters are in god agreement with the ones obtained in chapter 4. The right side shows a bin to bin comparison of SIMBA-data and measured data.
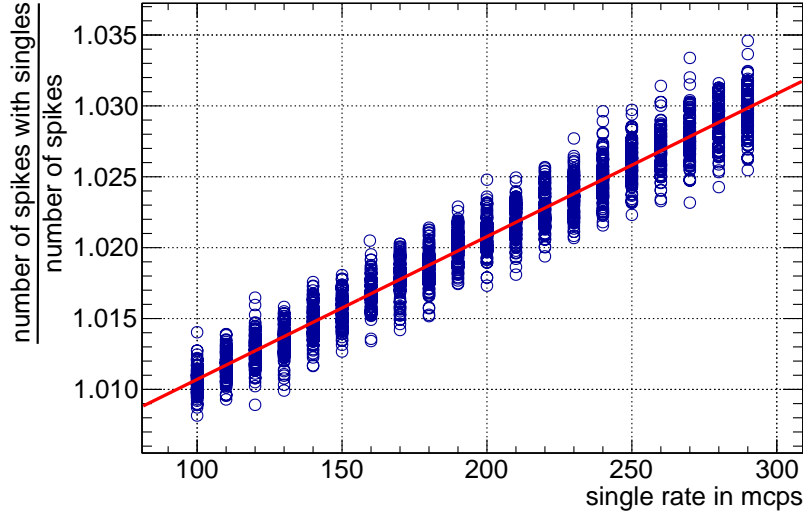
Figure 5.5.: Ratio between detected spikes by considering singles and without singles. Simulations are performed for different single rates with 20 steps in between and 100 repetitions. For the single rate at high-pressure measurements of (219.7 ± 4.7) mcps, the detected number of spikes is overestimated by a factor of 1.023.
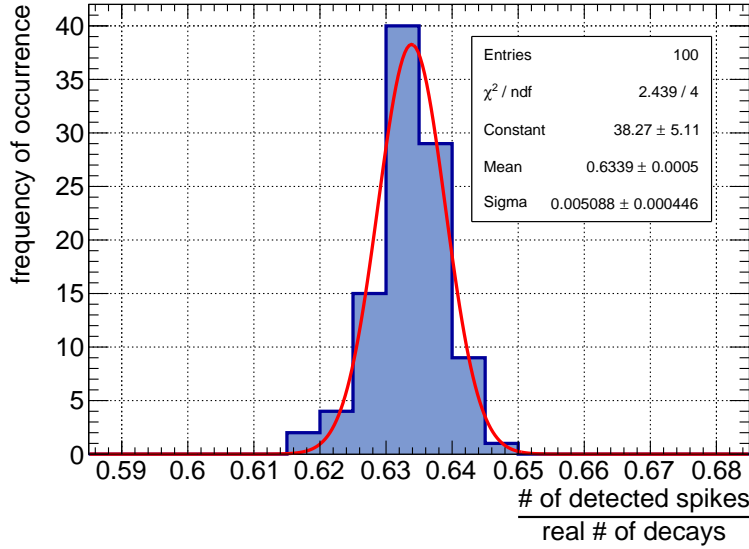
Figure 5.6.: Simulated radon background and ratio of number of detected spikes to real number of decays. 100 SIMBA-simulations are performed for the lower-bound Landau-distributed multiplicity. The obtained fraction of detected spikes (using the mean value of the Gauss-fit) is (63.39 ± 0.05) %.

6. Conclusion and Outlook

At the next-generation β-decay experiment KATRIN the effective electron-antineutrino mass will be measured with a sensitivity of $m_{\overline{\nu}_{\mathrm{e}}} = 200\,\mathrm{meV/c^2}$ at 90 % C.L. For this purpose, all experimental parameters have to be optimized. Major background sources are ^{219}Rn and ^{220}Rn. Therefore, the focus of this thesis is to study these background components by analyzing background measurements performed during the first commissioning phase (SDS-1).

The first step of the analysis is the separation of the background components: radon-induced background (so-called *radon-spikes* or *spikes*) and background originating from the vessel's wall (so-called *singles*) due to electrons kicked out by muons. By considering the interarrival-time between two signals, a condition is found. The assumption is that all events with interarrival-times lower than $0.2\,\mathrm{s}$ are due to radon and all other events are due to singles. However, a second condition is applied to find spikes: each radon-spike has to have a minimum amount of three electrons.

By using this separation method, the contributions of each background component to the total background rate $((857.7 \pm 2.4)\,\mathrm{mcps})$ were determined: the contribution of radon is $(569.8 \pm 2.0)\,\mathrm{mcps}$ and the one of singles is $(232.0 \pm 1.2)\,\mathrm{mcps}$. So, it is obvious, that radon induces the main fraction to the background. The radial distribution of both components shows the expected behavior. The radon-induced background is higher for decreasing radii. This is a consequence of the storage conditions. For the single background, the distribution is reversed due to shielding effects. The investigation of the events within a radon-spike revealed that the most events are distributed around the average radius and therefore, the fuzziness is very small.

Assuming that each spike corresponds to one radon-decay, the radon activity inside the observed flux-tube volume (for the 5 G- and 9 G-setting) was determined to $(49.2 \pm 0.6)\,\mathrm{mBq}$ and $(82.8 \pm 3.1)\,\mathrm{mBq}$ respectively. This activity was extrapolated to the main spectrometer volume. However, these only represent the observed activities, as the separation method neglects a fraction of radon-decays. To resolve this issue, the multiplicity of radon-spikes was studied to obtain a correction factor κ_3. Since this distribution is just known from the multiplicity of three, an extrapolation to one was performed. Nevertheless, it was only possible to determine an upper $(\kappa_3^{\mathrm{upper}}(9\,\mathrm{G}) = 2.85)$ and lower $(\kappa_3^{\mathrm{lower}}(9\,\mathrm{G}) = 1.51)$ limit. Consequently, the real activity inside the flux-tube volume lies between $(74.3 \pm 0.9)\,\mathrm{mBq}$ and $(140.3 \pm 2.8)\,\mathrm{mBq}$ for the 9 G-setting. In addition, two other correction factors are discussed, resulting from non-detectable decays and an overestimation of radon-

spikes due to singles.

The study of the storage time revealed a similar distribution as expected from simulations. The storage time was determined by using the time difference between the first and the last event of a radon-spike. The average value was determined to $(212.5 \pm 3.5)\,\text{ms}$ $(9\,\text{G})$, the most probable value to $(63.05 \pm 1.40)\,\text{ms}$ $(9\,\text{G})$. By the modification of the storage time, the background rate was extrapolated to $10^{-10}\,\text{mbar}$ and $10^{-11}\,\text{mbar}$. The rates were found to $(269.8 \pm 0.9)\,\text{mcps}$ and $(267.1 \pm 0.9)\,\text{mcps}$ respectively. For this purpose, several factors for scaling the storage time, so-called *stretching factors*, are found and compared. Also, the number of simultaneously stored electrons was estimated. This analysis yielded 9.3 ± 3.3 simultaneously stored electrons per $30\,\text{s}$ and 102.4 ± 12.3 electrons per $300\,\text{s}$ respectively.

Based on the analysis above, an entirely empirical background model called SIMBA was developed. It uses the distributions from above and can perform very fast simulations of radon background. This is, for instance, useful for neutrino mass sensitivity studies, as particle tracking has a long computation time. With the aid of this model, even the real activities inside the observed flux-tube volume were determined. As expected, these are comparable to the ones obtained in the analysis above. A benefit of this model, compared to the analysis above, is the a priori known number of radon-decays. Therefore, it was possible to investigate the impact of the single background to the number of detected radon-spikes. The single background leads to an overestimation of the radon-decays of $2.3\,\%$.

With the upcoming release of Kassiopeia3, it will be possible to perform particle tracking simulations with argon as main scattering target, leading to a better understanding of the different behavior of argon and hydrogen. This is of particular interest for a full understanding of the radon-spike multiplicity distribution as well as the amount of non-detectable decays. This will allow a more precise estimation of the real activity inside the main spectrometer volume.

A. Appendix

A.1. SDS-1 Measurement Settings

A brief overview of the SDS-1 runs are given in table A.1. For the 9 G-setting analysis only the runs #8547 - #8567 are chosen, as in the two previous runs, the pressure stability was not sufficient. The used air coil settings are listed in table A.2.

The pre-spectrometer solenoid settings are:

- PS1: 103.8 A.

- PS2: 149.7 A.

The detector and pinch magnet settings are:

- Detector: 54.59 A (3.5 T).

- Pinch: 72.63 A (5 T).

The high-voltage settings are:

- Vessel: $-18.5\,\mathrm{kV}$.

- Inner electrode: $-18.6\,\mathrm{kV}$.

- Steep cones with 100 V offset.

A.2. Correction Factors

A.2.1. Calculation of the Correction Factor

The correction factor of equation (4.6) is calculated by the following steps. Let $F(N)$ be the normalized distribution function of the multiplicity and N_0 the constant. By integrating the multiplicity distribution, the observable amount of decays is obtained by

$$\overline{N_{\mathrm{D}}(N_{\min})} = \int_{N_{\min}}^{\infty} N_0 \cdot F(N) \mathrm{d}N. \tag{A.1}$$

Equation (A.1) should be equal to

$$\overline{N_{\mathrm{D}}(N_{\min})} = A \cdot \Delta T, \tag{A.2}$$

Table A.1.: Overview over the SDS-1 measurements. Rates calculated in context of this thesis and obtained from [BBB$^+$14].

Magnetic Field in G	Baffle System	Pressure in mbar	Run Time in h	Average Rate in mcps	Run Numbers
3.8	warm	10^{-10}	30.7	781.9 ± 2.7	#6954, #6959, #6991, #7007, #8028, #8029
3.8	cold	10^{-10}	4.0	472.6 ± 5.7	#7070, #7072 - #7074
5.0	warm	10^{-10}	2.0	661.7 ± 9.6	#8289
5.0	warm	10^{-8}	4.2	1247.3 ± 9.0	#8531 - #8533
9.0	warm	10^{-10}	14.0	519.6 ± 3.2	#7340 - #7352, #8479
9.0	cold	10^{-10}	2.8	219.7 ± 4.7	#7093, #7094, #7096
9.0	warm	10^{-8}	42.3	858.1 ± 2.4	#8545 - #8567

Table A.2.: Overview over the air coil settings for measurements at 5 G- and 9 G-setting.

Air Coil Number	Current for 5 G-setting in A	Current for 9 G-setting in A
#1	60.1	95.2
#2	15.4	99.8
#3	24.3	48.9
#4	41.8	98.8
#5	47.4	100.0
#6	77.4	74.0
#7	29.7	98.2
#8	52.1	96.6
#9	58.0	80.9
#10	48.6	90.4
#11	54.8	61.3
#12	23.8	99.0
#13	46.0	97.6
#14	50.9	36.2
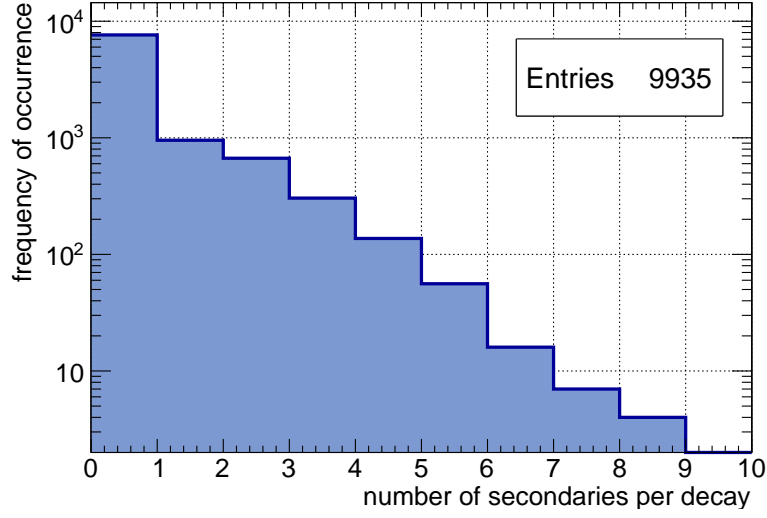
Figure A.1.: Kassiopeia simulation for *invisible decays* at 9 G-setting. This plot is a multiplicity plot without analysis cuts applied and a value to bin *zero* is appended. This represents the amount of decays which do not induce a signal at the detector.

where A denotes the observable activity and ΔT the exposure time. The real number of decays is given by

$$\overline{N_{\mathrm{D}}^{\mathrm{real}}} = A_{\mathrm{real}} \cdot \Delta T = \overline{N_{\mathrm{D}}(N_{\min} = 1)} = \int_1^\infty N_0 \cdot F(N)\mathrm{d}N. \qquad (\mathrm{A.3})$$

A_{real} describes the real activity inside the observed volume. Using these equations, the correlation between A_{real} and A and $\kappa(n_{\min})$ follows immediately:

$$
\begin{aligned}
A_{\mathrm{real}} &= \frac{\overline{N_{\mathrm{D}}^{\mathrm{real}}}}{\Delta T} & (\mathrm{A.4}) \\[2ex]
&= \frac{\overline{N_{\mathrm{D}}(N_{\min})}}{\Delta T} \cdot \frac{\overline{N_{\mathrm{D}}(1)}}{\overline{N_{\mathrm{D}}(N_{\min})}} & (\mathrm{A.5}) \\[2ex]
&= A \cdot \underbrace{\frac{\int_1^\infty F(N)\mathrm{d}N}{\int_{N_{\min}}^\infty F(N)\mathrm{d}N}}_{\kappa(N_{\min})} \cdot & (\mathrm{A.6})
\end{aligned}
$$

A.2.2. Correction Factor due to Invisible Decays

As introduced in section 4.5.2, the value of the correction factor for *invisible decays* is motivated by hydrogen simulations with Kassiopeia for the specified 9 G-setting, performed by N. Wandkowsky. The corresponding multiplicity plot is shown in figure A.1. This figure shows the multiplicity of radon de-

cays *before* any analysis is applied. The bin *zero* represents the number of decays which do not induce a signal on the detector. But in this case, this bin also contains all decays which have happened outside of the sensitive volume. Therefore it is overestimated and it has to be corrected by the ratio of volumes: $V_{9\mathrm{G}}/V_{\mathrm{MS}} = 391.781\,\mathrm{m}^3/1240\,\mathrm{m}^3$. After that, with equation (4.9), $\overline{N_{\mathrm{D}}(1)} = 2307$ and the corrected *zero* bin

$$N(0) = 7628 \cdot \frac{391.781\,\mathrm{m}^3}{1240\,\mathrm{m}^3} = 2410, \tag{A.7}$$

$\kappa_{\mathrm{invisible}}$ becomes to $\kappa_{\mathrm{invisible}} \approx 2$.

A.2.3. Fitted Function-Parameters to Multiplicity of Spikes

The parameters of the fitted functions to the multiplicity in figure 4.15 are listed below:

Lower-bound Landau distribution (lower limit) with parameters N_0 (constant), μ (MPV) and σ:

$$N_0 = 10\,628.100 \pm 294.747 \tag{A.8}$$
$$\mu = 1.481\,410 \pm 0.128\,197 \tag{A.9}$$
$$\sigma = 1.245\,350\,0 \pm 0.019\,666\,3 \tag{A.10}$$

Landau distribution (between lower and upper limit) with parameters N_0 (constant), μ (MPV) and σ:

$$N_0 = 51\,057.7 \pm 33\,434.1 \tag{A.11}$$
$$\mu = -0.395\,259 \pm 0.362\,738 \tag{A.12}$$
$$\sigma = 0.638\,947 \pm 0.190\,432 \tag{A.13}$$

Power-law distribution (upper limit) with parameters N_0 (constant) and γ (slope[1]):

$$N_0 = 18\,813.100 \pm 572.338 \tag{A.14}$$
$$\gamma = 1.944\,930\,0 \pm 0.013\,707\,6 \tag{A.15}$$

A.2.4. SIMBA: Fraction of Detected Spikes for Different Multiplicity Distributions

The obtained fractions, investigated in section 5.2.3, are listed below:

Lower-bound Landau distribution (lower-limit): Results of the gauss-fit.

$$\mu = 0.6339 \pm 0.0005 \tag{A.16}$$
$$\sigma = 0.005\,088 \pm 0.000\,446 \tag{A.17}$$

---

[1]Note that γ will be positive since in this work the power-law is defined as $N_{\mathrm{D}}(N) = N_{\mathrm{D}}^0 \cdot N^{-\gamma}$.
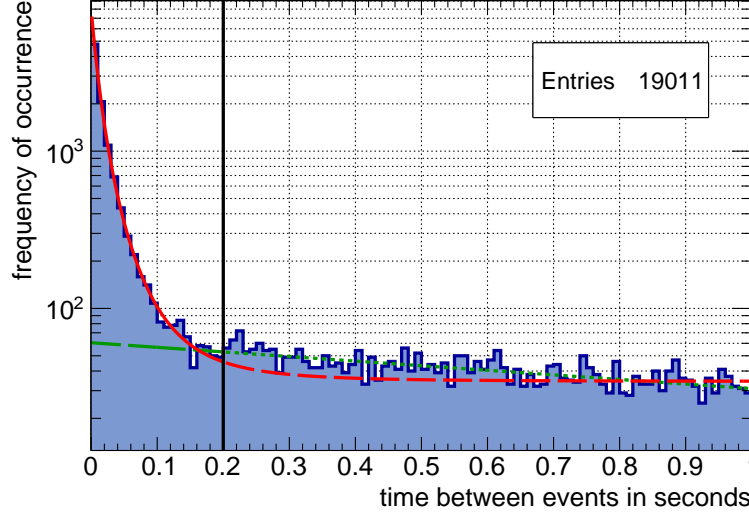
Figure A.2.: Time between two consecutive detector hits (interarrival-time Δt) during measurements at 10^{-8} mbar and 5 G-setting. An exponential and a flat background component were fitted to the data, intersecting at 0.2 s. The events with $\Delta t < 0.2$ s (solid line, *spikes*) originate mainly from stored particles, while events with $\Delta t > 0.2$ s (dotted line, *singles*) are generated by emissions from surfaces. Compare figure 4.3.

Landau distribution (between lower and upper limit): Results of the gauss-fit.

$$\mu \quad = \quad 0.53 \pm 0.00 \tag{A.18}$$
$$\sigma \quad = \quad 0.004\,747 \pm 0.000\,453 \tag{A.19}$$

Power-law distribution (upper limit): Results of the gauss-fit.

$$\mu \quad = \quad 0.3864 \pm 0.0004 \tag{A.20}$$
$$\gamma \quad = \quad 0.003\,631 \pm 0.000\,297 \tag{A.21}$$

A.3. Tables of Volumes and Activity Calculations

The used volumes and calculated and measured activities for figure 4.11 are listed in table A.3.

Table A.3.: Ring volumes for the 9 G-setting flux-tube. Also calculated and measured activities are included.

# of Ring	0	1	2	3	4	5	6	7	8	9	10	11	12
Ring Volume in m³	9.909	29.935	30.249	30.571	30.911	31.242	31.588	31.938	32.321	32.679	33.078	33.473	33.888
Volume from Ring #0 to # in m³	9.909	39.844	70.093	100.664	131.575	162.816	194.405	226.343	258.664	291.343	324.421	357.893	391.781
Volume from Ring #0 to # in m³ (corrected due to shadowed pixels etc.)	9.909	39.844	70.093	100.664	131.575	162.816	189.140	213.093	234.641	259.150	281.202	303.517	320.461
Expected Activity by [MDF+13] for Volumes from Ring #0 to # in mBq	1.701	6.839	12.032	17.279	22.585	27.948	33.370	38.852	44.400	50.009	55.687	61.433	67.250
Measured Activity for Volumes from Ring #0 to # in mBq (not corrected)	3.378	7.114	12.451	16.453	21.256	26.060	29.795	32.997	37.246	40.432	43.137	46.606	49.275

Figure A.3.: Detector rate during measurements at 10^{-8} mbar and 5 G-setting. Shown is a random 1000 s time window with a one-second binning. Increased rates over a short period of time (*spikes*) are caused by single high-energy stored electrons which cool down via ionization of residual gas molecules. Compare figure 4.4 (left).

A.4. Analysis of Background Measurements at Elevated Pressure and 5 G-Setting

In this section, the same analysis as in chapter 4 is briefly discussed for the 5 G-setting. The observed volume is larger than at the 9 G-setting (compare table 2.1). This leads to a larger number of detectable radon decays and hence to a larger measured activity. The statistics for the 5 G-setting is much lower than for the 9 G-setting, as its exposure time is just 4.2 h (compare table A.1).

In this section just the plots are shown and short descriptions are given. For further details, see chapter 4, as there the detailed explanations are given. For a better overview, in this section the same subsections are used as in chapter 4. So, the corresponding section at the 9 G-analysis should be easy to find.

A.4.1. Separation of Background Components

The analyzed runs are #8531 - #8533. The energy spectrum is shown in figure A.4. The shape is similar to the shape of the energy spectrum for the 9 G-setting (figure 4.1). The separation of the background components are performed in the same way (compare section 4.1). The corresponding interarrival-time spectrum is shown in figure A.2. The fits to the two different background components do not have an intersection at $\Delta t = 0.2$ s. However, this may be due to the low statistics, since the changed magnetic field do not have an impact on the time
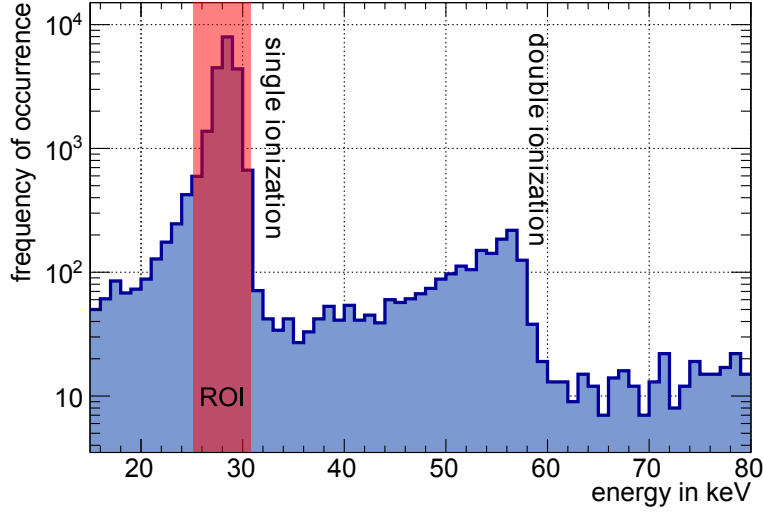
Figure A.4.: Energy spectrum of electrons detected at the FPD (5 G-setting). The *single ionization* peak, caused by single electron impact, is within the region of interest (ROI). The initially low-energetic electrons ($\mathcal{O}(\text{eV})$) are accelerated by the retarding potential $-18.6\,\text{kV}$ and the post acceleration electrode ($-10\,\text{keV}$). The *double ionization* peak is caused by the simultaneous (within $50\,\text{ns}$) impact of two electrons, presumably produced via double ionization of argon. Compare figure 4.1.

between ionizations[2] or single induced background. For the following analysis, also the time cut at $\Delta t = 0.2\,\text{s}$ is used to separate the background components.

The measured detector rate is shown in figure A.3. The very extensive rate increases are caused by stored electrons (emitted during a radon decay). The total background rate is determined to $(1247.3 \pm 9.0)\,\text{mcps}$. Out of that $(702.4 \pm 6.8)\,\text{mcps}$ are radon-induced and $(544.9 \pm 6.0)\,\text{mcps}$ are singles ($\Delta t > 0.2\,\text{s}$). Note, that this single rate is calculated by using a minimum of three events per spike. The real single rate is better estimated by using just two events per spike. This rate is measured to $(41.5 \pm 0.5)\,\text{mcps}$.

A.4.2. Radial Background Distribution

The radial background distribution is similar to the distribution during the measurements at the 9 G-setting (figure 4.6). The radial rate and the different background components are shown in figure A.5. A comparison of the single rate (shown in figure A.5) to cold baffle measurements is not possible for the 5 G-setting, since no cold baffle measurements are performed during SDS-1 for the 5 G-setting.

---

[2]To be more precise: The time between ionizations caused by a stored electron. Only pressure and residual gas species have a significant impact on this time difference.
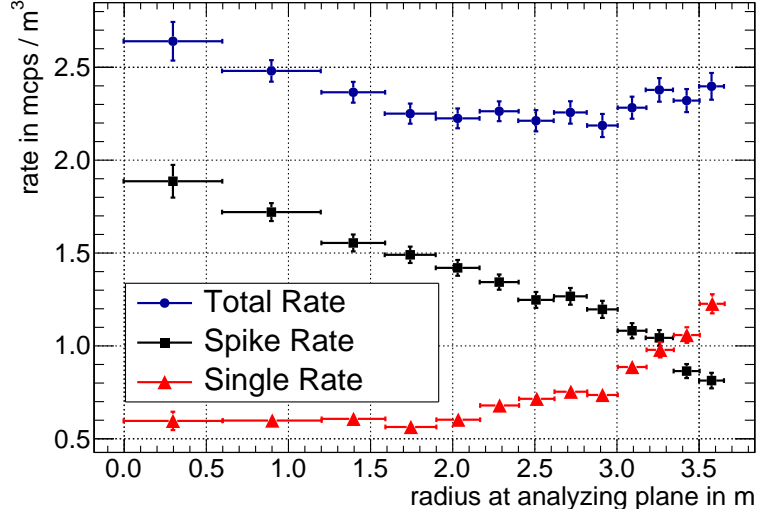
Figure A.5.: Radial background distribution at 5 G-setting: The total rate does not show a significant radial dependence. In contrast, events due to *spike* and events due to *singles* do have a contrary behavior at larger radii. Electron storage is most efficient in the center of the spectrometer, leading to spikes predominantly at smaller radii. Singles, however, originate from surface emissions and hence are expected to dominate at larger radii. Compare figure 4.6.

A.4.3. Spike Characteristics

The radial spike distribution during 5 G-setting measurements (figure A.6) is very similar to the distribution at 9 G-setting, shown in figure 4.8. The maximum at the radial spike distribution is reached at ring #7 respectively 2.5 m. Also the fuzziness is similar (see figure A.7 and compare to figure 4.9). Most events (70 %) are distributed around the mean radius within one ring. Just 4 % of the events are further away than four rings.

A.4.4. Radon Activity

To obtain the activity, equation (4.1) is used as well. The time between two decays is shown in figure A.8. The activity for the 5 G-setting is determined to (82.8 ± 3.1) mBq. This corresponds to $A_{5G}/V_{5G} = (0.126 \pm 0.005)$ mBq/m^3. The value for the 9 G-setting is determined to $A_{9G}/V_{9G} = (0.126 \pm 0.002)$ mBq/m^3. Thus, both measurements of the activity yielded equal results.

The constant H_0 (compare (4.1)) is measured to (91.3 ± 4.5) Bq. This leads to a measured exposure time of $(13\,317 \pm 520)$ s which is close to the real exposure time of $15\,242$ s.

Also an extrapolation to the entire main spectrometer volume is performed in the same way as for the 9 G-setting. The activity A_{MS}^{5G} is determined to
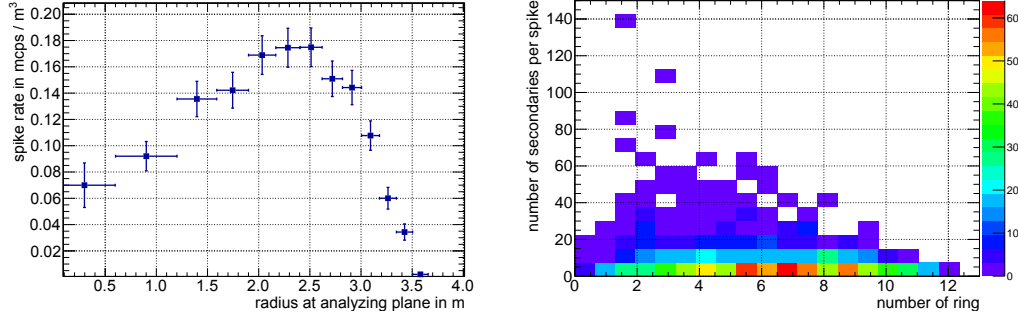
Figure A.6.: Radial distribution of spikes at 5 G-setting. (left) Equivalently to the radial rate distribution of figure 4.6 here the radial spike rate normalized to the volume is shown. This distribution also decreases towards larger radii, but not until ring #8. This can be explained with the scatter-plot of number of secondaries per spike as a function of its ring radius (right). At large radii it shows a large number of spikes but with low multiplicities. The smaller the radius, the more spikes with high multiplicities occur, which explains the difference in distributions of the radial spike rate and the radial background rate. Compare figure 4.8.
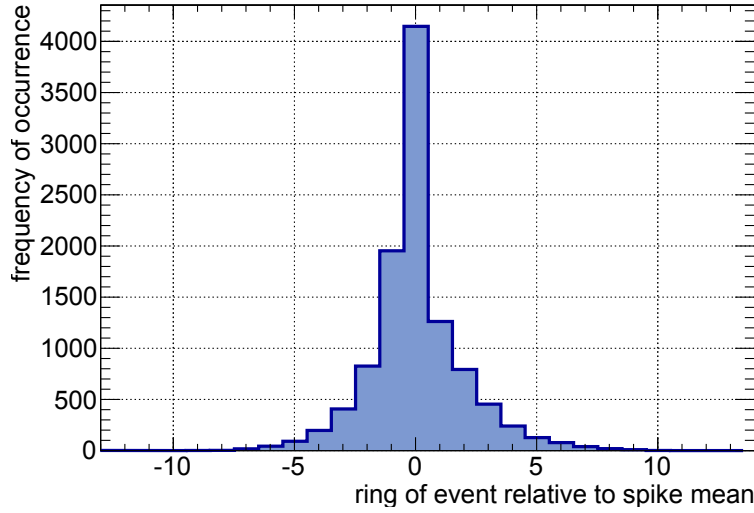
Figure A.7.: Fuzziness of spike-rings at 5 G-setting during high pressure measurements. The relative distance to the mean radius of the spike is calculated and inserted into the histogram. About 70 % of the events are distributed around the mean radius and in the neighboring rings. Only a fraction of 3 % extend over more than 4 rings. Compare figure 4.9.
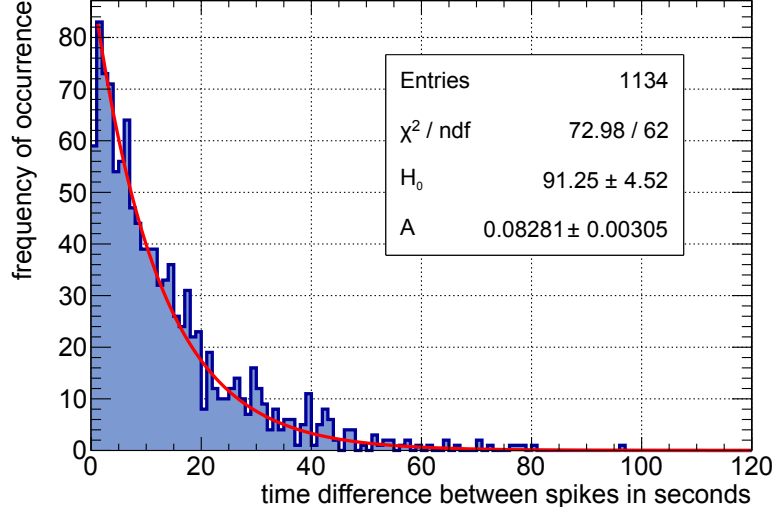
Figure A.8.: Observed activity for 5 G-setting. The drop at the first bin is due to the interarrival-time cut as introduced in section 4.1, where detector hits time differences lower than 0.2 s are assigned to one spike. Compare figure 4.10.

$A_{MS}^{5G} = (180.2 \pm 22.7)$ mBq. The activity determined by 9 G-measurements is $A_{MS}^{9G} = (189.8 \pm 12.8)$ mBq. Thus, both activities agree very well within the errors. Note, that at this time no corrections to the activity are applied. These are required, as the way of the selection of radon-spikes cannot detect all decays.

A.4.5. Multiplicity of Radon-Spikes and Correction Factors

The multiplicity distribution at 5 G-setting looks very similar to the distribution during 9 G-setting. The distribution is shown in figure A.10. At this setting, the χ^2/NDF value is better than at the 9 G-setting. The slope is different to the slope during the 9 G-setting, but this may due to the low statistics.

The χ^2/NDF value gives a hint, that the multiplicity is not power-law distributed. In addition, the power-law is fitted to different regions of this distribution. The lower bound is varied between $N_{min} = 2$ and $N_{min} = 50$. The upper bound is fix at $N = 100$. The yielded slope is plotted over the lower bound and shown in figure A.11. In contrast to the same analysis for the 9 G-setting, this distribution is not that obvious. Up to $N_{min} \approx 20$, the slope significantly varies. For higher N_{min}, the error bars are very large. Probably there also the slope significantly change. Consequently, the distribution follows in none region a power-law. However, more statistic is required to answer this question finally for the 5 G-setting.

A first-bin estimation cannot be performed, as no cold baffle measurements for the 5 G-setting during the SDS-1 phase are executed. Consequently, just the upper
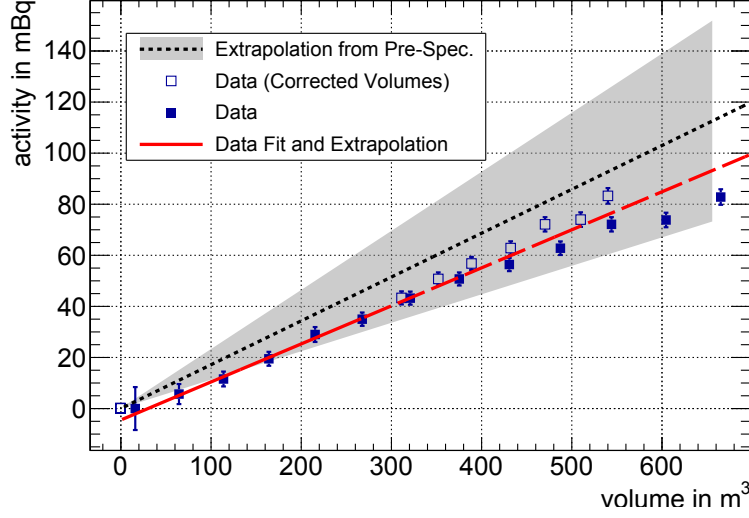
Figure A.9.: Activity extrapolated to the entire main spectrometer volume. Every point is obtained by successively considering more pixel-rings of the FPD starting at the inner four pixels. The fit is applied only to the first six data points (solid line) and extrapolated (dashed line). The kink occurs due to unused pixels, which are corrected at the empty squares. An extrapolation from the pre-spectrometer [MDF$^+$13] is drawn as dotted lines with its error-band. Compare figure 4.11.

bound correction factor can be calculated. This factor is obtained by extrapolation the power-law to bin one. Using equation (4.7), the correction factor is determined to

$$\kappa_{N_{\min}}^{\text{upper}} = 3.03 \pm 0.13, \tag{A.22}$$

while the slope is measured to $\gamma = 2.01 \pm 0.04$. This correction factor is greater than the factor, obtained by data during the 9 G-setting (compare table 4.1). This may due to the low statistics, as mentioned above. Consequently, the upper bound estimation for the activity inside the flux-tube volume is determined to (251.1 ± 14.5) mBq. The activity inside the entire main spectrometer volume is (546.6 ± 72.9) mBq

A.4.6. Storage Time and Background Estimation at 10^{-10} mbar and 10^{-11} mbar

The storage time is measured for the 5 G-setting as well. The obtained distribution is shown in figure A.12. The mean storage time is measured to (184.5 ± 5.2) ms. The most probably value (MPV) is obtained by the fit: (62.77 ± 36.96) ms. The errors are very large. That is caused by the low statistics. These values are similar to the values resulted by the 9 G-analysis: The mean value is determined to (212.5 ± 3.5) ms, the MPV to (63.05 ± 1.40) ms.
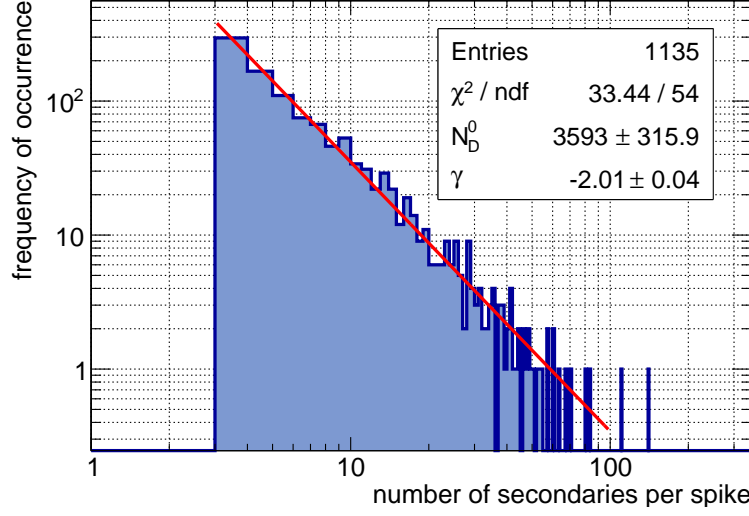
Figure A.10.: Applying power-law fits to the multiplicity by increasing successively N_{min} at 5 G-setting. As the slope γ is changing in particular for low N_{min}, it is reasonable that the multiplicity is not power-law distributed. For higher $N_{min} \gtrsim 25$, the multiplicity may follow a power-law. Compare figure 4.12.
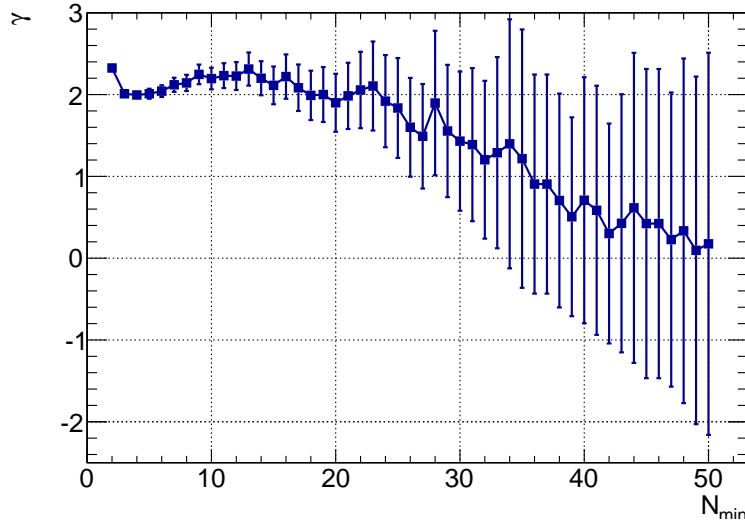
Figure A.11.: Applying power-law fits to the multiplicity by increasing successively N_{min} for data at 5 G-setting. As the slope γ is changing in particular for low N_{min} up to 20, it is reasonable that the multiplicity is not power-law distributed. For higher N_{min}, the error bars are to large to make a definitive statement. Probably the slope also changes in this region. Compare figure 4.13.
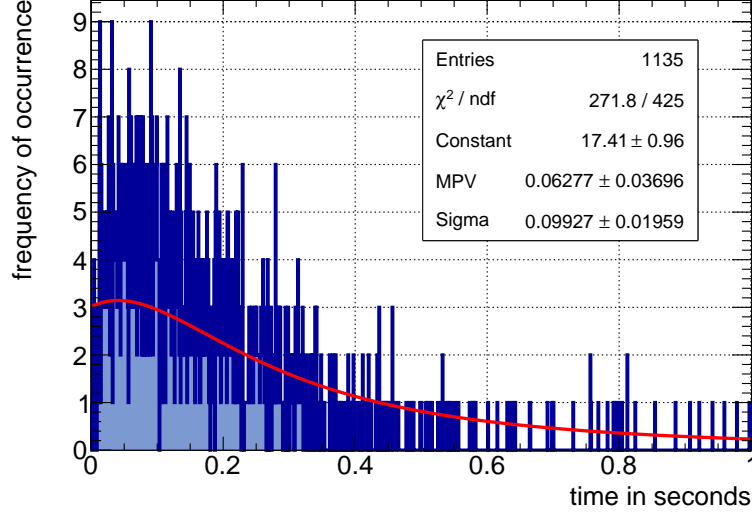
Figure A.12.: Storage time of trapped electrons at the 9 G-setting. The measured distribution follows in good agreement a Landau-distribution. The most probable value for the storage time is determined to (62.77 ± 36.96) ms. Compare figure 4.16.
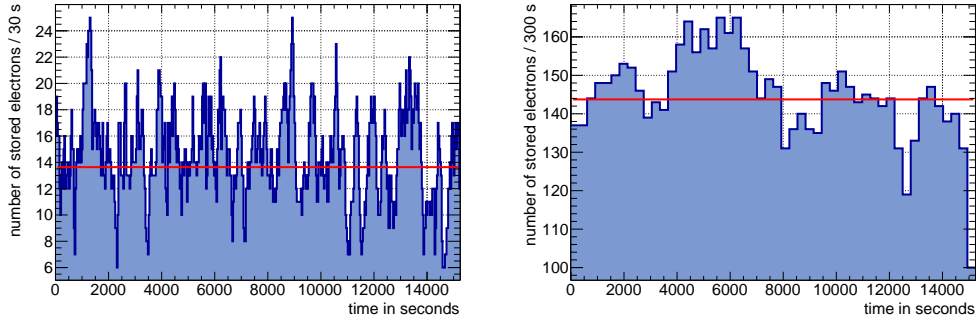
Figure A.13.: Number of simultaneously stored electrons at the 5 G-setting. (left) Extrapolation to 10^{-10} mbar (SDS-1) implies 13.6 ± 3.5 simultaneously stored electrons within 30 s. (right) Extrapolation to 10^{-11} mbar (normal pressure) with 143.7 ± 11.6 simultaneously stored electrons within 300 s. Compare figure 4.17.

Table A.4.: Radon-induced background extrapolations from high-pressure 10^{-8} mbar to 10^{-10} mbar (SDS-1) and 10^{-11} mbar (normal-pressure) for 5 G-setting. The table lists the results by stretching all radon-spikes by the factor ζ. Different methods yields different ζ for 10^{-11} mbar.

Pressure in mbar	ζ	Bin-Width in s	Mean De-tector Rate in mcps	Simultaneous Stored Electrons within Bin-Width	Simultaneous Stored Electrons (bin-width independent)
10^{-10}	900	30	332.6 ± 3.2	13.6 ± 3.5	12.3 ± 3.5
10^{-11}	3916	100	329.2 ± 3.2	60.1 ± 6.7	53.4 ± 7.3
10^{-11}	9000	300	329.2 ± 3.2	143.7 ± 11.6	121.2 ± 11.0

The radon-induced background for the 5 G-setting is extrapolated to 10^{-10} mbar (SDS-1) and 10^{-11} mbar (normal-pressure). The same stretching factors ζ are used as in section 4.6.2: For 10^{-10} mbar is $\zeta = 900$ used. For 10^{-11} mbar is $\zeta = 3916$ and $\zeta = 9000$ used. The results are listed in table A.4 and shown in figure A.13. The obtained numbers of simultaneous stored particles are agree with the rough estimation, explained in section 4.6.2. The following values are expected:

- $\zeta = 900$ and 10^{-10} mbar: 13 within 30 s.

- $\zeta = 3916$ and 10^{-11} mbar: 59 within 100 s.

- $\zeta = 9000$ and 10^{-11} mbar: 137 within 300 s.

The values, listed in table A.4, agree very well with these expectations.

The expected detector rate for 10^{-10} mbar is determined to (332.6 ± 3.2) mcps. For 10^{-11} mbar, the expected rate is (329.2 ± 3.2) mcps.

A. Appendix

List of Figures

List of Tables

List of Tables

Bibliography

[AAA+01] Q. AHMAD, R. ALLEN, T. ANDERSEN, J. ANGLIN ET AL. Measurement of the rate of $\nu_e + d \to p + p + e^-$ interactions produced by 8b solar neutrinos at the sudbury neutrino observatory. *Physical Review Letters*, 87(7):071301/1–071301/6, 2001.

[AAPA+11] H. AIHARA, C. ALLENDE PRIETO, D. AN, S. ANDERSON ET AL. The eighth data release of the sloan digital sky survey: First data from sdss-iii. *Astrophysical Journal, Supplement Series*, 193(2), 2011.

[AE14] ADE, P. and EFSTATHIOU, G. Planck 2013 results. xvi. cosmological parameters. *A&A*, 2014. doi:10.1051/0004-6361/201321591.

[AF11] S. AGARWAL and H. FELDMAN. The effect of massive neutrinos on the matter power spectrum. *Monthly Notices of the Royal Astronomical Society*, 410(3):1647–1654, 2011.

[Bac12] F. BACHMANN. *Aufbau und Inbetriebnahme des CPS-Testaufbaus*. Bachelor thesis, Karlsruhe Institute of Technology, 2012.

[BBB+12] M. BABUTZKA, M. BAHR, J. BONN, B. BORNSCHEIN ET AL. Monitoring of the operating parameters of the katrin windowless gaseous tritium source. *New Journal of Physics*, 14, 2012.

[BBB+14] J. BARRETT, A. BEGLARIAN, J. BEHRENS, T. CORONA ET AL. Results of the first katrin sds measurement phase, 2014. Internal report.

[BH59] J. BANG and J. M. HANSTEEN. *Coulomb deflection effects on ionization and pair-production phenomena*. Number 31,13 in Matematisk-fysiske meddelelser. Munksgaard, København, 1959.

[BP04] J. BAHCALL and C. PEÑA-GARAY. Solar models and solar neutrino oscillations. *New Journal of Physics*, 6:1–19, 2004.

[DTN+81] M. DOI, T. TOTANI, H. NISHIURA, K. OKUDA ET AL. Neutrino masses and the double β decay. *Physics Letters B*, 103(3):219–224, 1981.

[EHM87] S. ELLIOTT, A. HAHN and M. MOE. Direct evidence for two-neutrino double-beta decay in se82. *Physical Review Letters*, 59(18):2020–2023, 1987.

[EHO⁺04] S. EIDELMAN, K. HAYES, K. OLIVE, M. AGUILAR-BENITEZ ET AL. Review of Particle Physics. *Physics Letters B*, 592:1+, 2004. URL `http://pdg.lbl.gov`.

[Eic08] F. EICHELHARDT. *Measurement of the Tritium Pumping Properties of a 4.2 K Argon Condensate for the Cryogenic Pumping Section of KATRIN*. Phd thesis, Karlsruhe Institute of Technology, 2008.

[Erh12] M. ERHARD. *Untersuchung der Langzeitstabilität des nuklearen Standards für die Energieskala des KATRIN-Experiments*. Diploma thesis, Karlsruhe Institute of Technology, 2012.

[FBD⁺11] F. FRÄNKLE, L. BORNSCHEIN, G. DREXLIN, F. GLÜCK ET AL. Radon induced background processes in the katrin pre-spectrometer. *Astroparticle Physics*, 35(3):128–134, 2011.

[Fer34] E. FERMI. Versuch einer theorie der betastrahlen. *Zeitschrift für Physik*, 88:161–177, 1934.

[Frä10] F. FRÄNKLE. *Background Investigations of the KATRIN Pre-Spectrometer*. Phd thesis, Karlsruhe Institute of Technology, 2010.

[Fre74] M. S. FREEDMAN. Atomic structure effects in nuclear events. *Annual Review of Nuclear Science*, 24(1):209–248, 1974. doi:10.1146/annurev. ns.24.120174.001233.

[Fri22] A. FRIEDMAN. Über die krümmung des raumes. *Zeitschrift für Physik*, 10(1):377–386, 1922. doi:10.1007/BF01332580.

[FSS⁺11] S. FISCHER, M. STURM, M. SCHLÖSSER, B. BORNSCHEIN ET AL. Monitoring of tritium purity during long-term circulation in the katrin test experiment loopino using laser raman spectroscopy. *Fusion Science and Technology*, 60(3):925–930, 2011.

[Fur39] W. FURRY. On transition probabilities in double beta-disintegration. *Physical Review*, 56(12):1184–1193, 1939.

[GBB⁺10] W. GIL, J. BONN, B. BORNSCHEIN, R. GEHRING ET AL. The cryogenic pumping section of the katrin experiment. *IEEE Transactions on Applied Superconductivity*, 20(3):316–319, 2010.

[GGS58] M. GOLDHABER, L. GRODZINS and A. W. SUNYAR. Helicity of neutrinos. *Phys. Rev.*, 109:1015–1017, 1958. doi:10.1103/PhysRev. 109.1015.

[Goe35] M. GOEPPERT-MAYER. Double beta-disintegration. *Physical Review*, 48(6):512–516, 1935.

[Gör14] S. GÖRHARDT. *Background Reduction Methods and Vacuum Technology at the KATRIN Spectrometers*. Phd thesis, Karlsruhe Institute of Technology, 2014.

[Han10] S. HANNESTAD. Neutrino physics from precision cosmology. *Progress in Particle and Nuclear Physics*, 65(2):185–208, 2010.

[Har12] F. HARMS. *Assembly and First Results of the KATRIN Focal-Plane Detector System at KIT*. Diploma thesis, Karlsruhe Institute of Technology, 2012.

[HIKO08] H. HIGAKI, K. ITO, K. KIRA and H. OKAMOTO. Electrons confined with an axially symmetric magnetic mirror field. volume 1037, pages 106–114. 2008.

[KAT04] KATRIN COLLABORATION. Katrin design report 2004. *Wissenschaftliche Berichte FZKA 7090*, 2004.

[LBB$^+$12] S. LUKIČ, B. BORNSCHEIN, L. BORNSCHEIN, G. DREXLIN ET AL. Measurement of the gas-flow reduction factor of the katrin dps2-f differential pumping section. *Vacuum*, 86(8):1126–1133, 2012.

[LCM$^+$71] C. LU, T. CARLSON, F. MALIK, T. TUCKER ET AL. Relativistic hartree-fock-slater eigenvalues, radial expectation values, and potentials for atoms, $2 \leq z \leq 126$. *Atomic Data and Nuclear Data Tables*, 3(C):1–31, 1971.

[LP12] J. LESGOURGUES and S. PASTOR. Neutrino mass from cosmology. *Advances in High Energy Physics*, 2012, 2012.

[Mac14] C. MACOLINO. Results on neutrinoless double-beta decay from gerda phase i. *Modern Physics Letters A*, 29(1), 2014.

[MDF$^+$13] S. MERTENS, G. DREXLIN, F. FRÄNKLE, D. FURSE ET AL. Background due to stored electrons following nuclear decays in the katrin spectrometers and its impact on the neutrino mass sensitivity. *Astroparticle Physics*, 41:52–62, 2013.

[Mer12] S. MERTENS. *Study of Background Processes in the Electrostatic Spectrometers of the KATRIN Experiment*. Phd thesis, Karlsruhe Institute of Technology, 2012.

[Mis06] MISSMJ, 2006. URL http://commons.wikimedia.org/wiki/File:Standard_Model_of_Elementary_Particles.svg, found 08/31/2014.

[MS86] S. MIKHEYEV and A. SMIRNOV. Resonant amplification of ν oscillations in matter and solar-neutrino spectroscopy. *Il Nuovo Cimento C*, 9(1):17–26, 1986. doi:10.1007/BF02508049.

[Pra11] M. PRALL. *Transmission properties of the pre-spectrometer at high surplus energies*. Phd thsis, University of Münster, 2011.

Bibliography

[Rac37]   G. RACAH. Sulla simmetria tra particelle e antiparticelle. *Il Nuovo Cimento*, 14(7):322–328, 1937.

[RAP75a]   M. RAPAPORT, F. ASARO and I. PERLMAN. K-shell electron shake-off accompanying alpha decay. *Physical Review C*, 11(5):1740–1745, 1975.

[RAP75b]   M. RAPAPORT, F. ASARO and I. PERLMAN. L- and m-shell electron shake-off accompanying alpha decay. *Physical Review C*, 11(5):1746–1754, 1975.

[RC59]   F. REINES and C. L. COWAN. Free antineutrino absorption cross section. i. measurement of the free antineutrino absorption cross section by protons. *Phys. Rev.*, 113:273–279, 1959. doi:10.1103/PhysRev.113.273.

[Rei13]   J. C. REICH. *Magnetic Field Inhomogeneities and Their Influence on Transmission and Background at the KATRIN Main Spectrometer.* Phd thesis, Karlsruhe Institute of Technology, 2013.

[Sch10]   J. SCHWARZ. *Design zur Messung der elektro-optischen Eigenschaften der differentiellen Pumpstrecke DPS2-F des KATRIN-Experiments.* Diploma thesis, Karlsruhe Institute of Technology, 2010.

[Sch14]   J. SCHWARZ. *The Detector System or the KATRIN Experiment - Implementation and First Measurement with the Spectrometer.* Phd thesis, Karlsruhe Institute of Technology, 2014.

[Sie68]   K. SIEGBAHN. *Alpha-, Beta- and Gamma-Ray Spectroscopy*, volume 2. North-Holland Publishing Company, 1968.

[SM13]   J. E. SANSONETTI and W. C. MARTIN. National Institute of Standards and Technology Gaithersburg, MD 20899, 2013. URL http://physics.nist.gov/PhysRefData/Handbook/.

[SNE14]   SNEWS, 2014. URL http://snews.bnl.gov/news.html, found 09/01/2014.

[Son]   A. SONZOGNI. Chart of nuclides. National Nuclear Data Center: Brookhaven National Laboratory. URL http://www.nndc.bnl.gov/chart/.

[TLMB08]   C. THEISEN, A. LOPEZ-MARTENS and C. BONNELLE. Internal conversion and summing effects in heavy-nuclei spectroscopy. *Nuclear Instruments and Methods in Physics Research, Section A: Accelerators, Spectrometers, Detectors and Associated Equipment*, 589(2):230–242, 2008.

[WA03]   K. WINTER and G. ALTARELLI. *Neutrino Mass.* Springer, 2003.

[Wan13] N. WANDKOWSKY. *Study of background and transmission properties of the KATRIN spectrometers.* Phd thesis, Karlsruhe Institute of Technlogy, 2013.

[WDF⁺13] N. WANDKOWSKY, G. DREXLIN, F. FRÄNKLE, F. GLÜCK ET AL. Modeling of electron emission processes accompanying radon-α-decays within electrostatic spectrometers. *New Journal of Physics*, 15, 2013.

[Wol78] L. WOLFENSTEIN. Neutrino oscillations in matter. *Phys. Rev. D*, 17:2369–2374, 1978. doi:10.1103/PhysRevD.17.2369.

[Wol09] J. WOLF. Size matters: The vacuum system of the katrin neutrino experiment. *Journal of the Vacuum Society of Japan*, 52(5):278–284, 2009.

[YAA⁺06] W.-M. YAO, C. AMSLER, D. ASNER, R. BARNETT ET AL. Review of particle physics. *Journal of Physics G: Nuclear and Particle Physics*, 33(1):1, 2006.

Bibliography

Danksagung

Zum Schluss möchte ich mich noch bei all denjenigen herzlich bedanken, die mich während diesem Jahr und bei der Masterarbeit bei KATRIN unterstützt und zum Gelingen dieser Arbeit beigetragen haben. Besonderer Dank geht an

- PROF. DR. G. DREXLIN, für die Möglichkeit bei KATRIN diese Arbeit zu schreiben. Vielen Dank für das spannende und erfahrungsreiche Jahr und die Vorlesungen ATP I und II.

- PROF. DR. G. QUAST für die Übernahme des Korreferats und die Vorlesung DETEKTOREN IN DER TEILCHEN- UND ASTROTEILCHENPHYSIK.

- PROF. DR. G. DREXLIN and PROF. DR. J. A. FORMAGGIO for giving me the opportunitiy to stay abroad at MIT and Boston and participate in the NEUTRINO2014 conference.

- DR. MARCO KLEESIEK für die Betreuung und das "sich immer für Jan Zeit nehmen", das Helfen bei Statistik- und Compilerproblemen. Danke!

- DR. N. WANDKOWSKY und ihre Doktorarbeit für die so vielen Hilfen bei Radon und KASSIOPEIA und für die Simulationen.

- DR. F. GLÜCK für die großartige Hilfe bei den Wirkungsquerschnitten.

- DIPL.-PHYS. S. GROH und DIPL.-PHYS. N. TROST für die unzähligen Hilfen bei KASSIOPEIA.

- DIPL.-PHYS. F. HARMS und DR. J. SCHWARZ für die vielen Hilfen bei BEANS.

- DR. N. WANDKOWSKY, DR. M. KLEESIEK, DR. M. LUDWIG, DR. D. HUBER, DR. B. FUCHS und M. OERTLIN für das Korrekturlesen.

- meinen Bürokollegen NANCY und NIKOLAUS für die tolle Arbeitsatmosphäre und die schöne Zeit.

- TONI für die tollen Kaffeepausen, vielen lustigen Abende und für die Freundschaft!

- FRANK THE TANK für das Aufmuntern, die Kaffeepausen (mit den witzigen Gesprächen und Geschichten), die Abende und für die Freundschaft! Und natürlich für das Einspringen beim Organisieren des STAMMTISCHES®.

- ROWNTREE'S für das Erfinden von KITKAT®.

Danksagung

- BBA[3] für die Übernahme des KIOSKS®.

- RODOLPHE für die Übernahme des WABs[4].

- NANCY, TONI, FRANK THE TANK, MARCO, GROHMEISSTER, MARCELLO, MO, BBA, HEIZI, den DING und den ANDEREN, MAGNUS, SEBASTIAN, CHUCK NORRIS, AXEL und alle anderen von KATRIN, TLK und EDELWEISS für die tolle und lustige Zeit bei KATRIN, die tollen STAMMTISCHE, den WABs, Fußballspielen, Lasertag-Spielen, für das Grillen, Go-Kart-fahren und die lustige Zeit bei der DPG und in Boston

An diesem Punkt möchte ich auch noch die Gelegenheit ergreifen, mich bei all denjenigen zu bedanken, die mich während des gesamten Studiums unterstützt haben. Dazu zählen in erster Linie meine Eltern und meine beiden Geschwister, die mich durch alle Höhen und Tiefen begleitet haben. Ebenfalls wäre ein Studium nichts ohne gute Freunde und Kommilitonen, die u. a. auch die Lernzeit zu einer tollen Zeit gemacht haben! Nicht zu vergessen sind die tolle Arbeitsgruppe, in der ich meine Bachelorarbeit schreiben durfte, und alle anderen für mich wichtigen Menschen, die ich während des Studiums kennenlernen durfte.

Es war eine tolle Zeit, vielen Dank Euch allen!

---

[3]Birgit

[4]© by DANIEL HUBER.

Erklärung

Hiermit versichere ich, dass ich die vorliegende Masterarbeit selbstständig und nur unter Verwendung der angegebenen Quellen und Hilfsmittel verfasst habe.

Karlsruhe, September 2014

....
(Jan Oertlin)

Mhhhhh... Spareribs...